

DYNAMICS OF DIBLOCK COPOLYMERS

NONEQUILIBRIUM DYNAMICS IN SYMMETRIC DIBLOCK COPOLYMER SYSTEMS

By

ROBERT DAVIDSON PETERS, B.Sc., M.Sc.

A Thesis

Submitted to the School of Graduate Studies
in Partial Fulfillment of the Requirements
for the Degree

Doctor of Philosophy

McMaster University

©Copyright by Robert Davidson Peters, 2014.

DOCTOR OF PHILOSOPHY (2014)
(Physics)

McMaster University
Hamilton, Ontario

TITLE: Nonequilibrium dynamics in symmetric diblock copolymer systems

AUTHOR: Robert Davidson Peters, B.Sc., M.Sc.(McMaster University)

SUPERVISOR: Dr. Kari Dalnoki-Veress

NUMBER OF PAGES: vii, 101

Abstract

In this dissertation, experiments are described which elucidate how the ordering of symmetric diblock copolymers affects the dynamics within various geometries. In all studies presented herein, experimental techniques are used to probe the dynamics of symmetric diblock copolymer systems as they progress toward equilibrium and to study the role that nanoscale ordering plays in these processes.

In the majority of work presented herein, experiments were performed on symmetric diblock copolymer thin films. This work focuses on the effect of various sample preparation techniques on the equilibration kinetics of lamellar forming films. Films are prepared with varying thicknesses in the homogeneous, disordered state and annealed to form islands and holes as the surface decomposes to form commensurate thicknesses. Both nucleated and spinodal growth patterns were observed for this surface decomposition dependent on the initial thickness and intermediate morphologies formed upon ordering. We also prepare equilibrium commensurate films and induce a step change in surface interactions, switching from asymmetric to symmetric wetting boundaries. Upon equilibration, a perforated lamella forms at the free surface to mediate the order-order transition, inducing hole growth with a ramified shape.

In the final project, the effect that lamellar order has on dynamics is studied within unstable polymer melt bridges. Liquid bridges are what is formed when a droplet is stretched between two surfaces, like spit between two fingers. Disordered diblock bridges are shown to evolve similar to their homopolymer counterparts. However, ordered diblock copolymer exhibits an enhanced stability with an inhibition of flow proposed to be induced by the isotropic orientational order within the bridge. As well, shear thinning is observed that is believed to be caused by an alignment of ordered domains along the bridge axis due to shear strain rates, providing pathways for flow of diblock copolymer out of the unstable bridge.

Acknowledgements

When you spend 6 years endeavouring to complete a PhD, there are many people without whom its completion would have been impossible or unbearable or possibly both. A humongous thanks must be given to all the great people of the McMaster Physics department. I know that wherever I go next, it will be hard to top the people I've had the pleasure of working with these last few years.

To all those with whom I got to enjoy the KDV experience, I count myself lucky to have had the chance to work with each and every one of you. In backwards chronological order there's Solomon, Raffi, Paul, Marl, Matilda, Josh, Jess, Olli, MJ, Mark H., Adam, and Andrew. You guys made the grind that is grad school an absolute joy every single day. I truly enjoyed getting to know all of you individually and hope we get to hang out often in my post KDV life.

To my two older brothers, Bryan and Craig. Thanks for being the people I could always look up to and count on when I really needed you. Though all three of us are so incredibly different, that's what makes it so fun to hang out with both of you. Let's never stop doing that.

To Mom and Dad, thank you for always knowing that I could do this even when I didn't believe you. Your constant support and encouragement throughout my entire life is irrefutable, and I can't express in words how much you have done for me. Thank you for teaching me what hard work can achieve while still raising me to know what is important in life.

Kari. The supervisor that can not be beat. Over the last 6 (and more) years you have inspired and motivated me to become not only a better researcher, but a better human being. Your passion for science is contagious, and without your support and advice, I have no doubt that these last few years would have been miserable, or very likely not even possible. I can't imagine not being able to work with you anymore, possibly because it hardly feels like work at all. No boss or supervisor will ever be able to top what you have done for me, and for that I will always be thankful.

And finally to my wife, Jenn. You make me a better person, each and every day we are together. Your constant support, patience, motivation, love and encouragement is what has kept me going these last 4 years. Through it all, I knew that I could always count on you no matter what. Thank you for being amazing in every way.

Contents

1	Introduction	1
1.1	Polymers	2
1.1.1	Phase separation: equilibrium and kinetics	6
1.1.2	Time-temperature superposition	16
1.2	Diblock copolymers	17
1.2.1	Equilibrium	17
1.2.2	Interfacial effects	23
1.2.3	Order-order transitions	26
1.2.4	Shear effects	28
1.3	Liquid Jets and Bridges	29
1.3.1	Newtonian liquids	30
1.3.2	Polymer solutions and melts	37
2	Experimental Details	41
2.1	Sample Preparation	41
2.1.1	Materials	41
2.1.2	Film Preparation	43
2.1.3	Polymer Melt Bridge Preparation	44
2.2	Sample Characterization	45
2.2.1	Optical Microscopy	45
2.2.2	Ellipsometry	45
2.2.3	Atomic Force Microscopy	48

CONTENTS

3	Summary of Papers	51
3.1	Manuscript I	52
3.2	Manuscript II	60
3.3	Manuscript III	66
3.4	Manuscript IV	73
4	Conclusions	83
A	Works not included in thesis	87
A.1	Paper I	87
A.2	Paper II	87

List of Figures

1.1	Variety of polymer architectures	3
1.2	Energy of mixing vs. weight fraction of polymer	9
1.3	Phase diagram of polymer mixture stability	11
1.4	Classical nucleation theory	13
1.5	Diblock copolymer schematic	18
1.6	Diblock copolymer architectures	19
1.7	Morphologies of capped thin films	25
1.8	Schematic of equilibration of incommensurate supported films	26
1.9	Schematic of surface tension acting as a force	31
1.10	Schematic of determining curvature for complex shapes	32
1.11	Schematic of Plateau-Rayleigh instability	34
1.12	Schematic of liquid bridges	36
1.13	Schematic of shear strain in liquid bridge	37
2.1	Molecular structure of polymers	42
2.2	Polymer bridge experimental schematic	44
2.3	Schematic for ellipsometry setup	46

LIST OF FIGURES

Chapter 1

Introduction

Many naturally occurring systems over a wide range of length scales undergo self-assembly including molecular crystals, cellular membranes, colloidal crystals, bacterial colonies, and schools of fish [1]. The one thing all of these systems have in common is their ability to organize into structures and patterns composed of many different components without any active human intervention. One model system which has provided a great deal of information on general self-assembly processes is the block copolymer. Block copolymers are used in a number of common materials, including ABS thermoplastic, a high strength plastic used in the production of protective headgear, medical devices, and toys such as Lego. Symmetric diblock copolymers, the focus of this thesis, are a simple type of copolymer which consists of two equal length homopolymer blocks that are covalently bonded together. The self-assembled nanostructures formed by these molecules are well reviewed [2], however there are many aspects of ordering dynamics in diblock copolymer systems that are yet to be studied. Thus, the goal throughout my PhD has been to understand the ordering dynamics of various symmetric diblock copolymer systems. By studying these assembly dynamics, a better understanding of how to control the final morphologies of block copolymer systems can be developed.

In order to understand the physical properties and dynamics of diblock copolymers studied within this thesis, one must start from the basic building blocks upon which these molecules are built, simple homopolymer chains. In section 1.1 I will provide the background necessary for understanding statics and dynamics of self assembly in

diblock copolymer melts by providing a description of polymer chains, phase separation of polymer blends, the dynamics of phase separation, and the time-temperature properties of polymers. In section 1.2 I will discuss the various properties of diblock copolymers which are pertinent to this thesis work, including the equilibrium self-assembly of bulk diblock copolymers, confinement effects on equilibrium structure, the rich history of order-order phase transitions and the effect of shear strain rates on the orientation of self-assembled domains. In section 1.3 I will switch focus to the dynamics of break-up within the geometry used for my final project, liquid bridges. I will provide an overview of the instabilities and dynamics for both Newtonian and polymeric liquids in axi-symmetric jets and bridges, with the eventual goal of understanding the role that diblock copolymer order plays in changing these dynamics.

1.1 Polymers

Polymers are molecules that are composed of many repeating units called monomers. Though polymers come in many different configurations (see Figure 1.1), in this work I consider only linear polymer molecules (Figure 1.1a). In linear polymers, monomers are connected in a single long chain. Long polymer chains tend to be highly flexible molecules, giving rise to a variety of interesting properties in polymeric melts including exhibiting both elastic and viscous responses. Though this flexibility may arise due to a variety of different mechanisms dependent on the molecular composition of the monomers [3], the effects are often similar independent of monomeric composition. In order to elucidate the physical source of some of these global polymer melt properties, a study of the statistical mechanics of individual polymer chains is necessary.

In the spirit of generalization, I will discuss a common representation of the polymer chain utilized by many authors to successfully describe chains in the melt state, the gaussian or ‘ideal’ polymer chain [3–5]. To understand this depiction, consider that the polymer chain is composed of N_m monomers, each of length $|\vec{r}|$, where \vec{r} are the bond vectors for the monomers. Consider adjacent monomers, \vec{r}_i and \vec{r}_{i+1} , that are correlated by some bond angle, θ , such that $\vec{r}_i \cdot \vec{r}_{i+1} = |\vec{r}|^2 \cos \theta$. In order to develop a generalized model of polymer molecules, we wish to remove this level of detail where bond angles are affected by the particular monomer that makes up the

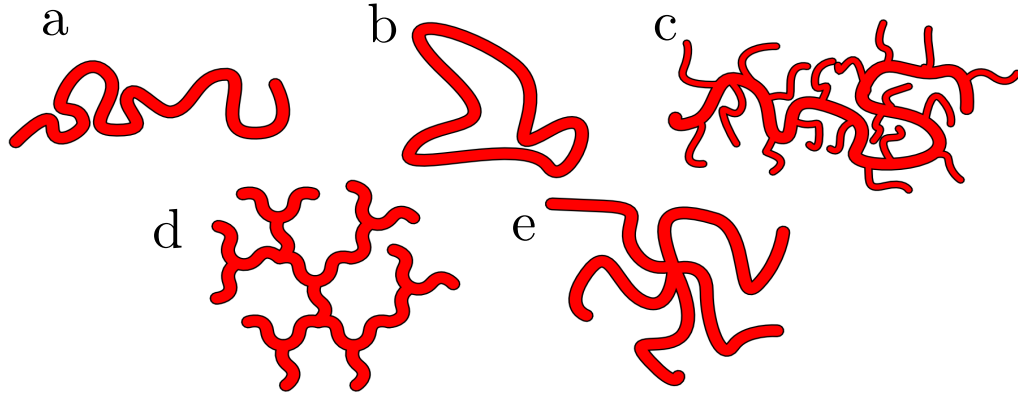


Figure 1.1: Various polymer architectures which may be fabricated in polymerization process. a) linear polymer, b) ring polymer, c) brush polymer, d) dendrimer, and e) star polymer

polymer chain. Therefore, in the ideal chain model, we consider a segment length,

$$\vec{a}_i = \sum_{k=i}^{i+n} \vec{r}_k, \quad (1.1)$$

which is the sum of several bond vectors. The key is that n is chosen sufficiently large so that each segment is uncorrelated, removing molecular details to describe chains equivalently. Represented mathematically, $\langle \vec{a}_i \cdot \vec{a}_{i+1} \rangle \approx 0$. Werner Kuhn proposed that the contour lengths of the real and ideal polymer chains be equal, i.e. $N_m |\vec{r}| = N |\vec{a}|$ [3, 5]. In other words, there are N Kuhn segments, $|\vec{a}|$, in an ideal chain, each completely uncorrelated from its neighbouring segments [3, 5].

This generalization of the polymer molecule as a chain of uncorrelated segments is useful as it provides a direct equivalency to a random gaussian walk of N uncorrelated steps of length $a = |\vec{a}|$. In the following I will highlight some of the interesting features of the gaussian chain result, starting with a calculation of a measure of polymer size, the average end-to-end distance of a polymer chain, \bar{R}_{ee} [3]. The end-to-end distance, \vec{R}_{ee} , of a gaussian chain is simply

$$\vec{R}_{ee} = \sum_{i=1}^N \vec{a}_i. \quad (1.2)$$

Just like a random walk, the ensemble average end-to-end distance for a polymer molecule is zero. However, in analogy to the measure of the average extent of a random walk, the average mean squared end-to-end distance can be calculated to obtain a measure for the average size of a polymer molecule as

$$\bar{R}_{ee} = \sqrt{\langle \vec{R}_{ee}^2 \rangle} = \sqrt{\sum_{i=0}^N \sum_{j=0}^N \langle \vec{a}_i \cdot \vec{a}_j \rangle} = \sqrt{N}a. \quad (1.3)$$

One interesting results from this calculation for the ‘size’ of the polymer molecule is that it does not depend linearly on the length of the chain as you might expect, but varies with \sqrt{N} , just like a random walk. This end-to-end distance not only sets the length scale for our polymer chains but, as I will discuss in the following paragraphs, plays a fundamental role in determining the entropy of polymer chains. Polymer chain entropy is an intrinsic property which gives rise to a number of the interesting effects observed in bulk polymer melts.

In discussing the entropy of polymer chains, I will first consider the free energy of a single polymer chain in a melt with a particular end-to-end distance, R . The Helmholtz free energy is defined as

$$F = U - TS, \quad (1.4)$$

where U is the internal energy, T is temperature, and S is the entropy of the polymer molecule. Since throughout our experiments, polymer molecules in the melt do not break apart or bond together, the internal energy within the melt is constant. Therefore, the only variable contribution to the free energy is the entropy of the polymer chains which can be calculated as

$$S \sim \ln [p(R)], \quad (1.5)$$

where $p(R)$ is the probability that a polymer has a size R in the melt. Utilizing the ideal chain model, the statistics of random walks can be used to calculate the

probability of a three dimensional random walk to be [3, 4]

$$p(R) = \left(\frac{3}{2\pi\bar{R}_{ee}^2} \right)^{3/2} \exp \left(-\frac{3R^2}{2\bar{R}_{ee}^2} \right). \quad (1.6)$$

Substituting Equation 1.6 into Equation 1.5, a description for the entropy of a single polymer molecule in a melt is seen to be

$$S \sim S_0 - \frac{3R^2}{2\bar{R}_{ee}^2}, \quad (1.7)$$

where S_0 is a constant. In reference to Equation 1.4 it is clear that since U is constant, the conformation of polymer molecules has a great effect on the free energy of a polymer melt. From Equation 1.7, if a chain is stretched (R increases), there is an energy cost that is quadratically dependent on the new end-to-end distance. This energy cost is inversely dependent on the square of average end-to-end distance, \bar{R}_{ee}^2 , illustrating its importance as a length scale in polymeric systems.

An analogy for the free energy of a polymer chain may be made to a simple Hookean spring, where the energy of the system varies with extension or compression squared ($F \sim kx^2$) where k represents the spring constant. Therefore, it is clear that the polymers high elasticity is due to this entropic stretching cost in the free energy. It is also interesting to consider that since the product of entropy and temperature gives us the free energy contribution, the spring constant k , contains the temperature term, giving rise to a spring constant that is temperature dependent. It is worth noting that this Hookean response is for individual chains and does not describe entangled or cross linked (rubberized) networks of polymers, which exhibit non-linear elasticity.

In summary, linear polymers are well described by a simple random walk of uncorrelated chain segments in the ideal chain model [4]. This model allows us to calculate an important length scale within the system, \bar{R}_{ee} , which quantifies the average size of a polymer chain in the melt and is integral in determining polymer properties such as the entropy of a molecule. Using the ideal chain model, you can calculate the free energy of a chain in the melt, and find that the free energy is largely dominated by the entropy of the polymer molecule. As a consequence, it is not a surprise that temperature and chain conformations have been shown to play a pivotal role in dynamics and physical properties of polymer systems.

1.1.1 Phase separation: equilibrium and kinetics

To understand the driving forces behind the self-assembly process in diblock copolymer systems, I will first study the thermodynamics of phase separation in homopolymer blends. In this calculation the liquid-liquid unmixing transition is studied, where two polymers that are miscible at high temperatures, forming a homogeneous mixture, phase separate as the temperature is lowered. Flory and Huggins originally performed this calculation independently from one another in 1942 [6,7], however the following derivation follows what is outlined nicely by Rubinstein and Colby [3] and Jones [8].

Polymer blends

This calculation uses a mean-field approach, meaning instead of studying the effects of interactions between a large number of particles within a system, the interaction of one molecule with an average field is considered. This simplification reduces the complex many-body physics problem to a simpler one body problem and is a common method for performing calculations on diblock copolymer systems, as I will outline in section 1.2. The calculation is performed on a lattice allowing for simple counting of site occupancies to calculate possible states and interactions. In the following, I consider the mixing of two homopolymers, denoted A and B , with degree of polymerization N_A and N_B respectively. The mixture contains a total fraction of the individual polymer segments A and B in proportions of $\phi_A = V_A/(V_A + V_B)$ and $\phi_B = V_B/(V_A + V_B)$ giving $\phi_A + \phi_B = 1$.

Upon simple inspection of the Helmholtz free energy of the system, $F = U - TS$, at high temperatures entropy will dominate favouring the mixture of polymers so that every lattice site is a possible state for each monomer. However, at sufficiently low temperatures, the enthalpic penalty of interaction between the two unlike chains, U , becomes important, and the system may phase separate. The following calculation is a derivation of the free energy of mixing, $F_{\text{mix}} = U_{\text{mix}} - TS_{\text{mix}}$ where U_{mix} is the enthalpy penalty of mixing due to the interaction of the two polymers, and S_{mix} is the gain in translational entropy upon mixing

In calculating the entropy of mixing in a polymeric system, S_{mix} , the entropy is

given by the Boltzmann equation

$$S = k_B \ln \Omega, \quad (1.8)$$

where k_B is the Boltzmann constant and Ω represents the number of possible positions (states) for a segment on the lattice. Considering a lattice with n sites, in the case of a homogeneously mixed system, each segment has $\Omega_{AB} = n$ possible states available to it. However, considering the A polymer segments in the pure unmixed case, the molecules are segregated and thus the total number of lattice sites available to an A segment is reduced to $\Omega_A = n\phi_A$. Therefore, the entropy change upon mixing for a single A polymer segment is

$$S_A = k_B \ln \Omega_{AB} - k_B \ln \Omega_A = -k_B \ln \phi_A, \quad (1.9)$$

and since $\phi_A < 1$ by definition, Equation 1.9 denotes an increase in entropy upon mixing. The mixing entropy for a B segment is calculated similarly, and upon summing up the entropy gain for each polymer segment within the system, the entropy of mixing per lattice site is calculated as

$$S_{\text{mix}} = -k_B \left[\frac{\phi_A}{N_A} \ln \phi_A + \frac{\phi_B}{N_B} \ln \phi_B \right]. \quad (1.10)$$

The entropy of mixing per lattice site provides a measure that is independent of system size. It is interesting to note that this formula is directly applicable to the entropy of mixing in both polymer solutions ($N_A = N, N_B = 1$) and regular solutions ($N_A = N_B = 1$) as well.

Having calculated the entropy of mixing, I will now consider the enthalpy of mixing, U_{mix} . Only nearest neighbour interactions are considered on a lattice, assuming that interactions are pairwise additive. We represent the interaction between two neighbouring A polymer segments as ϵ_{AA} , between two neighbouring B segments as ϵ_{BB} , and between neighbouring A and B segments as ϵ_{AB} . Once again, a mean field approach is used assuming that any given site has $z\phi_A$ A neighbours and $z\phi_B$ B neighbours, regardless of whether it is occupied by an A or B polymer segment where z is the number of nearest neighbours in the system ($z = 4$ for a 2D lattice and $z = 6$

for a 3D lattice).

With this approach, the total energy per site for the mixed state is calculated as

$$\frac{z}{2} (\phi_A^2 \epsilon_{AA} + \phi_B^2 \epsilon_{BB} + 2\phi_A \phi_B \epsilon_{AB}), \quad (1.11)$$

and a total energy per site for the unmixed state of

$$\frac{z}{2} (\phi_A \epsilon_{AA} + \phi_B \epsilon_{BB}), \quad (1.12)$$

where the division by 2 in each of Equations 1.11 and 1.12 is to avoid double counting the same interaction. Combining Equations 1.11 and 1.12, a definition for the enthalpy of mixing is

$$U_{\text{mix}} = \chi \phi_A \phi_B k_B T, \quad (1.13)$$

where $\chi = \frac{z}{2k_B T} (2\epsilon_{AB} - \epsilon_{AA} - \epsilon_{BB})$ is the Flory-Huggins interaction parameter which characterizes the difference in interaction energies in the polymer blend [3,6,8]. Combining Equations 1.13 and 1.10, a description for the free energy of mixing is given as

$$F_{\text{mix}} = k_B T \left[\frac{\phi}{N_A} \ln \phi + \frac{1-\phi}{N_B} \ln(1-\phi) + \chi \phi(1-\phi) \right], \quad (1.14)$$

where $\phi = \phi_A$.

One important assumption made in the lattice model is that volume is constant upon mixing, and the packing of both monomers separately and when mixed is identical. As polymers generally pack more closely with certain monomers over others, there is a temperature independent term that should be included in the Flory-Huggins interaction parameter, χ . In general, the Flory-Huggins interaction parameter is written as the sum of two terms

$$\chi = \chi_s + \frac{\chi_H}{T}, \quad (1.15)$$

where χ_H is the “enthalpic contribution” to the parameter which was calculated above due to interactions between particles, and χ_s is an “entropic contribution” that arises due to many number of factors, one major factor being the unphysical representation of our system as an equally packing lattice. χ has been measured for a large number of different polymer blends [9], and is an integral parameter in understanding the drive to phase separate in polymer blends as well as in diblock copolymers.

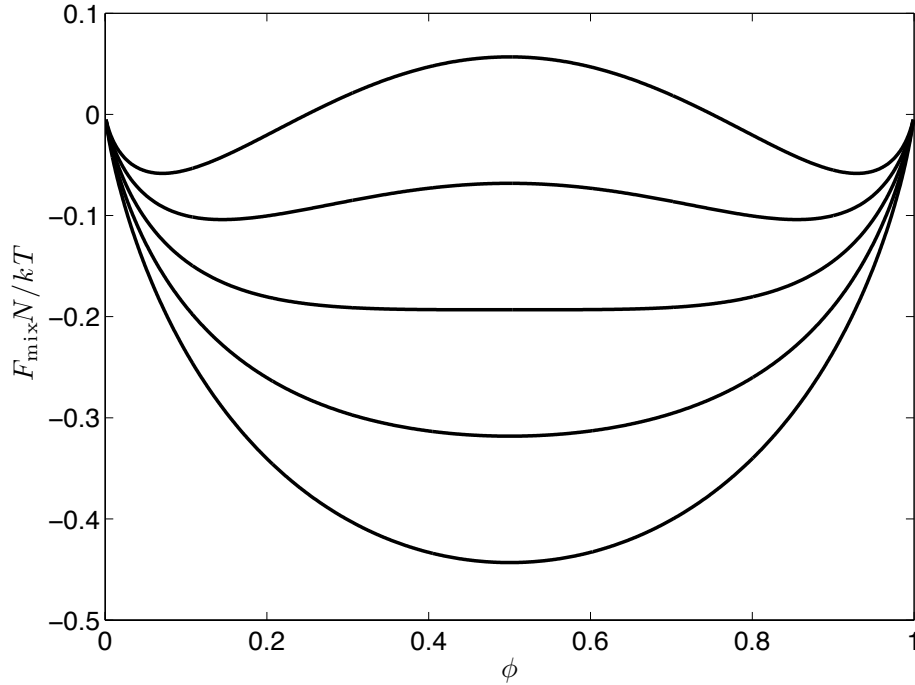


Figure 1.2: Plot of free energy per lattice site as a function of weight fraction of polymer for $\chi N = 3, 2.5, 2, 1.5, 1$ from top down when $N_A = N_B$.

Using Equation 1.14, the behaviour of a polymer blend may be described to gain physical insight on whether a blend will phase separate, and how phase separation will take place. The first two terms in Equation 1.14 are due to entropy, and always work to promote mixing (decreasing the free energy of the system), however the third term may be either positive or negative, depending on the interaction parameter, χ . If the two polymer species have an attractive interaction, $\chi < 0$, favouring mixing in the system. However, if the two species have a repulsive interaction which is more common, then $\chi > 0$. In order to develop a better understanding of the free energy of mixing, Equation 1.14 is plotted as a function of ϕ for different values of χN . In Figure 1.2 the results are shown using equal degrees of polymerization for the two polymers, $N = N_A = N_B$.

It is shown in Figure 1.2 that at $\chi N < 2$, the free energy has a single minimum at $\phi = 0.5$. Alternatively, for $\chi N > 2$, the free energy has two minima, and a maxima at $\phi = 0.5$. Considering a mixture of equal parts A and B where $\phi = 0.5$, for $\chi N < 2$, the mixture is stable, as the free energy curve is concave up such that $\frac{d^2 F_{\text{mix}}}{d\phi^2} > 0$.

Similarly, for $\chi N > 2$, compositional fluctuations about $\phi = 0.5$ provide a decrease in the free energy, and the film will phase separate into A and B rich mixtures which correspond to the two minima in Figure 1.2. This phase separation occurs because the mixed state is unstable as $\frac{d^2 F_{\text{mix}}}{d\phi^2} < 0$, and the free energy curve is concave down. The crossover in behaviour from globally stable to globally unstable occurs when the common tangent of the free energy curve minima are equal, or in other terms

$$\left(\frac{dF}{d\phi}\right)_{\phi=\phi_1} = \left(\frac{dF}{d\phi}\right)_{\phi=\phi_2}, \quad (1.16)$$

where ϕ_1 and ϕ_2 are the two minima, as indicated in Figure 1.3a for $\chi N = 3$. For the simple example of a blend with equal length polymers, $N = N_A = N_B$, this corresponds to a χN dependance on ϕ of

$$(\chi N)_{\text{bi}} = \frac{1}{2\phi - 1} [\ln \phi - \ln(1 - \phi)], \quad (1.17)$$

where $(\chi N)_{\text{bi}}$ is commonly referred to as the *binodal line*, the line which separates globally stable mixtures from those which are globally unstable.

The other crossover behaviour of interest is that where the mixed state becomes completely unstable, or $\frac{d^2 F_{\text{mix}}}{d\phi^2} = 0$. This signifies the inflection points of the free energy curve, identifying the boundary between locally stable to locally unstable mixtures. In our model, this corresponds to

$$(\chi N)_{\text{sp}} = \frac{1}{2} \left[\frac{1}{\phi} + \frac{1}{1 - \phi} \right] \quad (1.18)$$

where $(\chi N)_{\text{sp}}$ is referred to as the *spinodal line*. In Figure 1.3 (bottom), the complete phase diagram for this polymer blend system is shown. A plot of the free energy as a function of ϕ for a blend with $\chi N = 3$ is shown in Figure 1.3 (top) for reference as to where the transition between regions of different stability occur. It is important to note here that the binodal and spinodal lines separate the phase diagram into regions of varying stability. The binodal line separates the diagram into regions of equilibrium phase separated mixture for $\chi N > (\chi N)_{\text{bi}}$, and mixed phase for $\chi N < (\chi N)_{\text{bi}}$ (ϕ_1 and ϕ_2 in Figure 1.3a). Similarly, the spinodal line separates the phase separated mixtures into metastable regions for $\chi N < (\chi N)_{\text{sp}}$ and unstable for $\chi N > (\chi N)_{\text{sp}}$ (ϕ_{sp1} and

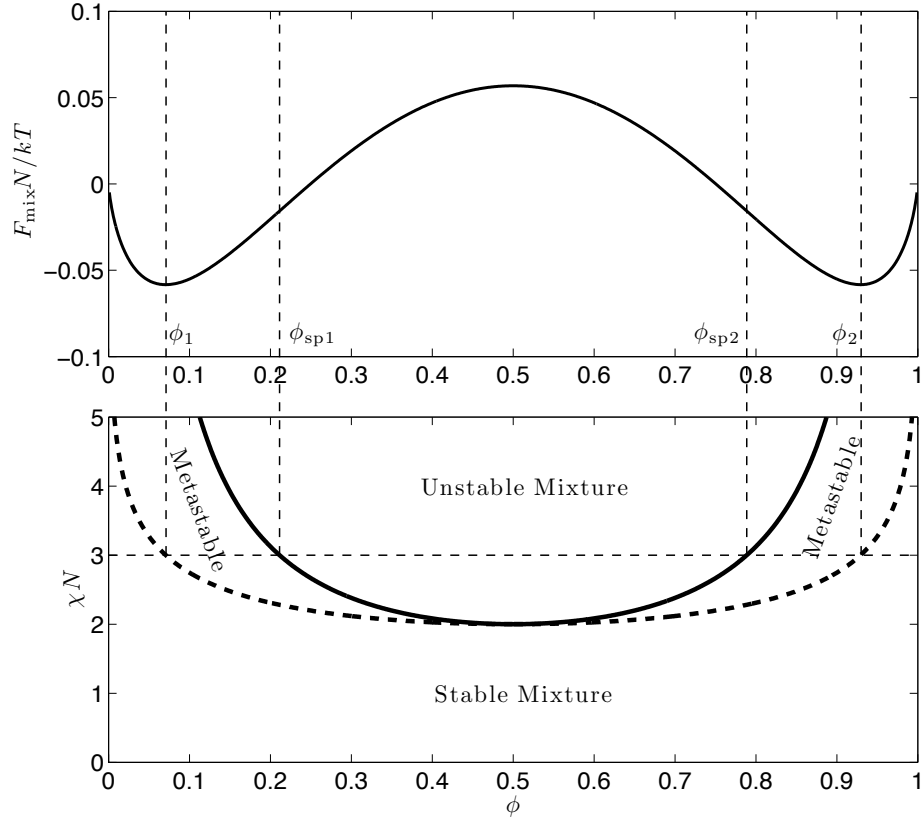


Figure 1.3: a) Free energy per lattice site for $\chi N = 3$ in relation to b) the phase diagram for mixing stability of polymer blend with $N_A = N_B = N$. ϕ_1 and ϕ_2 represent the binodal points, and $\phi_{\text{sp}1}$ and $\phi_{\text{sp}2}$ represent the spinodal points for $\chi N = 3$.

$\phi_{\text{sp}2}$ in Figure 1.3a). The stability of the mixed phase will determine the kinetics of phase separation, ultimately playing a role in determining the final morphology of the phase separated state. The metastable and unstable regions will separate via *nucleation and growth* or *spinodal decomposition* respectively. These two mechanisms of phase separation apply to a wide range of phase transitions including but not limited to crystal growth [5], dewetting of films [10–13], and in relation to the research contained within this dissertation, the break-up of liquid jets [14] and the transition between various ordered diblock copolymer phases [15–17]. A discussion of the growth kinetics in nucleated and spinodal systems is discussed in the following sections.

Nucleation and growth

When a blend system is in a metastable state, the system is stable to compositional fluctuations which are sufficiently small. However, a large enough composition fluctuation can overcome the free energy barrier required to escape the local free energy minimum, forming a domain of the equilibrium composition which grows in size. Thus, these equilibrium domains must be *nucleated* by thermal fluctuations in the system. To understand the general case of nucleation and growth, I will discuss the classical nucleation theory which describes this activated process.

Let us first consider the growth of a spherical equilibrium composition domain with radius r out of a metastable phase. We can estimate the free energy change, ΔF , which results from the nucleation of this droplet. There is a decrease in the free energy that is proportional to the droplet volume, $\frac{4}{3}\pi r^3$, due to the favourable formation of the droplet in the lower free energy equilibrium state. However, there is an energy cost associated with the additional surface created between the metastable phase and the equilibrium droplet which can be written as an energy cost per unit area, or surface tension, γ . Thus, the equation for the change in free energy by creating a droplet with radius r is

$$\Delta F(r) = 4\pi r^2 \gamma - \frac{4}{3}\pi r^3 \Delta F_V, \quad (1.19)$$

where ΔF_V is the change in free energy per unit volume between the metastable and equilibrium phases. Both γ and ΔF_V are positive quantities, and thus the first term is strictly positive, favouring smaller r , while the 2nd term is negative, favouring increasing r . The droplet size that gives the maximum free energy increase can be calculated by differentiating Equation 1.19 and equating to zero. The droplet size at maximum, r^* is then

$$r^* = \frac{2\gamma}{\Delta F_V}, \quad (1.20)$$

and substituting r^* into Equation 1.19, the energy barrier to nucleation, ΔF_V^* is shown to be

$$\Delta F_V^* = \frac{16\pi\gamma^3}{3\Delta F_V^2}. \quad (1.21)$$

Equations 1.20 and 1.21 identify that for compositional fluctuations with size

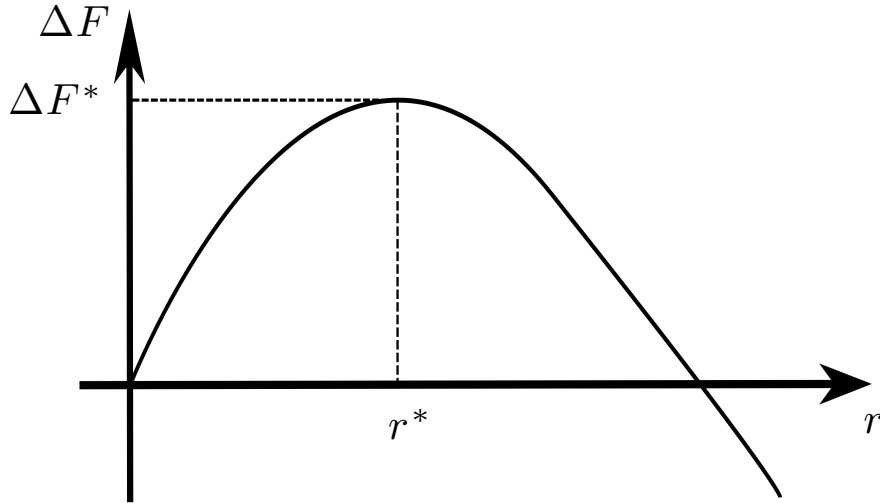


Figure 1.4: A schematic of nucleation parameters and the energy barrier to nucleation.

greater than r^* , the global free energy will decrease if the droplet grows in size, promoting a change in phase. However, for fluctuations with size smaller than r^* , the droplet is unstable and will dissolve. The energy barrier to this process is ΔF_V^* , making this an activated process where the probability of a nucleated domain being bigger than r^* and growing is proportional to the Boltzmann factor, $\exp(-\Delta F^*/k_B T)$ [8].

I note here that this calculation is under the assumption that there is homogeneous nucleation, where the energy barrier is defined simply by the energy considerations between the two phases. In the case of a completely homogeneous system, this nucleation will occur randomly throughout the sample, independent of location. However, in practice, heterogeneous nucleation is more likely to occur, nucleating primarily around defects which lower the activation energy barrier. In the case of heterogeneous nucleation, though the probability of nucleating near defects is increased due to the lower energy barrier, the dynamics are still governed by the nucleation of individual domains which will grow in time, contrasting with the unstable formation of domains in spinodal decomposition.

Spinodal decomposition

If a system is within an unstable region in the phase space, then any small local fluctuation in composition will be amplified, causing a decomposition of the material into stable phases. However, not all wavelengths of fluctuation grow at the same rate. In the case of long wavelength fluctuations, the material must flow over large lateral distances, slowing down the phase separation process. Conversely, in the case of short wavelength fluctuations, there is a large amount of excess surface area created which can counteract the process of phase separation due to the high surface energy cost. Therefore, there must be an optimal wavelength of composition fluctuation that will grow the fastest, balancing surface energy cost and length scale of flow. This will cause domains to grow randomly as in the nucleated and growth case, however with a characteristic wavelength that is related to this optimal wavelength. This growth process is generally identified by correlated domains in the final state which are related to this optimal wavelength [8].

In order to develop a quantitative understanding of this spinodal process, I will discuss a calculation initially performed by Cahn and Hilliard more than 50 years ago [18]. I perform the calculation for simplicity in one dimension, however the same physics is observed in two and three dimensions [19]. In this calculation, the difficulty arises due to the fact that interfaces are not sharp in the initial stages of phase separation, making it unphysical to denote a surface energy cost per unit area for these interfaces [8]. Instead, Cahn and Hilliard proposed a free energy which depended on the local composition, ϕ , but with an added dependence on the gradient of the composition. In this way, they defined the free energy as a function of ϕ such that

$$F = \int \left[f_0(\phi) + \kappa \left(\frac{d\phi}{dx} \right)^2 \right] dx, \quad (1.22)$$

where $f_0(\phi)$ is the free energy per unit volume of a homogeneous mixture, and κ is the gradient energy coefficient. This equation is phenomenological, making it applicable to a wide variety of systems [8].

In the case of phase separation of A and B domains consideration is given to the chemical potential, μ , which represents the change in free energy upon removing an A molecule and replacing it by a B molecule. The chemical potential is calculated by

taking the derivative of the free energy density, f , in the integrand of Equation 1.22 with respect to concentration such that [8]

$$\mu = \frac{\partial f}{\partial \phi} = \frac{\partial f_0}{\partial \phi} + 2\kappa \frac{\partial^2 \phi}{\partial x^2}. \quad (1.23)$$

The chemical potential is what drives diffusion in phase separating systems, as it represents the free energy changes upon changing concentration profiles of the A and B molecules. Therefore, a linearized diffusion equation can be used to study the decomposition of an unstable mixture [8]. Note that due to linearization of the equation, this will only be valid in the initial stages of decomposition when deviations from the initial state are small. The result is the Cahn-Hilliard equation

$$\frac{\partial \phi}{\partial t} = M f_0'' \frac{\partial^2 \phi}{\partial x^2} + 2M\kappa \frac{\partial^4 \phi}{\partial x^4}, \quad (1.24)$$

where M is the Onsager coefficient (a measure of mobility). Equation 1.24 represents a modified diffusion equation for the initial stages of phase separation [19]. Though it is quite complex, the solution to Equation 1.24 may be verified to be of the form

$$\phi(x, t) = \phi_0 + \epsilon \cos(qx) \exp \left[-D_{\text{eff}} q^2 \left(1 - \frac{2\kappa q^2}{f_0''} \right) t \right], \quad (1.25)$$

where q represents the wave vector of the composition fluctuation and $D_{\text{eff}} = M f_0''$ is the effective diffusion coefficient [8]. Equation 1.25 tells us that for fluctuations with wavelength $\lambda = 2\pi/q$, the composition fluctuation will grow with an amplification factor, $R(q)$ equivalent to the term in the exponential,

$$R(q) = -D_{\text{eff}} q^2 \left(1 - \frac{2\kappa q^2}{f_0''} \right). \quad (1.26)$$

The largest amplification factor is thus when $q_{\text{max}} = \sqrt{\frac{f_0''}{2\kappa}}$, giving the fastest growing wavelength as $\lambda_{\text{max}} = 2\pi/q_{\text{max}}$.

Spinodal decomposition is commonly recognized experimentally by taking a Fourier transform of a 2D image, resulting in a ring of intensity corresponding to the length scale which matches q_{max} [8, 12, 13]. However, since this calculation has been per-

formed using a linear model, which only describes the early portions of phase separation, the final wavelength is often shifted toward longer wavelengths (smaller q values in Fourier space) due to coarsening of A and B rich domains. The important distinction between the two phase separation mechanisms is that in contrast to the random domains formed via the nucleation and growth mechanism, spinodal decomposition results in an experimentally measurable spatial correlation in phase separated domains. The spinodal ring in the Fourier transform and the shift in wavelength on coarsening are important concepts for the study performed in Manuscript II (see Section 3.2).

1.1.2 Time-temperature superposition

Due to the subject matter in Manuscript IV (section 3.4), an aside must be made to discuss the effect that temperature can have on the flow properties of polymer melts. The following is taken from Ref. [9] and [20]. It was shown in a study by Williams, Landel and Ferry in 1955 that when measurements were made on polymers at various temperatures, T , the viscosity could be related through a shift factor, a_T , according to the relation

$$\frac{a_{T_1}}{a_{T_2}} = \frac{\eta_{T_1}}{\eta_{T_2}}, \quad (1.27)$$

where η_{T_1} and η_{T_2} are the viscosities of the polymer at temperatures T_1 and T_2 respectively. The shift factors may be calculated using an empirical relationship developed by Williams, Landel, and Ferry such that

$$\log a_T = -\frac{C_1(T - T_0)}{C_2 + (T - T_0)}, \quad (1.28)$$

where C_1 and C_2 are empirical constants and T_0 is the chosen reference temperature. Typically, C_1 , C_2 , and T_0 are found empirically through bulk rheology measurements where the frequency response at various temperatures is measured and constants are found that will align all data to a single master curve [20]. This relationship relies on the assumption that all curves will have the same characteristic time variation with temperature, as is the case in polymer melts. As a consequence, the timescales for

experiments performed at different temperatures are equated through the relation

$$t_1 = \left(\frac{a_{T_1}}{a_{T_2}} \right) t_2, \quad (1.29)$$

where t_1 and t_2 are timescales for experiments performed at T_1 and T_2 respectively. This is quite remarkable, as it allows one to experiment at different temperatures, probing a wider range of dynamic responses, yet relate all measurements on one master plot. In the case of the shear rate experiments discussed in Manuscript IV (section 3.4), it allows for a broader range of shear rates to be probed for the same material, as upon construction of the master curve, experiments at different temperatures probe different regions of shear rate response. It is worth noting here that the experiments which are generally performed to determine these shift factors, bulk oscillatory shear rheology experiments, exhibit a shear thinning property for polymer melts for sufficiently high frequencies of oscillation [21]. As well, it is important to note that Equation 1.27 is only valid for temperatures that are within 100 °C of the glass transition.

1.2 Diblock copolymers

The preceding description of the statics and dynamics of phase separation in binary systems, though simplistic in its assumptions, describes the physics of phase separation very well. I will now build upon this understanding of macrophase separation (phase separation on a global scale), in order to understand the microphase separation which occurs for the molecules that are the main topic within this thesis, diblock copolymers.

1.2.1 Equilibrium

When a polymer is composed of 2 or more different monomer repeat units, the molecule is referred to as a block copolymer. Block copolymers may be fabricated with a wide variety of different configurations and any number of different monomer units. However, the main subject of this thesis is one of the simpler copolymer molecules, the diblock copolymer, where two linear homopolymer molecules are covalently bonded

together to form a chain as shown in Figure 1.5. As in the case of a polymer blend, due to the chemical distinction between the two polymer blocks, they generally do not mix favourably. However, the connectivity of the two blocks makes the macrophase separation described previously impossible, and thus phase separation can only be achieved on the molecular level, resulting in a vast array of nanosized self-assembled architectures [2, 22]. Owing to the small length scale of organization there is interest in various technological applications for diblock copolymers including nanolithography [23], biomolecule patterning [24], and surface property modification [25, 26]. As well, there has been significant interest in diblock copolymer systems for research as a model system for pattern formation and self assembly of amphiphilic molecules in nature such as membranes [27, 28] and vesicles [29–31].

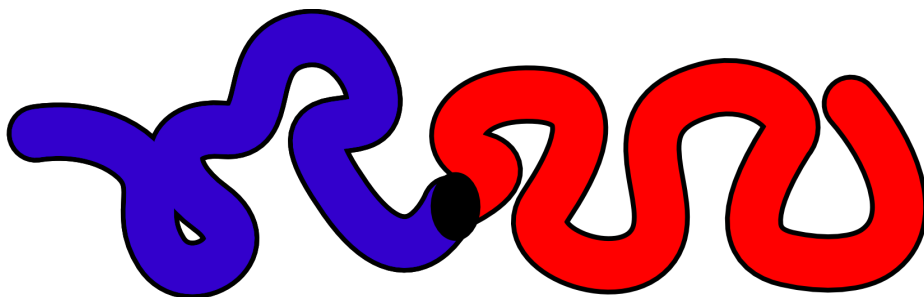


Figure 1.5: A schematic of a diblock copolymer molecule.

In the case of diblock copolymers, the equilibrium structure in the melt state is determined by 2 parameters: the relative fraction of the A block in the diblock chain, f , and the parameter discussed in regards to phase separation denoting the temperature dependent Flory-Huggins interaction parameter, χN . As in the case of phase separation in polymer blends, for small χN (high temperatures), entropy dominates and the diblock prefers to be in a homogeneous disordered state. Conversely, for large χN (low temperatures), the system prefers to phase separate into self-assembled structures determined by f , where the 3 simplest domain structures are shown schematically in Figure 1.6. In the case of a symmetric diblock copolymer, the main focus of this thesis, the chains assemble into a lamellar structure (Figure 1.6a), with well defined bilayer thickness, L_0 . As the relative fraction of the A block is decreased, the lamellar structure becomes less preferable. This is caused by the fact that in order to accommodate the shorter A block, the B block must stretch, adding

an entropic cost to the lamellar morphology. However, if the interface is curved, such that the shorter blocks may assemble into smaller regions, then both blocks may be stretched equal amounts. This naturally occurring interface curvature is what induces the transition to hexagonally packed cylindrical domains where the shorter chains assemble into long cylinders (Figure 1.6b). Similarly, for even greater asymmetry in block lengths, a transition to body centred cubic spheres will occur (Figure 1.6c) where the shorter block forms the spheres [2]. Other more complex phases are also observed under varying conditions of χN and f . Some examples are the gyroid phase, which is a known stable phase in the region between lamellae and cylinders in systems with lower χN [32], or the perforated lamellae phase, a metastable phase observed in Manuscript III (section 3.3) that has been observed both in film [33] and bulk systems [34].

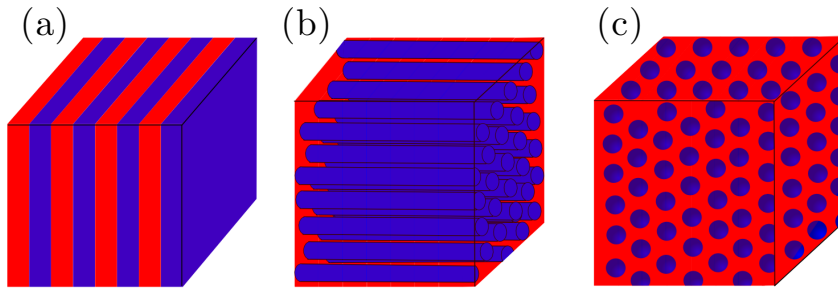


Figure 1.6: Schematic depicting the simple phases of a linear diblock copolymer.

The calculation of block copolymer phases, and when ordered their organizational spacing, can be accurately predicted if their free energy is known [32,35–39]. There are a number of viable theories of diblock copolymer structures, each valid under different conditions. The simplest calculation is performed in the regime where the diblock copolymers are strongly segregated ($\chi N \gg 1$). In this model, the assumption is made that the interface between the regions of varying blocks is very thin, with very little mixing between the A and B rich domains [8, 35, 36]. In the case of a very thin interface, the assumption is made that the interface between the two regions gives rise to a simple energy cost per unit area, γ_{AB} . We estimate the width, w , of this very thin interface by considering that some segment of chain monomers of polymer

A , N_{seg} , will protrude into the B rich domains. Assuming that this chain segment follows a random walk, like an ideal chain, then the width will be on the order

$$w \sim a\sqrt{N_{\text{seg}}}, \quad (1.30)$$

where a is simply the size of a chain monomer. The energy cost of interfacial width is simply given as the enthalpic energy cost, U_{enth} due to the interaction between the two blocks as

$$U_{\text{enth}} \sim \chi N_{\text{seg}} k_{\text{B}} T. \quad (1.31)$$

However, at equilibrium, $U_{\text{enth}} \approx k_{\text{B}} T$, giving the relation $N_{\text{seg}} \sim \frac{1}{\chi}$. In combination with Equation 1.30, that gives an interfacial width between the A and B domains of

$$w \sim \frac{a}{\sqrt{\chi}}. \quad (1.32)$$

Using Equation 1.32, the energy cost per unit area of interface is calculated by recognizing that there are w/a^3 segments per unit area at the interface, and thus the interfacial energy cost per area, γ_{AB} is

$$\gamma_{AB} = \frac{w}{a^3} \chi k_{\text{B}} T = \frac{\sqrt{\chi} k_{\text{B}} T}{a^2}. \quad (1.33)$$

Though this calculation is rather simplistic, and more sophisticated calculations of the interfacial width are possible [35, 36], Equations 1.32 and 1.33 provide a clear demonstration of the physics within the strong segregation regime, and provide an accurate result that has been measured to be correct within a numerical pre factor [36].

Using this interfacial cost per unit area, I now discuss a calculation which can be used in the strong segregation limit to study the equilibrium length scale of patterning in a diblock copolymer melt. As stated earlier, the equilibrium bilayer width, L_0 of a lamellar forming symmetric diblock copolymer is well defined. The free energy of the system may be thought of as a combination of an elastic component, F_{el} , and an interface component, F_{int} . The elastic portion of the free energy may be described by considering the entropic penalty for stretching calculated in Equation 1.7, giving us

an elastic free energy cost per chain of

$$F_{\text{el}} \sim k_{\text{B}}T \frac{l^2}{Na^2}, \quad (1.34)$$

where l represents the length of the polymer chain in the organized lamellar phase [8]. The interfacial cost per chain may be calculated as

$$F_{\text{int}} = \frac{\gamma_{AB}Na^3}{l}. \quad (1.35)$$

By minimizing the sum of F_{el} and F_{int} , and using the definition of γ_{AB} in Equation 1.33, the equilibrium chain length, l_{eq} , is shown to be

$$l_{\text{eq}} \sim a\chi^{1/6}N^{2/3}, \quad (1.36)$$

where l_{eq} scales as $N^{2/3}$. This scaling is different compared to the ideal polymer case in the melt with an increased exponent of N indicating the chains are more stretched than in the ideal case due to the repulsive interaction between the A and B blocks.

It is important to note that while this scaling law is valid in the strong segregation limit ($\chi N \gg 1$), the assumptions within the model are quite extreme. Though the scaling has been verified in experiment [40, 41], it is only applicable in the limits where we approach infinitely long chains and the interface is extremely thin between the A and B domains. However, it is obvious that in the disordered phase, A and B monomers will mix, and near the order-disorder transition (ODT), it is expected that there is significant incursion of A monomers into primarily B regions and vice versa. In order to understand this weak segregation of domains, Leibler developed a theory that would correctly describe this diffuse interfacial width between A and B domains for weaker segregation regimes [38].

A full description of Leibler's calculation is beyond the scope of this thesis, and the complete calculation may be found in the original article by Leibler, Ref. [38]. However, a summary of the important results of the calculation is warranted. The calculation uses a mean field theory approach, defining an order parameter, $\phi(r)$, which describes the change in A monomer density from that of the homogeneous, disordered state. Performing a Landau expansion and using a random phase ap-

proximation of ideal chains, he was able to successfully calculate a phase diagram detailing stable phases of lamellar, cylinder and sphere forming diblock in the vicinity of the ODT. The calculation was also able to identify the interaction parameter for symmetric diblocks where the ODT occurs at $(\chi N)_{\text{ODT}} = 10.495$. This is in direct comparison to the interaction parameter of $\chi N = 2$ that was found for the ODT of symmetric homopolymer blends in Section 1.1.1. However, a major issue with the weak field calculation by Leibler was that it does not take into account the effects of fluctuations due to thermal energy. This effect is negligible for infinitely long chains, however in the case of finite length chains, this effect is important near the ODT. A correction factor was calculated by Fredrickson and Helfand (Ref. [42]) that identified the ODT for a symmetric diblock to be located more accurately at $(\chi N)_{\text{ODT}} = 10.495 + 41.022N^{-1/3}$. Note that in the limit of infinitely long chains, Leibler's result is recovered as should be expected. The main issue with Leibler's calculation is that similar to the strong segregation theory, it is only valid in a narrow phase space region, close to the ODT, where diblock copolymers are weakly ordered. This is the same issue experienced with the strong segregation theory proposed by Semenov [35], where the theory is only valid in the other extreme case of nearly perfect segregation. Therefore, a theory was needed to bridge the gap between these two extremes.

Self-consistent field theory (SCFT) has been well established as the theory which can be used to unite the weak and strong segregation regimes [32, 39, 43–48]. A complete description of SCFT would be beyond this thesis, and thus only a brief description of the important points are presented herein. In SCFT, as in other mean field theories, the system is modelled as a single polymer chain in a field created by the concentration of other polymer chain blocks. Given an initial state for the field and boundary conditions, a modified diffusion equation is solved in order to calculate the concentration profiles by studying possible chain conformations in the field. This concentration profile is then used to recalculate the field and the entire process is iterated until a convergence criteria is reached. The result is a concentration profile describing the diblock copolymer phase at equilibrium. SCFT is successful in not only bridging the gap between the weak and strong segregation regimes [49], but also provides an exact solution to the mean field theory rather than the approximated

results from the weak and strong segregation theories. SCFT was the first theory to be able to correctly assess the stability of complex phases such as gyroids and perforated lamellae in comparison to the simple phases of lamellae, cylinders and spheres [32, 50]. The main drawback to traditional SCFT is its inability to treat thermal fluctuations, thus providing a poor description of the disordered state of diblock copolymer [47]. However, progress has been made through recent advances in this field, providing the ability to treat fluctuations in calculations [51]. These recent results have been successful in confirming the treatment of fluctuations noted previously by Fredrickson and Helfand, with $(\chi N)_{\text{ODT}} \propto N^{-1/3}$ [42].

In summary, due to the preference for phase separation of their two block components, diblock copolymers self assemble into ordered assemblies of varying morphologies. Simple equilibrium morphologies of lamellae, cylinders and spheres are understood with approximate theories for weakly or strongly segregated polymers, however the exact theory of SCFT has provided the ability to assess stability in more complex systems [47]. Though the equilibrium phases in diblock copolymer melts are well understood, the ordering of diblock copolymers under various different confinements, and the effect of this ordering on system dynamics, is still an area of much interest.

1.2.2 Interfacial effects

When diblock copolymers are confined, the difference in interface surface energies of the two polymer blocks are known to play a significant role in the ordering process [52–64]. Various different confinement geometries have been studied and shown to play an important role on the unique morphologies formed including, but not limited to, cylindrical confinement [61, 62], spherical confinement [63], channel confinement [64], or the geometry used for the bulk of work within this thesis, film confinement [52–60]. Symmetric diblock copolymer films have been studied at length in order to understand how equilibrium microphase separated morphologies are altered in the presence of interfaces, leading to a number of excellent reviews of the topic [58, 65–67]. When there is a difference in surface energies between the two blocks, as is usually the case when working with surfaces that are not specifically modified to reduce interaction [25], the lower energy block will preferentially segregate to that interface. In the case

of symmetric diblock copolymer films, this preferential interaction gives rise to an alignment of lamellae parallel to the interfaces, exposing only the lower surface energy block at each surface. This preferential interaction not only determines the orientation of the ordered structure but has also been found to induce ordering near interfaces, even for systems in the bulk disordered state [54–57, 59].

As discussed earlier, symmetric diblock copolymers microphase separate into lamellae with a well defined bilayer thickness, L_0 , due to the balance of entropic and enthalpic free energy terms. Thus, the parallel alignment of lamellae due to interfacial interactions gives rise to a system frustration when the film thickness is not commensurate with the necessary number of lamellar monolayers. The preferred equilibrium thickness, referred to as the commensurate thickness, of a symmetric diblock copolymer film, h_{comm} , is defined as

$$h_{\text{comm}} = \frac{\nu L_0}{2}, \quad (1.37)$$

where ν is an integer denoting the number of monolayers in the film and is determined by the boundary conditions. In the case where the same block has lower surface energy at both interfaces, known as the symmetric boundary conditions, ν is even in Equation 1.37. Conversely, if a different block has lower surface energy at each interface, termed asymmetric boundary conditions, then ν is odd. Films with thicknesses that satisfy this commensurability condition ensure that both surface interactions and the energetics of equilibrium bilayer thickness are satisfied [58, 65, 66].

In the case of capped thin films of symmetric diblock copolymers, it has been found that film morphology becomes frustrated when films are prepared that are not commensurate [68–72]. In these studies, the structure of the diblock order was investigated by theory [69], simulation [70] and experiment [68, 71, 72] for symmetric diblock films confined between two hard substrate walls. Both simulation and theory predicted the conformations to remain parallel for moderate incommensurability, but to revert to perpendicularly oriented lamellae in the middle of sufficiently thick films which were maximally incommensurate (See Figure 1.7). However, it was found that except in cases which exhibited weak surface preferences [72], the surface energy dominated the lamellar order, maintaining parallel lamellae with expanded or compressed bilayers. In the case of expanded bilayers, copolymers are stretched, increasing the entropic free energy term, whereas when bilayers are compressed, extra interface is

created between domains, increasing the enthalpic cost. Regardless, by confining these films between two substrates, parallel morphology of non-equilibrium lamellae persisted for films with thickness greater than 9 lamellar layers [68, 71], once again alluding to the fact that surface interactions play a dominant role in determining thin film morphologies.

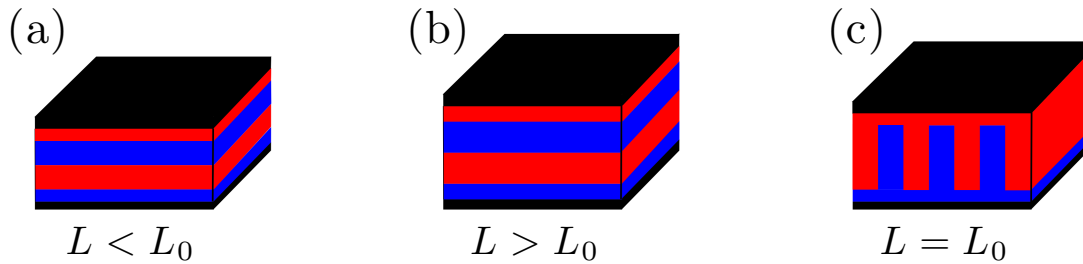


Figure 1.7: Schematic displaying the morphologies of capped symmetric diblock thin films with a) compressed lamellae ($L < L_0$), b) expanded lamellae ($L > L_0$), and c) perpendicular lamellae ($L = L_0$).

For a supported film, where one interface is in contact with a hard substrate and the other is unconfined, the equilibrium morphologies are quite different. Similar to the capped thin film case, the film prefers to be ordered with thicknesses that correspond to Equation 1.37. However, in the case of a supported film, since the one surface is free to deform, the film will separate into regions of commensurate thickness while conserving volume [58, 65]. This results in a film surface that has a terraced structure, with higher regions equivalent to $\nu + 2$ in Equation 1.37 (islands) and lower regions of ν (holes) (See Figure 1.8). The growth of islands or holes at the surface of the film creates excess surface area at the edge of the features which costs energy, however it provides a film which satisfies both surface preferences and the entropic and enthalpic energy balance that determines lamellar thickness. The total incommensurability of the disordered film thickness determines the area fraction of islands and holes at equilibrium through volume conservation. Though this equilibrium morphology of symmetric diblock thin films is well understood, the dynamics by which surface features grow is a complex topic with many unanswered questions and is the focus of Manuscripts I and II (sections 3.1 and 3.2).

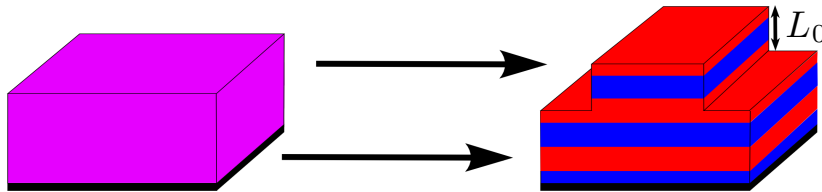


Figure 1.8: Schematic displaying the morphology of incommensurate symmetric diblock films.

The growth of terraced structures at the free surface of supported symmetric diblock copolymer films has been studied for films which have been prepared in the disordered homogeneous state [53, 72–79]. It is known that upon annealing, these films order lamellae at the strongest interacting interfaces first [53]. For incommensurate films, it has been observed that the growth mechanism for terraced structures may occur via nucleation [73, 77, 78] or spinodal decomposition [74, 75, 77]. However, though various experiments provide evidence of nucleation and spinodal mechanisms, a complete description of the dynamics for either mechanism has not been generally described and tested. In our work, using the same diblock copolymer in both studies, we examine in detail both the nucleated (Manuscript I) and spinodal (Manuscript II) growth dynamics of islands and holes.

1.2.3 Order-order transitions

The study of various order-order transitions has been a focus of diblock research over the last decade or so. The goal of the bulk of this work is to understand the kinetics of phase transitions between different ordered morphologies [15–17, 33, 45, 60, 76, 80–89]. Understanding these kinetics behind ordering is valuable in helping to optimize processes which influence ideal morphological conformations while understanding more clearly the various properties that are dependent on diblock copolymer morphologies [90].

A major result of the work performed using theory and simulation has been that the transition from one morphology to another often exhibits an epitaxial growth

mechanism [16, 17, 81, 84, 89]. The term epitaxial originated in crystal growth studies, where it refers to the growth of crystals on substrates which influence structure and orientation [91]. In terms of the order-order transition (OOT) of diblock copolymer films, it refers to the growth of one phase from another such that orientation of the order is preserved. As an example, in the cylinder to sphere packing transition of diblock copolymers, it has been theorized that spherical domains will grow through the break up of cylinders into spheres with a characteristic wavelength [84], similar to the Plateau-Rayleigh instability I will discuss in Section 1.3.1. As a consequence, the new sphere domains are aligned along the direction of the cylinder axes. Similarly in the cylinder to lamellar transition, simulations have shown a growth of lamellae along rows of cylinders and vice-versa [89] in agreement with theory [16]. Similar epitaxial growth patterns have been predicted in the cylinder to gyroid [81] transition as well as others [17].

A great deal of work has been performed looking at these OOT's in the bulk [15–17, 33, 45, 80–87, 89], however for the work contained within this thesis, it is the study of thin films that is of primary interest [60, 76, 88]. In particular, the work performed by Koneripalli et al. (Ref. [76]) is of direct relevance for understanding the dynamics of symmetric diblock copolymers in thin films and understanding the effect of non-equilibrium order on the formation of surface relief structures as described in Section 1.2.2. In this work, the authors equilibrated incommensurate capped films into morphologies of expanded or compressed lamellae, then removed the capping surface to produce a free interface. They found that in the case of the energetically frustrated order of compressed lamellae, the growth of holes occurred with a fractal dimension of 1.67 [76]. In the work by Ly et al. (Ref. [88]), the effect of electric field on the ordering of thin films was studied using SCFT, probing an OOT from perforated lamellae to aligned cylinders. In addition to electric fields, a number of other force fields (magnetic, shear, flow, etc.) have been utilized alter block copolymer long range orientational order. In particular, the effect of shear rates on the alignment of lamellae and cylinders has been the focus of a great deal of research, and warrants a discussion in relation to the work performed within this thesis.

1.2.4 Shear effects

Shear forces are known to have a significant effect on the phase separation in polymer blends [92,93] and polymer solutions [94,95], so it is not surprising that shear forces can alter the ordering of microphase separated diblock copolymers as well. Symmetric diblock copolymers when annealed below the ODT in the bulk will form lamellae as discussed before, but the orientation of these lamellae is isotropic throughout the sample when sample sizes are large enough that surface interactions do not play a significant role [2]. As a consequence, there is no long range order within symmetric diblock copolymer systems unless some action is taken during the sample preparation process to align domains.

It has been observed that in the case of symmetric diblock copolymer melts, lamellar domains may become aligned in the direction of the shear strains applied by large amplitude oscillatory shear [96,97] and steady shear [98]. In these studies it was observed that for low frequency shear, or low shear strain rates, lamellar orientation is unaffected. However, for large enough shear strains, the lamellae tend to align with the shear strain direction such that the normal to the lamellar plane is pointing perpendicular to the shear strain field. These results have been confirmed using simulation, with transverse lamellar domains (domains with lamellar planes that have a normal that is parallel to the shear) being aligned through the application of large enough shear rates [99].

The alignment of lamellar domains in thin films of diblock copolymer is of technological importance for various nano-patterning applications [100]. As discussed in Section 1.2.2, lamellar forming diblock copolymers typically align parallel to the substrate when there is a preferable interaction with one of the two polymer blocks. However, when the surface is modified to be a neutral substrate, such that neither block is preferred at the interface, then incommensurate films may align lamellae perpendicular to the substrate [25]. Similar to in the bulk case, thin films of perpendicular lamellae will exhibit an isotropic orientation in lamellar domain order, albeit now confined to two dimensions, which is undesirable for technological application [100]. Success in obtaining long range orientational order through alignment of lamellar domains has been achieved through the application of shear strain rates [101,102]. Similar to the case of lamellar ordering diblock copolymer in the bulk state, lamellae

tend to align such that their normals are oriented perpendicular to the flow field, resulting in perpendicular domains aligned in the direction of the applied strains.

Experiments have also been carried out on symmetric diblock copolymers which are in the homogeneous disordered state. In these experiments, it has been observed that the temperature for the isotropic to lamellar transition is increased [98, 103, 104]. In other words, as shear strain rates are increased, a homogeneous disordered lamellar copolymer can order under shear. These experiments have been confirmed using simulation [105], and imply a strong desire for lamellae to align in the direction of shear strain rates, even in the bulk disordered state.

Due to a number of different external forces, interfacial effects, and self-assembly energetics, a variety of different diblock conformations and kinetics can be probed. Though equilibrium phases are quite well understood, there is still a great deal to be understood about how these structures form, and how the final morphology structures and orientations are affected by different initial conditions and preparation procedures.

1.3 Liquid Jets and Bridges

If you have ever observed a thin jet of water streaming from your kitchen faucet, you may have noticed that the initial cylindrical jet of liquid breaks up into individual droplets before it hits the basin of the sink [14]. Similarly, when you place a droplet of liquid between two surfaces, like some saliva between your fingers, if you separate the surfaces you can create a liquid bridge that spans the separation distance. If this bridge is thin enough in comparison to its length, it will be unstable and thin out, eventually breaking up into individual droplets on each surface [106]. These systems of liquid jets and bridges provide an interesting platform for studying dynamics in liquid systems. The instabilities in these geometries give rise to strain rates which are quite different than in typical bulk and thin film systems due to the axisymmetric geometry. As well, by adding small amount of very long polymers, as is the case with mucosacchirides in your saliva, a stability within very thin fibers occurs due to a viscoelastic effect of polymers in axisymmetric shear strain rates [107]. I will start with a discussion of the surface tension and Laplace pressure that give rise to

the instabilities of liquid jet and bridge geometries for simple Newtonian liquids, and then discuss the effect that the elastic nature of polymer chains has on dynamics within these geometries.

1.3.1 Newtonian liquids

In order to understand the instabilities that arise within liquid jet and bridge systems, I will consider the driving forces behind these dynamics for simple Newtonian liquids (ie. constant viscosity liquids). The following closely follows arguments made by the authors of Ref. [106]. As per the discussions on polymer blends and nucleation in Section 1.1.1, all liquid-liquid or liquid-gas systems have an energy cost per unit area of interface that is called the surface tension, γ . The general definition of the surface tension is that it is the energy cost of increasing the surface area by one unit, or in equation form

$$\gamma = \left[\frac{\partial F}{\partial A} \right]_{T,V,n}, \quad (1.38)$$

where T is temperature, V is volume, and n is the total number of molecules. Though γ is typically regarded as an energy per unit area, it may also manifest itself as a force per unit length. One example of this is when a moveable wire is placed across a liquid membrane (typically demonstrated using a sliding wire and soap film), the wire will stay at rest at any point along the film. However, upon rupturing the film on one side of the wire, the surface tension of the existing film will pull with a force proportional to γ such that

$$f \cdot dx = 2\gamma l dx, \quad (1.39)$$

where f is the force exerted by the soap film, and l is the length of the rod [106] (See Figure 1.9). Thus, the surface tension may be represented not only as an energy per unit area, but a force per unit length normal to the wire, directing the motion of the wire in toward the film surface, reducing the total surface area of the system.

This effect of surface tension is quite remarkable in flat films, but when you consider curved surfaces it becomes even more interesting. It seems obvious that since surfaces cost energy that nature will tend to minimize surface area between immiscible fluids (ie. two unlike polymers or oil and water) by forming minimal surface structures, like spheres. However, in addition to this drive to minimize surface area,

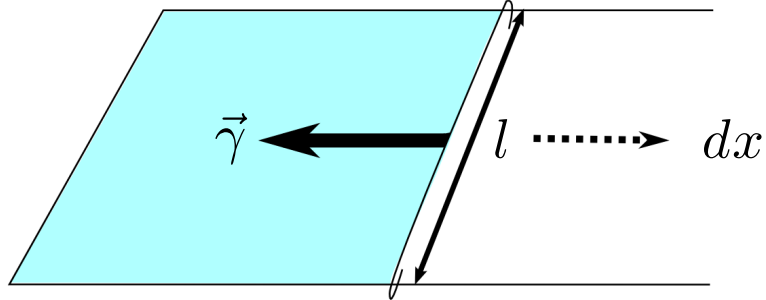


Figure 1.9: Schematic of the simple demonstration of a soap film pulling a mobile wire due to surface tension. The surface tension, $\vec{\gamma}$ acts as a force per unit length, l , pointing inward toward the film surface.

there is also a pressure that must be created to prevent a curved surface from collapsing in on itself. This pressure is calculated for a simple spherical drop of A fluid in a bath of B fluid by computing the work, δW created by deforming the droplet as

$$\delta W = -P_A dV_A - P_B dV_B + \gamma_{AB} dA, \quad (1.40)$$

where P_A and P_B are the pressures in the A and B fluids respectively, γ_{AB} is the interfacial tension between the two fluids, and dV_A , dV_B , and dA are the changes in volume and surface area of the two fluids. Using a spherical geometry and the fact that due to incompressibility, $dV_A = -dV_B$, the condition for mechanical equilibrium, $\delta W = 0$, can be calculated to show a difference in pressures between the A and B liquids to be

$$\Delta P = P_A - P_B = \frac{2\gamma_{AB}}{R}, \quad (1.41)$$

where R is the radius of the spherical droplet. This is quite remarkable, as it tells us that the pressure inside a droplet is greater than outside, simply due to the need to balance surface tension. As a consequence, this signifies greater pressure difference in tiny droplets with smaller radius [106].

This definition of the pressure may be generalized to any liquid-liquid or liquid-

gas interface using Laplace's theorem, where the increase in pressure is calculated as simply the product of surface tension and the curvature of the system, C , such that

$$\Delta P = \gamma \left(\frac{1}{R_1} + \frac{1}{R_2} \right) = \gamma C, \quad (1.42)$$

where R_1 and R_2 are the radii of curvature at the surface. In the case of a sphere, this converges to the pressure calculated in Equation 1.41. However, in the more general case, the two radii of curvature may be identified by considering a more complex surface, like that displayed in Figure 1.10. By defining a direction perpendicular to the surface at any point, the curvature is simply found by taking cuts through two mutually orthogonal planes of the object at that point. The two radii of curvature, R_1 and R_2 , are simply the two radii defined by the curvature at the points intersected by the mutually orthogonal planes. Focusing now on the geometry of a cylindrical liquid jet, like water from your kitchen faucet, we can utilize arguments of minimizing surface energy and Laplace pressures to explain the dynamics within these systems.

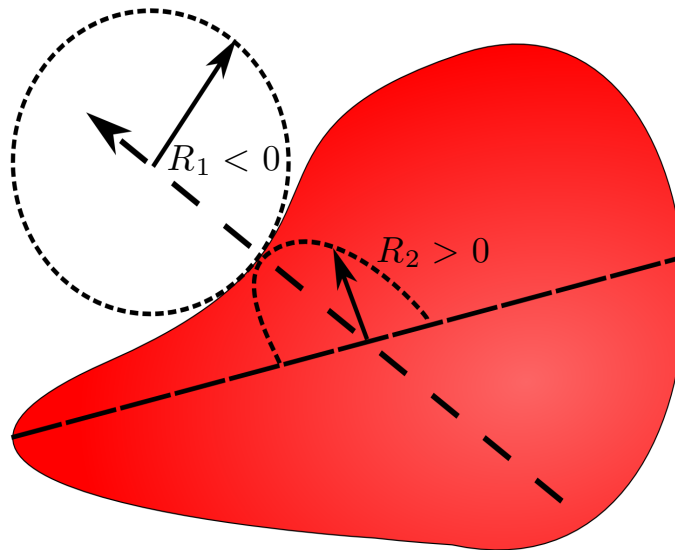


Figure 1.10: Schematic for determining curvature of complex shapes. Radii of curvature may be either positive (R_2) or negative (R_1) dependent on whether their radii are within or without the surface respectively.

As described earlier, the cylindrical jet of water from your faucet breaks up into individual droplets before it hits the sink basin. In order to better understand this, consider a simple analysis of the initial and final states of the system, where initially a perfect cylindrical element exists, and in the final state there is a number of individual spherical droplets, n . Using conservation of volume we obtain

$$\pi R^2 L = n \cdot \frac{4}{3} \pi r^3, \quad (1.43)$$

where L is the length of the cylindrical element being considered, R is the initial radius of the cylinder, and r is the radius of the individual spherical droplets. Since liquid systems prefer to reduce surface area due to their surface tension, consider when $S_f < S_i$, such that

$$n \cdot 4\pi r^2 < 2\pi RL, \quad (1.44)$$

where by combining Equation 1.43 and Equation 1.44 the inequality becomes

$$r > \frac{3}{2}R. \quad (1.45)$$

Therefore, as long as the individual droplets in the final state have radii greater than $\frac{3}{2}R$, the final state has a lower surface energy. However, though this describes the droplet state as equilibrium, it does not explain the dynamics by which this state is achieved. Is the initial state metastable (nucleated dynamics) or unstable (spinodal dynamics)? The response to this question is formed by considering the effect of perturbing the surface and assessing whether the surface energy is reduced or increased, indicating whether the jet is locally stable or unstable. This calculation was initially performed by Lord Rayleigh [108], though a good outline for the calculation may be found in Ref. [14] or [106].

Consider the effect of a sinusoidal perturbation with wavelength, λ and amplitude, ϵ , on a cylinder of radius, R . A schematic of this process is outlined in Figure 1.11, but in mathematical form, the radius of the cylinder along the axis coordinate, x , follows

$$R(x) = R^* + \epsilon \cos(qx), \quad (1.46)$$

where $q = \frac{2\pi}{\lambda}$ is the wave vector of the perturbation, similar to our discussion of

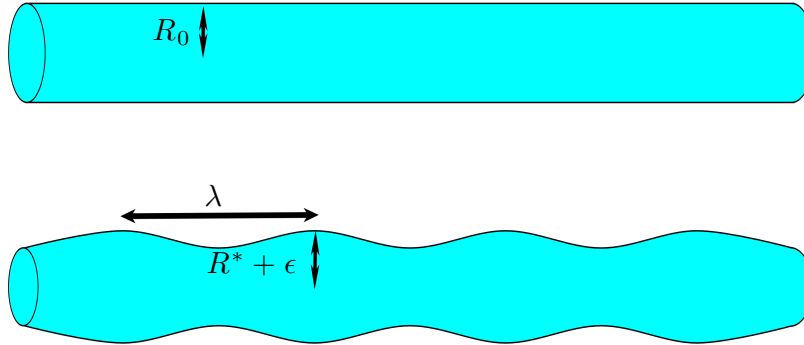


Figure 1.11: Schematic of the Plateau-Rayleigh instability, the unstable perturbation of a liquid jet with amplitude ϵ and wavelength λ .

spinodal decomposition, and R^* is the average radius of the jet which must be less than the initial radius of the jet R in order to conserve volume [106]. By considering small perturbations, where $\epsilon \ll 1$, the surface energy change in the system due to a perturbation, ΔE can be calculated as

$$\Delta E = \frac{\epsilon^2}{4R_0^2} [(qR_0)^2 - 1] E_0, \quad (1.47)$$

where R_0 is the initial cylinder radius, and E_0 is the initial system energy. Note that the value within the brackets will be negative, making the change in energy negative, if

$$\lambda > 2\pi R_0. \quad (1.48)$$

In other words, the cylindrical jet is unstable to any perturbation with wavelength greater than the initial circumference of the jet. Though this tells us that the cylindrical jet is unstable, a similar calculation to that carried out by Cahn and Hilliard for spinodal phase separation may be performed to determine through linear stability analysis that there is a specific wavelength which grows fastest that corresponds to $\lambda_0 = 2\pi\sqrt{2}R_0$ [106,108]. It is interesting to note that though this calculation was first performed by Rayleigh in 1878 describing the stability of liquid jets, it was initially discovered experimentally by Plateau around 1870. He made the discovery when de-

forming droplets of oil in water into long cylinders which he found to break up when cylinders were long enough to satisfy the instability criterion in Equation 1.48 [106]. It is due to the experimental contribution by Plateau and the theoretical contribution by Rayleigh that this instability of liquid jets is commonly referred to as the Plateau-Rayleigh instability [106]. It is interesting to note that the Plateau-Rayleigh instability is a global phenomenon for any fluid-fluid system and plays a role in many practical applications including ink-jet printing and agriculture irrigation, while also being observed throughout nature, such as in the beautiful patterns of droplets formed from the break-up of water films on spider webs [14].

Another cylindrical geometry similar to the liquid jet is that of the liquid bridge (see Figure 1.12). Consider a droplet between two substrates, like some honey between your fingertips. If you separate your fingers only a small amount, a liquid bridge will form, connecting the droplets on each finger (see Figure 1.12a). This bridge can be stable, as the wavelength of perturbation to which the axisymmetric bridge is unstable is longer than the actual length of the bridge [109]. As well, this short liquid bridge applies a capillary force, attempting to force your fingertips back together. This force is induced by the difference between inside and outside curvature of the bridge, such that in Equation 1.42, ΔP is negative at the midpoint of the bridge, pulling the droplets on each fingertip together [106]. Though this conformation of the bridge is stable, if the bridge is stretched further (see Figure 1.12b) by pulling your fingertips apart, it becomes unstable as ΔP becomes positive and liquid flows from the high pressure region at the centre of the bridge (large inside curvature at midpoint), into the low pressure droplets on each finger (small curvature of droplets) [109]. This flow from the centre of the bridge into the droplets causes the bridge to thin out in diameter until it eventually pinches off at the centre point, breaking up into separate droplets on each fingertip.

The breakup of unstable viscous Newtonian liquid bridges has been found to evolve such that the minimum diameter of the bridge, d_{\min} decreases linearly with time, t , such that [110, 111]

$$d_{\min} = d_0 - 2\alpha \frac{\gamma}{\eta} t, \quad (1.49)$$

where d_0 is the initial bridge diameter, $\alpha = 0.0709$ is a numerical pre-factor which has been determined in Ref. [112], and η is the viscosity of the liquid. Equation 1.49 has

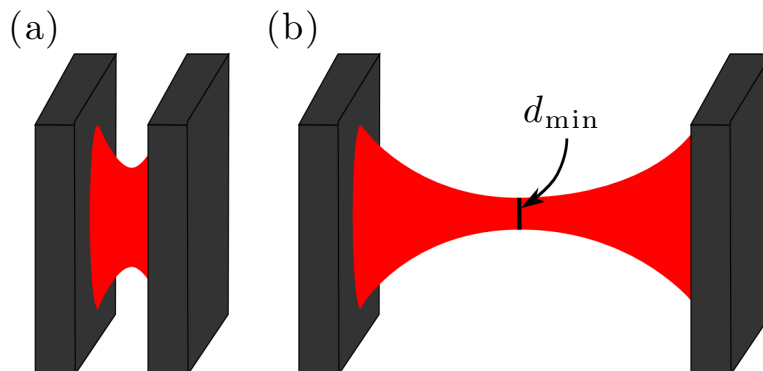


Figure 1.12: Schematic of liquid bridges which are a) stable and b) unstable.

been confirmed to be valid experimentally through a number of rheological experiments on viscous liquids [110,111]. The derivation of Equation 1.49 and the pre-factor α is beyond the scope of this introduction, however it is important to note that it is only valid for break-up dynamics when the outer curvature is much smaller than the inside curvature (ie. $R_{\text{in}} \ll R_{\text{out}}$) at the bridge midpoint. In other words, the bridge must be approximately cylindrical at the midpoint [112], such that the inside or azimuthal curvature related to the bridge radius is much greater than the axial curvature along the outside of the bridge (See Figure 1.12). The remarkable part of Equation 1.49 is that by measuring the minimum diameter of a thinning liquid bridge, we can calculate the ratio of surface tension to viscosity, $\frac{\gamma}{\eta}$, an important rheological property. This ratio of the surface tension to viscosity is sometimes referred to as the capillary velocity [113].

Armed with this understanding of the dynamics in Newtonian liquid jets and bridges, the study of break-up dynamics in polymer liquid jets and bridges has been undertaken. I will now provide an overview of this work, describing the drastic effect that large molecular weight polymers have on the flows within these axisymmetric liquid systems.

1.3.2 Polymer solutions and melts

It has been shown that as liquid jets or bridges of dilute solutions of high molecular weight polymer evolve toward break-up, the local decreases in radius of the jets or bridges are accompanied by a shear thickening that can cause orders of magnitude increases in viscosity [107, 110, 111, 114–118]. This is quite a phenomenal result and may be explained by considering the effect that shear strain rates induced by flow within these axisymmetric geometries have on the long polymer chains.

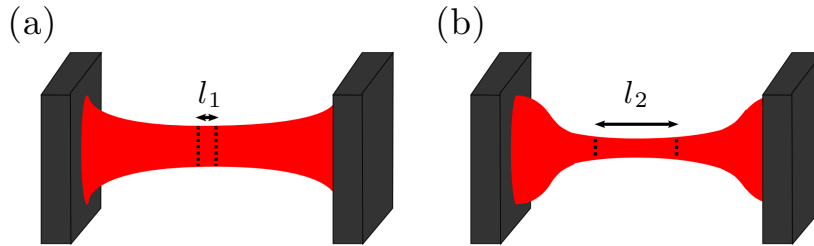


Figure 1.13: Schematic of the elongational shear strain on a cylindrical element at the midpoint of a thinning liquid bridge. l_1 and l_2 represent the length of an equal volume cylinder as material flows from the midpoint of the bridge into the droplets on each substrate.

Considering the evolution of a small cylindrical element at the centre of a liquid bridge (See Figure 1.13), it can be shown that as there is a local decrease in radius, there is also a stretching of the fluid element in that region due to the axisymmetric geometry where material is flowing from the centre of the bridge into droplets on either side. The stretching induces a shear strain rate on polymers within the bridge, and has an intimate relation with the shear thickening effects that are observed. In order to calculate the shear strain rate within the jets and bridges, an assumption must be made similar to Equation 1.49 that the jet or bridge is approximately cylindrical near its pinch-off point. Therefore, the shear strain rate, $\dot{\epsilon}$, is calculated by considering the evolution of a cylindrical element near the pinch off point such that

$$\dot{\epsilon} = \frac{1}{l} \frac{dl}{dt}, \quad (1.50)$$

where l is the length of the fluid element as a function of time as shown in Fig-

ure 1.13. Using conservation of volume in the cylindrical element, then $l = \frac{4V}{\pi d_{\min}^2}$, and Equation 1.50 reduces to

$$\dot{\epsilon} = -\frac{2}{d_{\min}} \frac{d}{dt} (d_{\min}), \quad (1.51)$$

where the shear strain rate, like the capillary velocity from Equation 1.49, can be calculated as a simple function of the measurable parameter, $d_{\min}(t)$ [110, 111].

Combining the knowledge of Equation 1.49 and 1.51, we can see that as a liquid bridge or jet evolves toward pinch-off, and d_{\min} becomes small, the shear strain rates due to the elongation of these cylindrical fluid elements will become very large. In the case of a polymeric liquid, this stretching of the fluid element will extend polymer chains along with it, creating a build up of elastic stresses due to the elastic effects of polymers discussed in Section 1.1. This build up of elastic stresses manifests as a shear thickening, as polymers resist the extensional flow which is extending the chains, slowing down bridge thinning. It has been found that the onset of this shear thickening in the case of dilute polymer solutions is found to occur for shear strain rates which are comparable to the inverse of the polymer relaxation time in dilute solution, $\dot{\epsilon} \gtrsim \frac{1}{\tau_{\text{rel}}}$ [107]. This relation illustrates that for large bridge thicknesses, or low shear strain rates at the bridge midpoint, polymer chains may relax faster than they are extended within the flow, causing the liquid to act Newtonian-like with a viscosity that is similar to that of the solvent, η_s . Conversely, for thin polymer solution bridges, where shear strain rates are high at the midpoint, polymer chains are extended much faster than they can relax, and thus resist this stretching, resisting the flow in thinning regions and increasing the effective viscosity. This increase in effective viscosity is sometimes referred to as the extensional or elongational viscosity [107]. This is remarkable, as it provides a local, shear strain rate dependent viscosity within liquid jets and bridges, which can give rise to a number of very interesting viscoelastic effects in liquid jets [119] and bridges [114–117, 120].

In the case of liquid jets dripping from a nozzle, like water from a faucet, this can give rise to an interesting ‘gobbling’ phenomenon. As droplets break-off from the bottom of a stream, reducing the weight of the liquid element, there is an elastic rebound effect as thin regions of the stream which have a higher effective viscosity, have an elastic response due to the stretching of polymer chains. This results in a thickening of the thin regions, pulling the liquid jet back toward the faucet [119]. As a

consequence, you get an almost bungee jumping like effect, where when droplets at the bottom of the jet detach, the decrease in gravitational force causes an elastic response in the thin capillary regions, pulling the jet upwards. Then, as the amount of liquid in the droplet at the bottom of the jet increases with added fluid, the gravitational force increases, pulling the liquid element down once again. This gravitational force stretches out thin regions within the jet, repeating the process as soon as break-up occurs again. This process is quite beautiful and outlined/imaged nicely in Ref. [119].

However, in the work contained within this thesis I studied the break-up of liquid bridges. Liquid bridges have been the primary focus for research on elongational viscosity increases in high molecular weight polymer solutions and melts [117, 118, 121–125]. As mentioned above, these measurements of viscosity as a function of shear strain rate in dilute polymer solution bridges have demonstrated shear thickening that increases the viscosity by orders of magnitude over that of the solvent. As polymeric bridges thin out under surface tension, instead of a linear decrease in diameter, it has been observed that the diameter decreases at an exponential rate, such that

$$d_{\min}(t) = d_0 \exp(-t/\tau), \quad (1.52)$$

where d_0 is the initial bridge diameter, and τ is the decay constant for the bridge width [115]. In addition to this slowing of dynamics due to shear thickening, in the late stage of break-up, the liquid bridge becomes unstable to a Plateau-Rayleigh instability, causing the liquid bridge to thin out into individual droplets [114–117, 120]. In this process, as fluctuations grow, droplets will grow as expected. However, the thin connections in between the droplets will have drastic increases in effective viscosity due to the pinch-off in these regions. As a consequence, the bridge forms a fairly stable bead-on-a-string (BOAS) structure which consists of low viscosity droplets (beads) connected by thin filaments of high effective viscosity polymer solution (string) [114–117, 120]. A great way to see the BOAS structure described here is to perform an experiment with saliva between your fingers. Due to the mucopolysaccharides in your saliva, this simple accessible solution exhibits all the properties described here, forming a BOAS structure in the late stages which can remain stable for 10's of seconds

In addition to the work on polymer solutions, there has also been an effort to

understand the dynamics of polymer bridges in the melt state as well [121–125]. Similar to in the case of polymer solution bridges, there is shear thickening due to the elastic stresses applied to polymer chains, however most work has looked at high molecular weight polymer melts [121–125], and relatively few have looked at short polymer chains which are below or near to the entanglement molecular weight [122]. As well, diblock copolymer bridges have never been studied until our work presented in Manuscript IV (section 3.4). One can imagine that the additional complexity of diblock copolymer order may play an interesting role in the dynamics of break-up in these liquid bridge geometries.

Chapter 2

Experimental Details

Sample preparation and characterization for all experiments contained within this thesis has been described in detail within the individual Manuscripts in Chapter 3. In this chapter, I will provide a general description of the various techniques for preparation and characterization of polymer films and bridges that were used throughout my PhD research.

2.1 Sample Preparation

2.1.1 Materials

All polymer used in these studies was purchased from Polymer Source Inc. (Dorval, Quebec) and used as received without further purification. All polymer possessed low polydispersity ($M_w/M_n \lesssim 1.10$) and was clean of heterogeneous defects which could alter equilibrium structures or dynamics. The chemical structures of the monomer units for polymers used in experiments contained within this thesis are shown in Figure 2.1.

Symmetric diblock copolymer poly(styrene-*b*-methyl methacrylate) (PS-*b*-PMMA) is a diblock copolymer made up of polystyrene (PS) and poly(methyl methacrylate) (PMMA) linear homopolymer blocks of approximately equal length. PS-*b*-PMMA was chosen due to its low temperature dependence Flory-Huggins interaction parameter of

$$\chi = (0.028 \pm 0.002) + \frac{(3.9 \pm 0.6)}{T}, \quad (2.1)$$

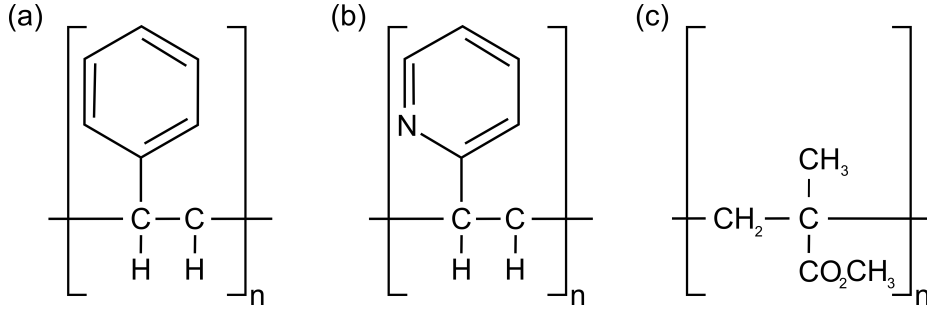


Figure 2.1: Molecular structure of (a) PS, (b) P2VP, and (c) PMMA polymer chains.

as taken from Ref. [126], where T is temperature in degrees Kelvin. By studying polymers of sufficiently large molecular weight, as used in the experiments included in this dissertation ($M_w = 25000 - 26000$ g/mol, $N \approx 500$), both films and bridges can be studied at various temperatures with relatively little change in the diblock copolymer order. For this particular polymer, assuming a bulk ODT occurring at $\chi N \approx 10.5$ as proposed in Ref. [2, 127], the polymer is always highly segregated with $\chi N = 17.8 - 18.6$ for temperatures ranging from 240 °C to 150 °C in the experiments carried out for this dissertation.

In Manuscript IV, poly(styrene-*b*-2-vinylpyridine) (PS-*b*-P2VP) was utilized, with $M_w = 8200 - b - 8300$ g/mol, $N \approx 158$. PS and poly(2-vinylpyridine) (P2VP) are very similar in chemical structure differing by the replacement of one carbon in the benzene ring of PS with a nitrogen atom in the P2VP monomer (See Figure 2.1a and 2.1c). Due to their similarity, they possess almost identical rheological properties (viscosity, η and temperature relations) [128]. Additionally, the order-disorder transition is experimentally accessible with $T_{\text{ODT}} \approx 160$ °C [129], which allows for experimentation in both the ordered and disordered states.

Linear homopolymers were also used for sample preparation in Manuscript III and as a reference system in Manuscript IV. PS homopolymer was used with molecular weight of $M_w = 8, 16, 1140$ kg/mol. The 1140 kg/mol PS was utilized as a smooth substrate for altering the thin film boundary conditions in Manuscript III, while the lower M_w PS was utilized in liquid bridge experiments in Manuscript IV. PS is used as its rheological properties are well understood, allowing for facile interpretation of results in the context of previous work. P2VP homopolymer was also used with M_w

for comparison to PS-b-P2VP dynamics in Manuscript IV.

2.1.2 Film Preparation

The preparation of clean, uniform films is essential for the study of dynamics in diblock copolymer thin films. This is made possible through the process of spin coating, whereby a few droplets of dilute solution of polymer (1.0% to 5% polymer by weight) are placed on a substrate which is then spun at a high rate (1000-5000 rpm) on a commercial spincoater. For all solutions, toluene was used as the solvent. Due to the high volatility of the solvent, after spinning for ≈ 30 seconds, most of the solvent has left the system, and the result is a uniform, thin film of polymer on the substrate. By varying the concentration of solution and rotation speed of the spincoater, I created uniform films with thicknesses ranging from 10's to 100's of nanometres. Increasing the solution concentration increases the resultant film thickness. Conversely, increasing the speed of the spincoater decreases the thickness of the deposited film.

Films are prepared on one of two different substrates: silicon (Si) and mica. Both Si and mica offer a clean, smooth substrate when freshly cleaved. Most films are prepared on Si, as it is highly reflective, making it optimal for optical microscopy and ellipsometry for film characterization. For these experiments, Si wafers with a (1 0 0) orientation and an approximately 2 nm native oxide layer are used. Mica is used primarily as an intermediary in the sample preparation process through the use of a water transfer or "floating" technique that is utilized in the study described in Manuscript III. Once a film is spincast on a mica substrate and annealed to equilibrium configuration, it may be floated onto the surface of an ultra clean water bath of distilled water by submerging the substrate in the liquid. Subsequently, the film may be picked up using a Si substrate, allowing for the creation of layered films.

In order to ensure clean samples, extra care is taken throughout the sample preparation process to remove the possibility of contaminants. Only the highest quality of polymer, Si substrates (University Wafer, USA), mica substrates (Ted Pella Inc., California, USA) and toluene (Optima Grade Toluene, Fisher Scientific Canada) were used to create samples. All solutions were spincast from solution that was filtered through 0.2 μm filters. When cleaving Si substrates, extra care was taken to minimize

the amount of dust contaminant on the substrate surface. As well, mica substrates were only cleaved immediately before spin coating to ensure a pristine surface.

2.1.3 Polymer Melt Bridge Preparation

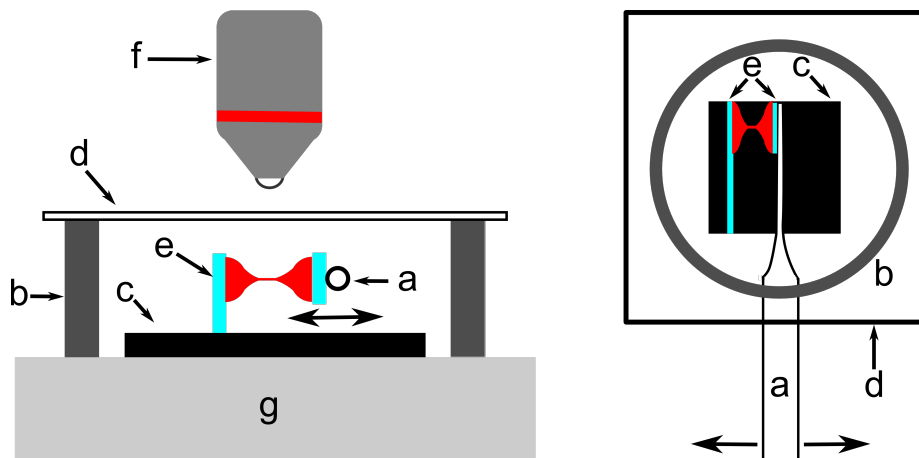


Figure 2.2: Schematic of experimental setup from side view (left) and top view (right). Components of experimental setup are identified in schematic as a) glass micropipette, b) metal ring, c) Si wafer, d) sapphire window, e) glass substrate, f) microscope objective, and g) hot stage. The red droplets represent the polymer.

For our studies on polymer melt bridges I needed to prepare axi-symmetric polymer bridges in the melt state. A detailed description of the experimental process is outlined in Manuscript IV, however I provide a brief description here as well. The experimental setup (shown in Figure 2.2) consisted of one glass substrate being affixed perpendicular to a clean Si wafer while another glass substrate was attached to a stiff glass micropipette that was mounted on a multi-axis translation stage. Polymer was deposited on each glass substrate by placing a droplet of concentrated solution of polymer in toluene ($\approx 25 - 40\%$ polymer by weight) on each glass substrate. The entire setup was placed on a modified optical microscope hot stage (THMS 600, Linkam Scientific, United Kingdom) with temperature control to within 0.1°C . The experimental region of interest is surrounded by a metal ring and topped with a sapphire window (Univeristy Wafer, USA). The metal ring was in conductive contact with both the hot stage and the sapphire window, and due to the high heat conductivity of both the

metal and sapphire, this maintained a consistent and well-known temperature within the experimental cell. The entire setup was placed on an optical microscope stage for observation of liquid bridge dynamics. For experiments performed above 180 °C, I needed an N₂ atmosphere in order to prevent degradation. Since the experimental design was constructed open to the atmosphere, the microscope objective and stage were placed within a sealed plastic bag and flushed with nitrogen during these high temperature experiments. In these experiments, the system was flushed with nitrogen for ≈ 30 minutes before annealing the system to high temperatures.

2.2 Sample Characterization

2.2.1 Optical Microscopy

For most studies within this thesis, an Olympus BX-51 reflection microscope was used to characterize film surfaces and liquid bridge dynamics. Images were taken using a CCD camera mounted on the microscope to provide high resolution images (1390 x 1040 pixels) for subsequent image analysis. All experimental heating on the microscope was performed using a Linkam microscope heating stage to provide precise and accurate temperature control.

2.2.2 Ellipsometry

Film thicknesses and changes in diblock film structure were measured using ellipsometry, a technique which measures the change in light polarization when it is reflected from a film covered substrate. I used both a commercial ellipsometer (EP3, Accurion GmbH, Germany) as well as a custom built device to carry out ellipsometric measurements. A schematic of a general nulling ellipsometry setup is shown in Figure 2.3. A monochromatic red laser is transmitted through a polarizer and quarter wave plate. This combination of optical elements creates elliptically polarized light which depends on the angle of the polarizer, P . In nulling ellipsometry, P is chosen such that upon reflection from the film-substrate sample, the resultant light is linearly polarized. This linearly polarized light is then passed through another polarizer, termed the analyzer, set at an angle A , such that it is cross polarized with the linearly

polarized laser line. This results in creating a minimum resultant intensity, or ‘null’ intensity that is measured using a detector.

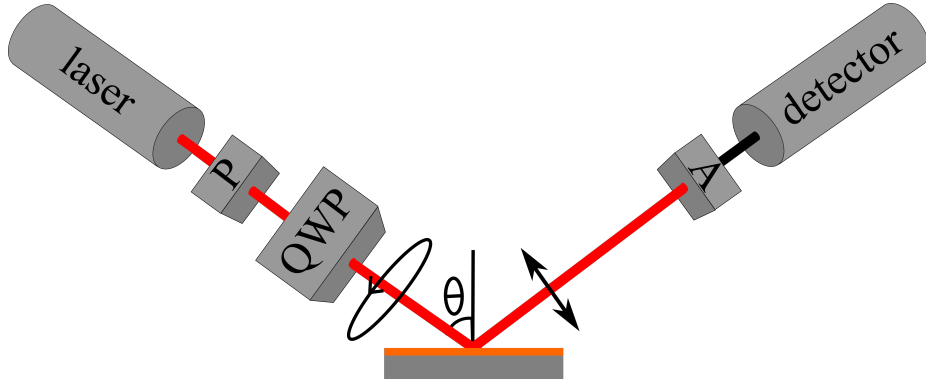


Figure 2.3: Schematic of ellipsometric setup used.

This unique set of polarizer angles, P and A , that results in a null intensity is directly related to films properties such as thickness, h and refractive index, n of the sample when assuming an isotropic film. The power of ellipsometry is its sensitivity to very small changes in thin film properties, measuring film thicknesses on the nanometre scale with the potential for angstrom level accuracy. When the resultant intensity for an initially nulled film with angles P_0 and A_0 are measured as a function of annealing time, information on how films are evolving may be gathered to determine the timescale on which film structure change is occurring.

When recording the polarization angles for an isotropic film, P and A , values of h and n are generally the properties that are measured. Using standard ellipsometry equations, the angles P and A at null may be used to define h and n for the film [130]. Snell’s law states

$$n_1 \sin(\phi_i) = n_2 \sin(\phi_t), \quad (2.2)$$

where n_1 and n_2 are the refractive indices at either side of an interface, and ϕ_i and ϕ_t are the angles between the incident ray and the refracted ray with respect to the normal of the film [130]. The boundary conditions that must be satisfied are determined using Maxwell’s equations, and these boundary conditions determine the perpendicular and parallel components of the lights’ electric field changes upon reflection. A set of equations derived by Fresnel can be used to relate the quantity of light that is

transmitted, t , and reflected, r , at each interface for the different light components which are parallel, \parallel , and perpendicular, \perp where

$$r_{\perp} = \left(\frac{E_{0r}}{E_{0i}} \right)_{\perp} = \frac{n_i \cos(\phi_i) - n_t \cos(\phi_t)}{n_i \cos(\phi_i) + n_t \cos(\phi_t)}, \quad (2.3)$$

$$r_{\parallel} = \left(\frac{E_{0r}}{E_{0i}} \right)_{\parallel} = \frac{n_t \cos(\phi_i) - n_i \cos(\phi_t)}{n_i \cos(\phi_t) + n_t \cos(\phi_i)}, \quad (2.4)$$

$$t_{\perp} = \left(\frac{E_{0t}}{E_{0i}} \right)_{\perp} = \frac{2n_i \cos(\phi_i)}{n_i \cos(\phi_i) + n_t \cos(\phi_t)}, \quad (2.5)$$

$$t_{\parallel} = \left(\frac{E_{0t}}{E_{0i}} \right)_{\parallel} = \frac{2n_i \cos(\phi_i)}{n_i \cos(\phi_t) + n_t \cos(\phi_i)}, \quad (2.6)$$

where E_{0r} , E_{0i} , and E_{0t} are the electric field amplitudes for the reflected, incident and transmitted beams respectively [130]. In addition to the Fresnel equations, describing the transmission and reflection of light at the interfaces, the relative change in phase of each component of light, δ , is dependent on the film thickness and index of refraction according to

$$\delta = 2\pi \left(\frac{t}{\lambda} \right) n \cos(\phi), \quad (2.7)$$

where λ is the wavelength of the laser light [130]. If the experimental setup involves multiple layered films (which is the case for all films on a Si substrate used in this study), then the Fresnel coefficients of Equations 2.3-2.6 must be calculated at each interface. Therefore, a model is constructed using the Fresnel coefficients to match the geometry of the film being studied, accounting for phase changes during transmission and reflection [130]. The model will have fit parameters of the refractive indices and the thicknesses of the different film layers, and will depend on the angle of incidence of the laser light on the film. All except two of the n or t values are fixed within the model, and a minimization scheme is used to adjust these values until the calculated polarizations match those which correspond to the measured polarizer angles P and A . In general, the equation calculated is not invertible and is cyclic, so reasonable values for the refractive index and film thickness must be input in order for the correct film thickness or index of refraction to be fit.

In the experiments carried out in Manuscripts I and II, the ellipsometer was used in

an unconventional way to obtain information on complex structural changes within the film. Since ellipsometry is very sensitive to changes in film structure, I utilize this to monitor the growth of lamellae in symmetric diblock copolymer films as they transition from the spincast, homogeneous state, to the layered lamellar state. In these experiments, homogeneous, disordered films were heated to above the glass transition into the melt state, but below the ODT, so films would order lamellae parallel to the substrate. As soon as the desired film temperature was reached, the polarizer angles, P and A , were set to nulling condition to provide minimum intensity at the detector, and fixed at these angles. As films were annealed and ordered, the change in the structure of the film resulted in an increase in the intensity measured at the detector as new interfaces between lamellar domains were created. Monitoring the evolution of this intensity with time I was able to observe structural changes within the film in the ordering process of parallel lamellae. Due to the complex nature of the growth of lamellae, the precise model of the evolution with time of lamellae was not calculated, however this technique did provide the ability to observe ordering and incubation times in the case of nucleated growth in incommensurate thin films.

2.2.3 Atomic Force Microscopy

An atomic force microscope (AFM) (Caliber, Veeco, USA) was used for sample characterization of diblock copolymer film surface topology and morphology for our work on symmetric diblock copolymer film dynamics. Measurements were made in AFM dynamic contact mode, hereafter referred to as tapping mode, such that the AFM cantilever is driven to oscillate near its resonant frequency. As the AFM tip is brought near to the surface of the film, interactions with the surface via Van der Waals forces, dipole-dipole interactions or electrostatic forces decrease the oscillation amplitude. Using a feedback loop, the tip is kept at a set distance from the surface presenting the same interaction throughout the scan. The advantage of this method, over traditional contact mode, is that you avoid complete contact with the surface which can be destructive as the AFM tip is dragged across the film surface. As well, in regular room conditions without an isolated chamber, a thin water layer is common which can alter the surface forces, making contact mode difficult, favouring the use of tapping mode.

An additional advantage of the tapping mode operation mode is that in addition to film topology information, the changes in oscillation of the tip can be used to provide more information on film properties. As the AFM tip approaches either an island or hole on the film surface, the amplitude of the oscillation will change as the film surface becomes further from the tip (hole) or closer to the tip (island), changing the interaction of the surface with the oscillating tip. Due to the feedback loop, the tip will move to maintain the same oscillation amplitude, however if the amplitude of the oscillation is plotted for the entire scan, the result is a measure of the gradient in the topology, identifying changes in height of the film. Additionally, the tip will have slightly different interactions with materials of different elastic moduli or absorptive properties at the film surface, such as two different polymer blocks [131]. As a consequence, small changes in the phase of oscillation will occur as different materials are at the surface during the scan, resulting in a phase image which provides information on the different blocks at the film surface, thus giving access to the film surface morphologies.

Chapter 3

Summary of Papers

The following 4 papers compose the bulk of the research carried out during my PhD. The first three papers focus on the dynamics of ordering symmetric diblock copolymer thin films. The first two study the nucleated and spinodal formation of terraced structures at the free surface of supported thin films when ordering from the homogeneous, spincast state. The third paper studies the effect on film surface morphology and topology in the order-order transition from asymmetric to symmetric wetting lamellae. The final paper focuses on the dynamics in a different geometry, the liquid bridge, and studies the effect of symmetric diblock copolymer order on the dynamics in polymer melt bridges.

3.1 Manuscript I

Film thickness dependent ordering dynamics of lamellar forming diblock copolymer thin films

R. D. Peters, K. Dalnoki-Veress, Eur. Phys. J. E **35**, 132 (2012).

This study is the first of two studies in which the dynamics of surface decomposition due to incommensurability is studied. For this paper, we spincoat films of poly(styrene-*b*-methyl methacrylate) (PS-PMMA) onto a Si wafer substrate, inducing asymmetric wetting conditions where films require commensurate thicknesses of $\frac{\nu L_0}{2}$ with ν odd. Films were prepared with heights ranging from $\nu \approx 8$ to $\nu \approx 15$ monolayers, resulting in a set of films with widely varying degrees of incommensurability.

Films were studied using the modified ellipsometry technique described in Section 2.2.2, studying the changes in film structure as a function of time while annealing below the ODT in the melt state. In our experiments, we observed three distinct regimes of ordering for our PS-PMMA films: i) an ordering regime where films form an intermediate morphology, ii) an incubation regime where film structure remains unchanged, and iii) a nucleating regime where islands and holes begin to appear at the film surface. This measurement technique gave us access to two timescales within the ordering process, the ordering time taken to form the intermediate structure, τ_{ord} , and the incubation time spent in the intermediate morphology before nucleating islands and holes, τ_{inc} .

τ_{ord} was observed to increase slightly for increasing film thicknesses. This was understood by considering that the more lamellar layers formed during the initial ordering stage, the larger the ordering time, τ_{ord} . Though the effect on τ_{ord} was small, we observed increases in τ_{inc} by 2 orders of magnitude as film thicknesses approached commensurate heights where there was no driving force to nucleate island or holes. We developed a model to describe our data using classical nucleation theory. The free energy was calculated using the strong segregation theory of diblock copolymers assuming an intermediate morphology of parallel compressed or expanded lamellae, like the equilibrium phases of capped symmetric diblock copolymer films.

I was the principal investigator on this study, which involved developing the modified ellipsometry technique, performing experiments and data analysis, developing the model for our data and writing the manuscript. Dr. Kari Dalnoki-Veress contributed through editing the manuscript and discussion on developing the ellipsometry technique, data analysis, and the model.

Film thickness dependent ordering dynamics of lamellar forming diblock copolymer thin films

Robert D. Peters and Kari Dalnoki-Veress^a

Department of Physics & Astronomy and the Brockhouse Institute for Materials Research, McMaster University, Hamilton, Canada

Received 2 August 2012 and Received in final form 19 October 2012
Published online: 19 December 2012 – © EDP Sciences / Società Italiana di Fisica / Springer-Verlag 2012

Abstract. Ellipsometry is used in a novel way to study the ordering dynamics of symmetric poly(styrene-methyl methacrylate) diblock copolymer thin films. Ordered thin films form lamellae parallel to the substrate which can form islands or holes at the free surface to ensure commensurability of the layers. The sensitivity of ellipsometry provides the unique ability to probe morphological changes during the ordering process *before* the ultimate formation of islands or holes at the free surface. We observe three distinct stages in the ordering process: i) an ordering into an intermediate state, ii) an incubation time where the film structure remains constant and iii) the nucleation of islands or holes to achieve equilibrium lamellar morphology. The time-resolved measurement of an incubation period and initial ordering stage provides a means for studying the effect of thickness on the ordering kinetics. The dependence of incubation time on the commensurability of the initial film height is explained using strong segregation theory.

1 Introduction

Diblock copolymers consist of two chemically distinct polymer chains that are covalently bonded together. These molecules are known for their remarkable ability to self-assemble into complex structures when annealed below the order disorder transition (ODT) [1]. Thin films of diblock copolymers are of particular interest due to their promise of technological advancement in photonics [2], data storage [3,4], adhesion [5], and surface property modification [6] among other applications [2].

It has been well established that symmetric diblocks, one of the simplest copolymers consisting of equal parts of both polymer blocks, will microphase separate into a lamellar morphology [1]. In equilibrium, each copolymer bilayer will have a characteristic thickness L_0 , determined by the balance between the enthalpic cost of creating the lamellar interfaces and the entropic cost of chain stretching [1]. In uncapped, supported thin films, we must take into account the effect of additional interfaces resulting from the substrate and free surface. A difference in the interfacial energies of the two polymer blocks with the substrate and the air causes the orientation of lamellae parallel to these interfaces [7]. In asymmetric wetting conditions, interfacial energies are such that one block preferentially orders at the air interface and the other block at the substrate, as is the case for poly(styrene-methyl methacrylate) (PS-PMMA). This results in a total film thickness at equilibrium that is $(N + 1/2)L_0$, with N an integer.

This film height preserves the bilayer thickness L_0 while satisfying the surface preferences for both interfaces [8].

When the initial film height, h_0 , is incommensurate (*i.e.* $h_0 \neq (N + 1/2)L_0$), the free surface will form relief structures of islands or holes upon annealing. These relief structures will grow, conserving volume, until the entire film is composed of two distinct heights, both satisfying the equilibrium condition of $h = (N + 1/2)L_0$ [8]. Though the equilibrium structure of symmetric diblock films is well understood [7,8], how the films order remains an elusive question. A number of studies have examined the growth of islands or holes both experimentally [9–12] and theoretically [9,13] to discern how a symmetric diblock film evolves when annealed below the ODT. Though these studies provide a good picture of how islands and holes form and grow, to the best of our knowledge, time-resolved *in situ* measurements of film ordering *before* the free surface forms relief structures are yet to be presented. Using ellipsometry, a tool that is sensitive to the small changes in structure within the film, we investigate the timescales of evolution from amorphous to lamellar morphologies of symmetric PS-PMMA thin films.

2 Experiment

2.1 Ellipsometry

In previous work, nulling ellipsometry has proven effective for measuring diblock morphological changes [14]. In the form of nulling ellipsometry employed here, circularly polarised monochromatic light is passed through a polarizer

^a e-mail: dalnoki@mcmaster.ca

and quarter wave plate such that when the polarizer is set at angle P , the elliptically polarized light produced after reflection from the film will be linearly polarized. A second polarizer called the analyzer is then rotated to an angle A such that it is cross polarized with the resultant light, yielding a minimum or “null” intensity. In traditional ellipsometry, these polarizer angles P and A are used to calculate film properties such as thickness and index of refraction of a thin film through the standard equations of ellipsometry [15]. Unfortunately, this analysis is model dependent, thus requiring a knowledge of the film structure. Since the evolution of symmetric diblock films from amorphous to lamellar structure is complex and annealing time dependent [16–18], such a direct analysis would be speculative.

To utilize the sensitivity of ellipsometry while simplifying our analysis, we use a modified ellipsometry technique for the bulk of our measurements. The approach we take may not be easily invertible to direct structural information, but as we will see, can be used to obtain the kinetics of changes in the properties of the sample. When the diblock films are annealed, the polarizer angles P and A are fixed to the settings that create a null intensity at the very beginning of the annealing process. Upon annealing, the diblock film will order from the amorphous structure obtained after sample preparation with an average index of refraction and no internal interfaces, to a lamellar morphology with interfaces between layers of PS and PMMA. Since our polarizer angles remain fixed throughout the annealing process, even a small change in the index of refraction profile within the film will alter the reflected polarization of light, causing a change in the measured intensity [14]. Studying the change in the intensity during film evolution, we can measure the timescales associated with the ordering of lamellar forming thin films before the formation of islands or holes occurs at the free surface. The high sensitivity of ellipsometry to changes in the index of refraction profile makes this experimental tool ideal for studying the ordering of the symmetric diblock.

2.2 Sample preparation

PS-PMMA of molecular weight $M_w = 25000\text{--}26000$ g/mol and a polydispersity of 1.06 was used in this study (Polymer Source, Canada). Thin films with thicknesses varying from $h_0 = 105$ to 195 nm were spincoated from dilute toluene solutions (2.5–4.5% by mass) onto silicon with a 1.7 nm native oxide layer. The initial as-cast thicknesses ranged from $h_0 \sim 4.0L_0$ to $7.3L_0$, with $L_0 = 26.5$ nm as measured by AFM for the PS-PMMA molecules used in this study. Samples were then heated in vacuum at 80°C for 2 hours to remove residual solvent and initial film heights were measured using ellipsometry (Accurion Nanofilm EP3, Germany). Samples were annealed during the ellipsometry experiment on a modified microscope heating stage (Linkam THMS 600, United Kingdom). A rapid heating rate of $90^\circ\text{C}/\text{min}$ was used for all measurements.

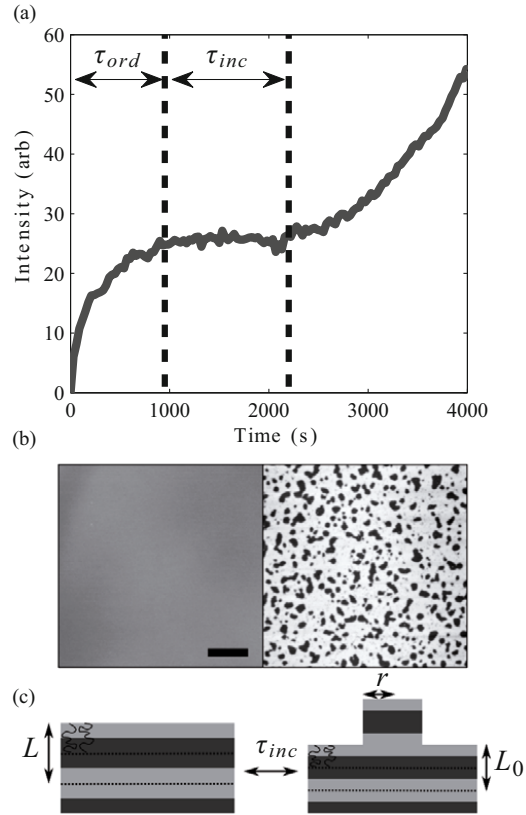


Fig. 1. a) The result of a typical intensity measurement taken for a 137 nm ($5.17L_0$) film with annealing temperature of 160°C . b) AFM topography images of 141 nm ($5.32L_0$) sample taken in the plateau region (left) and after the second intensity increase (right). Scale bar is $10\ \mu\text{m}$. Both images have the same height scale of 28 nm. c) Schematic of transition from metastable lamellar morphology in plateau region to final equilibrium state.

3 Results and discussions

In our experiments, the thin films were rapidly heated above the glass transition and below the ODT. The ellipsometric angles were immediately rotated to achieve a null intensity after the analyzer, and the intensity was monitored using the fixed-angle ellipsometry technique described above. A typical intensity profile, shown in fig. 1a, can be separated into three stages: i) an initial intensity increase, ii) a plateau region, followed by iii) another intensity increase. Using atomic force microscopy (AFM), we have observed that the surface remains flat with peak-to-peak roughness less than 1 nm until the second intensity increase, stage iii). Thus, the second intensity increase is caused by the onset of island or hole formation at the free surface. An example of typical AFM measurements of a

film in the plateau region and after the second intensity increase is provided in fig. 1b. The combination of AFM and the ellipsometry measurements indicate that two distinct processes occur before any changes to the surface topography caused by the final formation of islands or holes. First, an initial ordering of the film, signified by the first intensity increase and the time τ_{ord} . Second, a plateau region indicating that the optical properties within the film remain unchanged (within the resolution of the experiment), represented by the time τ_{inc} . The plateau region is a direct measurement of the incubation period in a metastable state prior to the nucleation event associated with the formation of islands or holes.

The incubation time is not a new concept in the organization of symmetric diblock films [9, 10, 12] and is to be expected if there is a metastable intermediate morphology. The system can be metastable because of an activation barrier associated with the cost of creating excess surface at the edge of islands or holes —directly analogous to the nucleation and growth regime in phase separation. The fixed-angle ellipsometry technique provides the ability to distinguish between the initial ordering stage and the incubation period during film organization with excellent time resolution. This ability to measure the two timescales separately provides the unique opportunity to study the effect of thickness and commensurability on both τ_{ord} and τ_{inc} over a wide range of thicknesses. These timescales and their dependence on initial thickness also provide insight into the intermediate metastable morphology and ordering pathway for symmetric diblock thin films.

In the initial ordering of symmetric diblock thin films, it has been well established that bilayer formation will begin at the interfaces due to strong surface energy differences between the two polymer blocks [16–18]. In the case of PS-PMMA, the surface energy of PMMA at the substrate interface is much lower than that of PS due to hydrogen bonding at the native oxide layer [18, 19]. Conversely, PS has only a slightly lower surface energy than PMMA at the air interface, only differing by $\sim 1\%$ [20]. Thus, as the film begins to order, the difference in surface energy at the substrate will initiate ordering from that interface propagating toward the free surface, forming bilayers of thickness $\sim L_0$ [16, 18]. For incommensurate films, as ordering nears completion there will be either an excess or deficiency of material which prevents lamellae from achieving equilibrium bilayer thicknesses throughout the film. This incommensurability is what will eventually drive nucleation of islands or holes. Using the measurement of the temperature dependence of the PS-PMMA ODT from [21], we calculate the interaction parameter to be $\chi N \sim 27$ for the PS-PMMA in this study when accounting for compositional fluctuations [22]. Thus, the remaining amorphous polymer at the free interface is unstable [23], requiring ordering into an intermediate state. Metastable intermediate states with parallel lamellae of non-equilibrium width have been shown to exist before island or hole nucleation in lamellar-forming diblock films through the use of neutron reflectivity [9]. For a film that is slightly thicker than commensurate, this means that the already formed lamellae must incorporate the excess

amorphous material, deforming into bilayers of thickness $L \geq L_0$. This process will conserve material and lamellar order while forming an intermediate state with a flat film surface. Conversely, if the initial film height is slightly thinner than commensurate, the intermediate state will consist of bilayers of $L \leq L_0$.

While it is not clear how the system adjusts to incorporate amorphous material with non-ideal thickness, we can turn to a simple free-energy calculation to understand the lamellar organization. We calculate the free energy of the film morphology in the strong segregation limit (SSL) [24] for a general film thickness without requiring commensurability (note that the model presented below should be interpreted as a first-order approximation). In the SSL, the lowest free-energy morphology in the intermediate state is that of lamellae with equal bilayer thickness. In this morphology, the excess or deficit of polymer in an incommensurate film is shared between all lamellae, decreasing the total free energy of the film. This morphology of equally deformed lamellae is metastable and consistent with previous measurements of film structure in the intermediate ordered state [9]. In this metastable state, each bilayer will have a thickness of

$$L = \frac{h_0}{(N + \frac{1}{2})}, \quad (1)$$

schematically shown in fig. 1c. Then, for films with $h_0 < (N + 1/2)L_0$, the metastable state would exhibit bilayers that are equally compressed, at a cost of increasing the interaction between the two blocks. In contrast, for films with $h_0 > (N + 1/2)L_0$, the metastable state consists of equally swollen bilayers, with an associated cost of stretching the polymers further than in the equilibrium state. Such swollen or compressed bilayers are equivalent to the equilibrium conformation of films confined between two hard walls which has been studied before [25].

The ordering time τ_{ord} (see fig. 1) represents the time required to form the intermediate state. To study the effect of thickness on τ_{ord} , we measured the initial ordering process at 155°C , where $\tau_{\text{ord}} > 5$ hours for the film heights used in our study. We performed a conventional nulling ellipsometry measurement where we measure the P and A necessary to create a null intensity as two nearly commensurate films of 146 nm ($\sim 5.55L_0$) and 174 nm ($\sim 6.56L_0$) order into the metastable state. Just as in the case of the intensity profile in fixed angle ellipsometry experiments, we do not attempt to model the ellipsometry data. Rather, for determination of the kinetics of ordering it suffices to recognise that if the ellipsometric angles are changing with time, so must the internal structure. $P(t)$ and $A(t)$ change for a time τ_{ord} , and then plateau as the film reaches the metastable state. In fig. 2, we see that the $6.56L_0$ film takes ~ 7 hours to reach the plateau region, whereas the $5.55L_0$ film takes ~ 5 hours. As both films exhibit similar incommensurabilities ($\sim 0.05L_0$ larger than commensurate height), this increase in ordering time for the thicker film can be attributed to the time needed to order an additional bilayer. The fractional change in $A(t)$ for the 174 nm film is a demonstration of the complex ellipsometric response with changing film structure that occurs

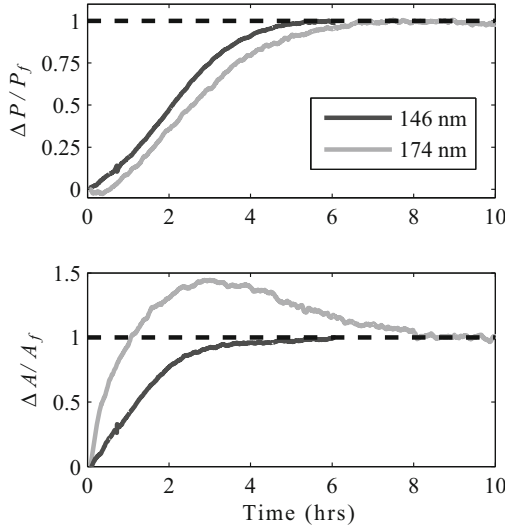


Fig. 2. Nulling ellipsometry measurement of the fractional change in nulling polarizer ($\Delta P/P_f$) and analyzer ($\Delta A/A_f$) angles during the initial ordering stage of 146 nm ($\sim 5.5L_0$) and 174 nm ($\sim 6.5L_0$) films. P_f and A_f represent the nulling polarizer and analyzer angles in the intermediate state.

upon initial ordering. As the formation of bilayers propagates toward the free surface, the response of P and A is not necessarily a monotonic function for all films, however as we are simply identifying the timescale associated with approaching a region of no change, this does not affect our evaluation of the ordering time, τ_{ord} .

For the remaining measurements, samples were annealed at 160 °C and characterized with fixed-angle ellipsometry measurements. At this higher temperature the samples order into the metastable state much faster, with $\tau_{\text{ord}} \sim 20$ minutes. The incubation time τ_{inc} , corresponding to the time the samples remain in the metastable state, was analyzed and defined as the time for which the intensity profile varied by $< 10\%$ from the plateau intensity of the metastable state (See fig. 1a). As an added precaution, during the experiment the samples were also imaged using optical microscopy, ensuring that the end of the incubation of the metastable state coincides with the optically observable nucleation of islands or holes at the film surface.

While the changes in τ_{ord} with h_0 at 160 °C are too small to measure, the measured incubation times, τ_{inc} , of nearly commensurate films increase by over 2 orders of magnitude (see fig. 3). This significant dependence of τ_{inc} on h_0 is to be expected. Consider the case of a commensurate film which can order into lamellae with bilayer thickness L_0 , with no need to swell or compress lamellae. This results in no driving force for nucleation of islands or holes, thus the incubation time diverges. In contrast, for incommensurate films the further the film is from commensurability, the further the bilayers are from equilib-

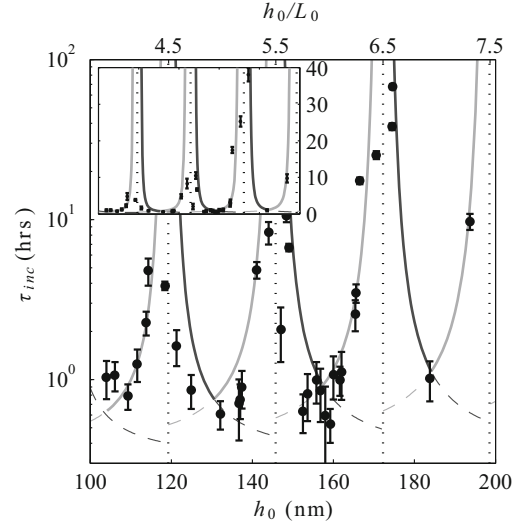


Fig. 3. Incubation time as a function of initial film height on a log-linear scale. The model incubation times for the growth of islands (dark grey) or holes (light grey) are given for each lamellar region. The inset displays the same results on a linear scale. The dotted lines represent commensurate thicknesses of $(N + 1/2)L_0$.

rium in the metastable state. Thus, the driving force to nucleate islands or holes increases and τ_{inc} decreases.

4 Model

A simple model calculated in the SSL can elucidate the dependence of incubation time on h_0 . Let us first consider the case where the film is initially slightly thicker than commensurate. For this case, $L > L_0$ in the metastable state and islands must form to reduce the lamellae to their equilibrium spacing while conserving volume. If we assume a local model, where the formation of an island initially only affects the top bilayer of the metastable film morphology as shown in fig. 1c, then the free-energy change will be a combination of surface energy cost due to the formation of an island edge and a free-energy decrease due to the formation of lamellae with the equilibrium thickness L_0 . The change in free energy may be written as

$$\Delta F = 2\pi r\sigma + V \cdot \Delta G_V(L), \quad (2)$$

where r is the radius of the island grown at the free surface, σ is the line tension of the island edge, V is the local volume of the film participating in the formation of the island, and $\Delta G_V(L)$ is the free-energy change per unit volume for lamellae to go from a lamellar spacing of L to L_0 .

Using conservation of volume between initial and final states, we can define the local volume as $V = \pi r^2 L_0 L / \delta L$,

where $\delta L = L - L_0$. Differentiating the free energy with respect to island radius, finding a critical radius for island formation, and substituting the critical radius back into eq. (2), we obtain an energy barrier for nucleation of

$$\Delta F^* = \frac{-\pi\sigma^2}{\Delta G_V} \cdot \frac{\delta L}{L_0 L}. \quad (3)$$

In the SSL, the difference between the initial and final state entropic and enthalpic contributions is given by [24]

$$\Delta G_V = \left(\frac{\gamma}{L_0} + \alpha L_0^2 \right) - \left(\frac{\gamma}{L} + \alpha L^2 \right), \quad (4)$$

where γ is the interfacial tension at the PS-PMMA interfaces and the constant $\alpha = kT/(N^2 a^5)$, with polymerization index N and monomeric lengthscale a .

At the equilibrium condition $(dG_V/dL)|_{L_0} = 0$, and thus $\gamma = 2\alpha L_0^3$. In combination with eq. (3), this equation yields a free-energy barrier to nucleation of

$$\Delta F^* = \frac{\pi\sigma^2}{3\alpha L_0^2 \delta L + \alpha L_0 (\delta L)^2}. \quad (5)$$

Therefore, the incubation time may be calculated as

$$\tau_{\text{inc}} = \tau_0 \exp\left(\frac{\Delta F^*}{kT}\right) = \tau_0 \exp\left(\frac{\beta}{\delta L + \frac{\delta L^2}{3L_0}}\right), \quad (6)$$

where τ_0 and β are fitting constants with $\beta \equiv \pi\sigma^2/(3kT\alpha L_0^2)$. The constant τ_0 governs the dynamics of the system and corresponds to the case where there is no energy barrier ($\Delta F^* = 0$) and equilibration is limited by molecular mobility. The parameter δL is experimentally determined from the initial film height, h_0 , using eq. (1) and the equilibrium bilayer spacing measured using AFM. Thus, the incubation time for islands may be calculated for each $(N + 1/2)$ number of layers formed in the metastable state. As well, the identical calculation may be performed for hole, rather than island, nucleation with the same result, the only difference being that δL is a negative quantity, causing a sign change in the exponential of eq. (6). Notice that for a commensurate film where $L = L_0$, $\delta L = 0$, and we recover the expected divergence of the incubation time for commensurate films. Conversely, as the film thickness deviates further from commensurability, δL increases causing a greater driving force to nucleation and a resultant decrease in the incubation time as indicated by eq. (6).

In fig. 3 we plot the experimentally determined incubation time as a function of film thickness, as well as the model with $\tau_0 = 1100$ s and $\beta = 0.1L_0$. Clearly the simple nucleation model, calculated in the SSL, effectively describes the data. As the initial film height approaches commensurability, the model diverges and the measured values increase more than 2 orders of magnitude in comparison to τ_{inc} for incommensurate films. There is little variation in τ_{inc} for incommensurate films regardless of the number of bilayers formed in the metastable state. However, the nearly commensurate films show larger increases

in τ_{inc} for thicker films. This difference in commensurability effect on τ_{inc} can be attributed to the fact that bilayers deform less in the metastable state for thicker films, as there are more bilayers to compensate for the incommensurability of the film. Since the bilayers are deformed less, there is a decrease in the driving force to nucleate for thicker films, thus the incubation time is longer. This phenomenon emerges naturally from the model since L , and consequently $\delta L = L - L_0$, is inversely proportional to $(N + 1/2)$ according to eq. (1). This inverse proportionality causes a decrease in maximum δL for thicker films, resulting in an exponential increase in eq. (6). This decrease in driving force causes a narrower region of short incubation times as can be seen in the linear inset of fig. 3. We note that this model assumes a homogeneous sample, ignoring any existence of defects. Additionally, the precise pathway by which islands and holes are nucleated is not taken into consideration for our calculations. Thus, it is expected that some of our measured incubation times will be much shorter than predicted, simply due to defects and ordering pathways of the sample which lower the activation barrier to nucleation. Therefore, the model provides an upper bound on the experimental results.

Though our model provides a good description for nearly commensurate films ($h_0 \sim (N + 1/2)L_0$), as the film heights approach complete incommensurability, the assumptions of the model break down. We assumed that the intermediate state consists of equally deformed lamellae as that is the lowest free-energy morphology consistent with our measurements. However, for incommensurate films, the incubation time becomes much shorter and approaches the timescale of the ordering time. As τ_{inc} gets shorter, the intermediate state will take on a morphology which is not only driven by energetics, but kinetics as well. This intermediate state could then be quite different from the assumption of equally deformed layers, altering the ordering pathway and dynamics for island and hole formation. Nevertheless, the model of the ordering pathway provided here for PS-PMMA thin films provides an acceptable description of the data.

5 Conclusions

In summary, using ellipsometry we were able to measure two distinct timescales in the ordering process of symmetric diblock copolymer films before the ultimate formation of islands or holes at the free surface. At 155 °C we observe an increase in τ_{ord} for thicker films which we attribute to the additional time required to order more bilayers in the metastable state. Annealing at 160 °C, incubation times were found to increase by up to 2 orders of magnitude for nearly commensurate films. As well, thicker films demonstrated a stronger dependence of τ_{inc} on commensurability due to a decrease in driving force from bilayer deformation in the metastable state. The nucleation model, based upon the SSL, captures the physics required to describe the incubation time results while providing insight into the metastable morphology of nearly commensurate symmetric diblock films.

Financial Support for this work was provided by National Sciences and Engineering Research Council (NSERC). The authors thank Mark Matsen for helpful comments.

References

1. G.H. Fredrickson, F.S. Bates, *Annu. Rev. Mater. Sci.* **26**, 501 (1996).
2. I. Hamley, *Progr. Polym. Sci.* **34**, 1161 (2009).
3. T. Thurn-Albrecht, J. Schotter, G.A. Kastle, N. Emley, T. Schibauchi, L. Krusen-Ebaum, K. Guarini, K.T. Black, M.T. Tuominen, T.P. Russell, *Science* **290**, 2126 (2000).
4. C. Tang, E.M. Lennon, G.H. Fredrickson, E.J. Kramer, C.J. Hawker, *Science* **322**, 429 (2008).
5. C. Creton, E.J. Kramer, H.R. Brown, C.Y. Hui, *Adv. Polym. Sci.* **156**, 53 (2001).
6. P. Mansky, Y. Liu, E. Huang, T.P. Russell, C. Hawker, *Science* **275**, 1458 (1997).
7. M.J. Fasolka, A.M. Mayes, *Annu. Rev. Mater. Res.* **31**, 323 (2001).
8. P.F. Green, R. Limary, *Adv. Colloid Interface Sci.* **94**, 53 (2001).
9. S. Joly, D. Ausserre, G. Brotons, Y. Gallot, *Eur. Phys. J. E* **8**, 355 (2002).
10. G. Vignaud, A. Bigaud, G. Grubel, S. Joly, D. Ausserre, J.F. Legrand, Y. Gallot, *Physica B* **248**, 250 (1998).
11. S. Joly, A. Raquois, F. Paris, B. Hamdoun, L. Auvray, D. Ausserre, Y. Gallot, *Phys. Rev. Lett.* **77**, 4394 (1996).
12. B. Collin, D. Chatenay, G. Coulon, D. Ausserre, Y. Gallot, *Macromolecules* **25**, 1621 (1992).
13. K.S. Lyakhova, A. Horvat, A.V. Zvelindovsky, G.J.A. Sevink, *Langmuir* **22**, 5848 (2006).
14. J.L. Carvalho, M.V. Massa, S.L. Cormier, M.W. Matsen, K. Dalnoki-Veress, *Eur. Phys. J. E* **34**, (2011).
15. R.M.A. Azzam, N.M. Bashara, *Ellipsometry and Polarized Light* (North Holland, Amsterdam, 1987).
16. A. Menelle, T.P. Russell, S.H. Anastasiadis, S.K. Satija, C.F. Marjkrzak, *Phys. Rev. Lett.* **68**, 67 (1992).
17. K.R. Shull, *Macromolecules* **25**, 2122 (1992).
18. A.B. Croll, A.C. Shi, K. Dalnoki-Veress, *Phys. Rev. E* **80**, 051803 (2009).
19. M.J. Fasolka, P. Banerjee, A.M. Mayes, G. Pickett, A.C. Balazs, *Macromolecules* **33**, 5702 (2000).
20. S. Wu, *Polymer Interfaces and Adhesion* (Marcel Dekker, New York, 1982).
21. T. Russell, *Macromolecules* **23**, 890 (1990).
22. G.H. Fredrickson, E. Helfand, *J. Chem. Phys.* **87**, 697 (1987).
23. M. Matsen, *J. Chem. Phys.* **106**, 7781 (1997).
24. A. Semenov, *Sov. Phys. JETP* **61**, 733 (1985).
25. T.P. Russell, P. Lambooy, G.J. Kellogg, A.M. Mayes, *Physica B* **213-214**, 22 (1995).

3.2 Manuscript II

Morphology induced spinodal decomposition at the surface of symmetric diblock copolymer films

R. D. Peters, P. Stasiak, M. W. Matsen, K. Dalnoki-Veress, ACS Macro Letters **2**, 441-445 (2013).

This second study on the dynamics of surface feature growth in PS-PMMA films looked at the decomposition of the film surface for maximally incommensurate thin films. Films were first annealed on an ellipsometer for τ_{ord} as described in Manuscript I, then transferred to the AFM. We measured the evolution of the topology at the film surface for successive heating cycles, observing a spinodal decomposition of the film surface with a characteristic length scale of $\approx 2 - 3 \mu\text{m}$. The same spinodal decomposition was observed for films with incommensurate thickness of $\nu = 10, 12$, and 14 monolayers.

At the onset of spinodal decomposition, AFM was used to probe the morphology at the film surface, identifying flat films with perpendicular oriented lamellae at the free interface. These measurements provided evidence of a mixed morphology of parallel lamellae at the substrate surface, and perpendicular lamellae at the free surface. Using SCFT, we determined that the mixed morphology was unstable and was likely the kinetically favoured morphology for a symmetric diblock which will order from the substrate up. We concluded that this mixed morphology was the source of the spinodal decomposition of the film surface, providing a clear picture of the ordering kinetics of symmetric diblock films of maximally incommensurate thicknesses.

I was the principal investigator on this study, which involved performing experiments, analyzing data and writing the manuscript. Dr. Kari Dalnoki-Veress contributed by editing the manuscript and through discussions on experimentation and data analysis and interpretation. Pawel Stasiak performed SCFT calculations. Mark Matsen edited manuscript and provided interpretation of SCFT and experimental results.

Morphology Induced Spinodal Decomposition at the Surface of Symmetric Diblock Copolymer Films

Robert D. Peters,[†] Pawel Stasiak,[‡] Mark W. Matsen,[‡] and Kari Dalnoki-Veress^{*,†,§}

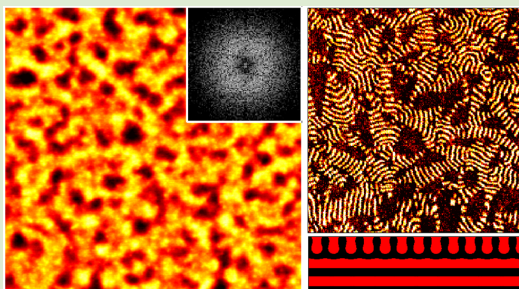
[†]Department of Physics and Astronomy, McMaster University, Hamilton, Ontario, Canada

[‡]School of Mathematical and Physical Sciences, University of Reading, Whiteknights, Reading, United Kingdom

[§]Laboratoire de Physico-Chimie Theorique, UMR CNRS, Gulliver 7083, ESPCI, Paris, France

Supporting Information

ABSTRACT: Atomic force microscopy is used to study the ordering dynamics of symmetric diblock copolymer films. The films order to form a lamellar structure which results in a frustration when the film thickness is incommensurate with the lamellae. By probing the morphology of incommensurate films in the early ordering stages, we discover an intermediate phase of lamellae arranged perpendicular to the film surface. This morphology is accompanied by a continuous growth in amplitude of the film surface topography with a characteristic wavelength, indicative of a spinodal process. Using self-consistent field theory, we show that the observation of perpendicular lamellae suggests an intermediate state with parallel lamellae at the substrate and perpendicular lamellae at the free surface. The calculations confirm that the intermediate state is unstable to thickness fluctuations, thereby driving the spinodal growth of surface structures.



Spinodal processes involve the continuous and rapid growth of two or more distinct phases from an unstable initial state, as opposed to the slower nucleation processes when the initial state is metastable. Spinodal dynamics are known to occur in a wide array of physical systems including alloys,¹ binary fluids,² glasses,³ liquid-crystalline films,⁴ polymer blends,² dewetting polymer films,^{5–9} and even the rupture of foams in a champagne glass.¹⁰ Thin films of symmetric diblock copolymer are of particular interest^{11–13} because they are a simple 2D system where the dynamics of the conserved order parameter $\Psi(x,y) = h(x,y) - h_0$ (film thickness relative to the initial uniform thickness) are potentially slow enough to observe the early time behavior.¹⁴ Maaloum et al. first surmised the existence of a spinodal process in diblock copolymer films from the long-time real-space patterns of $\Psi(x,y)$, which looked as if they emerged from fluctuations of a single characteristic wavelength.¹¹ They therefore assumed that the initial disordered state is unstable with respect to variations in film thickness. Joly et al. provided further evidence for a spinodal process by the absence of an incubation time.¹² However, they proposed a different explanation, which assumes that the free energy of an ordered film, $F(\Psi)$, is a smooth function with an interval of negative curvature (i.e., unstable region) between the two stable film thicknesses. Although these studies have speculated the existence of a spinodal process, conclusive proof and a solid theoretical explanation have yet to be provided. There is no reason for the disordered film to be

unstable, nor is the free energy of ordered films a smooth continuous function of film thickness.

In an “AB” diblock copolymer, incompatibility between the two blocks is characterized by the Flory–Huggins parameter, χ , which varies inversely with temperature. When the blocks segregate, like oil and water, it is the relative size of the A block to the entire polymer chain, f , that determines the morphology. Symmetric diblock copolymers, with equally sized blocks ($f = 1/2$), assemble into a stack of AB/BA bilayers creating a lamellar phase of alternating A- and B-rich domains. In the bulk, this ordered periodic microstructure forms from the disordered melt once $\chi N \gtrsim 10$,^{15,16} where N is the total polymerization index of the copolymers. The preferred thickness of a bilayer, L_0 , is determined by a competition between the entropic cost of stretching polymers and the tension of the A–B interfaces.¹⁷

Though equilibrium morphologies of diblock copolymers in the bulk are well understood,^{15–17} the study of these molecules under confinement is of particular interest owing to their potential for use in a variety of applications and for providing insight into physics at the nanoscale.^{18–22} In the case of thin films supported on a substrate, the copolymer is confined in 1-dimension. The difference in interfacial energies of the A and B block with the substrate and the free (air or vacuum) surface

Received: April 2, 2013

Accepted: April 30, 2013

Published: May 3, 2013

can cause preferential segregation of a particular block at each interface. In the case of symmetric diblocks, these preferred surface interactions direct lamellae to orient parallel to the interfaces.^{23–28} To preserve the equilibrium bilayer thickness throughout the film, the film thickness at equilibrium must satisfy the commensurability condition $h = L_0\nu/2$, where ν is an integer denoting the number of AB monolayers. We denote this parallel phase L_{\parallel}^{ν} . For symmetric wetting conditions where both interfaces have an affinity for the same block, ν is even. Conversely, for asymmetric wetting, ν must be odd. Films with initial thickness, h_0 , which do not satisfy the quantized commensurability condition, will order into regions consisting of ν and $\nu + 2$ monolayers, with a step of thickness L_0 separating the L_{\parallel}^{ν} and $L_{\parallel}^{\nu+2}$ regions. With increasing h_0 , the areal fraction of the $L_{\parallel}^{\nu+2}$ phase expands to satisfy volume conservation. In this case, the relief structures evolve from islands, to a bicontinuous pattern, to holes when the majority of the film is $L_{\parallel}^{\nu+2}$.^{23,24} Though these structures have been well studied, direct measurements of film morphologies during the intermediate stages of annealing in symmetric diblock films remain elusive, yielding a gap in our understanding of the ordering process.

Ordering of these lamellar forming films is known to initiate at the interfaces.^{26,28–30} Once the microphase separation of the diblocks is complete within the film, the topography of the free surface begins to develop relief structures by either nucleation^{13,31–33} or spinodal^{11–13} growth. Though nucleated growth has been shown to arise in nearly commensurate films from a metastable state consisting of parallel lamellae with nonequilibrium bilayer thickness,^{32,33} an explanation for the observation of spinodal decomposition of topological structure far from commensurability is yet to be provided. In order to investigate the origins of the spinodal morphology, we focus here on the pathway as the film transitions from a homogeneous slab to the final ordered phase during sample annealing. We will show that there is an intermediate morphology at the free surface that mediates the transition, and we establish the link between this morphology and the subsequent spinodal decomposition of the topography. Self-consistent field theory (SCFT) calculations verify the differences in the free energy of the observed structures that drive spinodal decomposition.

Experiments were performed using poly(styrene-methyl methacrylate) (PS-PMMA) copolymer, an asymmetrically wetting diblock. The topography evolution of an incommensurate 157 nm ($\nu \approx 12$) film annealed at 155 °C is shown in Figure 1. The upper panels show the spinodal growth of surface

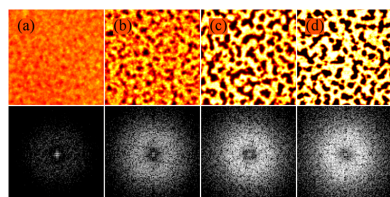


Figure 1. (Top Row) AFM topography images of 157 nm ($\nu \approx 12$) film for annealing times of (a) $t = 175$, (b) $t = 265$, (c) $t = 355$, and (d) $t = 445$ min at 155 °C. Scan size is 25 μm . The vertical scale is the same for each image with black to white corresponding to a 30 nm thickness difference. (Bottom Row) 2DFT obtained from each AFM image.

relief structures typical of all incommensurate films studied, evolving from initial undulations of <3 nm at annealing times of $t = 175$ min to equilibrium fluctuations of 26.5 nm corresponding to the full bilayer thickness at $t = 445$ min. The lower panels plot the 2D Fourier transform (2DFT) computed at each annealing stage. The spinodal ring, which grows in intensity for longer annealing times, is clearly visible. From the radial average of the 2DFT, we obtain a peak frequency of the spinodal pattern at $\sim 0.3 \mu\text{m}^{-1}$, corresponding to a correlation wavelength of $\sim 3 \mu\text{m}$ (Figure 2a). Though we

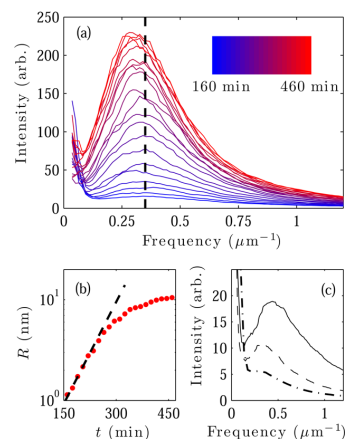


Figure 2. (a) Radial average 2DFT of AFM topography images for increasing annealing times. Dashed line is average peak position at early annealing times. (b) Root-mean-squared roughness, R , as a function of time on a log-linear plot. Straight dashed line shows the exponential growth of the thickness fluctuations at early annealing times. (c) Radial average of the 2DFT for films with initial thickness 129 nm (solid line), 157 nm (dashed line), and 187 nm (dashed-dotted line), corresponding to $\nu \approx 10, 12$, and 14 respectively.

only quantify the early stages of the topography evolution in accordance with the linearized spinodal theory, we do also observe the onset of coarsening through a shift in the 2DFT peak toward shorter frequencies (see Supporting Information).

The root-mean-squared roughness, R , is calculated to characterize the growth of surface fluctuations.^{12,31} In the early stages of spinodal growth, the film exhibits an exponential growth rate in R , consistent with a spinodal process (Figure 2b).² As annealing continues, the roughness plateaus as the equilibrium lamellar thickness is reached. The 2DFT peak amplitude also displays these growth kinetics.³⁴ In addition to the measurements of a film with $\nu \approx 12$, the measurement of early stage spinodal growth was observed for incommensurate films with initial thickness of $h_0 \approx 10L_0/2$ and $h_0 \approx 14L_0/2$. These films vary in thickness by about 60 nm, yet all exhibit similar spinodal wavelengths of 2–3 μm , with a slight increase in wavelength for thicker films (Figure 2c). The similarity in wavelength suggests that the driving force is dependent primarily on the film commensurability and not total film thickness: the wavelength is a property of the diblock structure nearest to the free surface.

As spinodal fluctuations begin to form ($t \sim 160$ min), we probe the morphology at the film surface. An AFM phase image taken during the onset of spinodal growth (Figure 3) clearly shows a majority of lamellae arranged perpendicular to the film

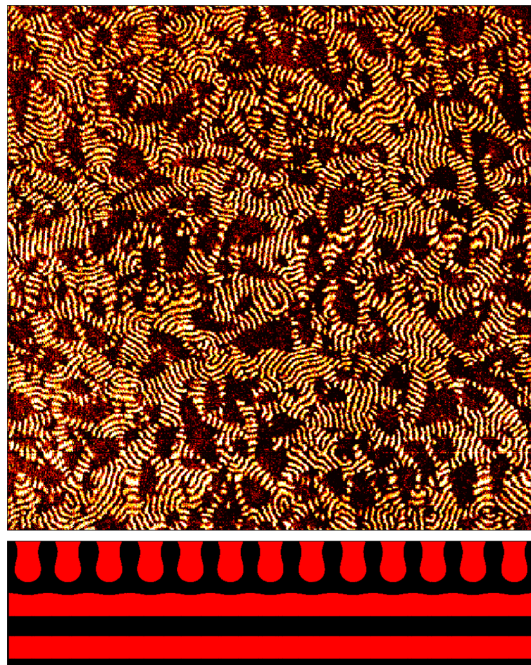


Figure 3. (Top) Phase image ($2.5 \mu\text{m}$) of film surface at $t \sim 160$ min showing majority perpendicular lamellar morphology (PS dark, PMMA light). (Bottom) SCFT calculation of mixed morphology intermediate state.

surface. The perpendicular lamellae of this intermediate morphology have the expected equilibrium bilayer period, L_0 . The larger dark areas in the phase image indicate regions of non-perpendicular morphology caused by the growth of parallel lamellae. This rearrangement is facilitated by the spinodal topography fluctuations at the surface that are already detectable at these annealing times, as demonstrated in Figure 1. Films that are closer to commensurate show nucleated growth of islands or holes, without passing through the intermediate perpendicular lamellar phase of Figure 3.³⁵ Thus, the intermediate morphology that facilitates spinodal decomposition into the L_v^{\parallel} and L_{v+2}^{\parallel} regions is a feature of the frustration in thin maximally incommensurate films.

For all maximally incommensurate films studied, we always observed perpendicular lamellae at the film surface preceding the spinodal growth in the surface topography. As a consequence, our measurements indicate that, for highly incommensurate films, an intermediate ordered state must consist of either (i) perpendicular lamellae throughout the entire film or (ii) a mixed morphology state consisting of perpendicular lamellae at the free surface and parallel lamellae at the substrate, as shown in Figure 3. The PMMA block is known to have a strong preferential interaction with the Si substrate.^{29,35} This surface affinity has been shown to align lamellae parallel to the substrate, well above the ODT,^{29,30} and consequently, a parallel morphology will exist near the substrate upon annealing. Therefore, the perpendicular lamellae at the free surface of incommensurate films indicate that a mixed morphology must occur as an intermediate ordering state. Mixed morphologies have been observed in films with a neutral

substrate³⁶ and in capped films;³⁷ however, the existence of a mixed morphology as an intermediate state in the ordering of films with a free surface is new.

To gain further insight into our system, Figure 4 shows the free energies, F , of different morphologies calculated with

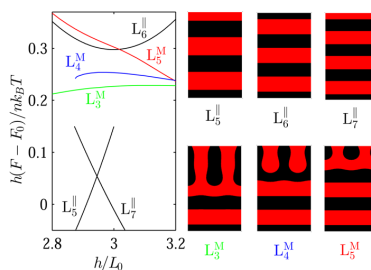


Figure 4. Free energy, F , of parallel (L_v^{\parallel}) and mixed (L_v^M) lamellar morphologies plotted as a function of film thickness, h . F_0 is the free energy of the bulk lamellar phase.

SCFT. Our calculations follow ref 25, except that we use reflecting boundary conditions at the substrate and air surfaces.³⁸ The experimental conditions are approximated by setting the block copolymer parameters to $\chi N = 25$ and $f = 0.5$ and providing an affinity for PS (red) at the air surface of strength $\Delta N = 0.3$, as defined in ref 38. The substrate affinity for PMMA is much greater, which rules out the possibility of perpendicular lamellae according to previous SCFT calculations.³⁸ Therefore, we only consider morphologies where the entire substrate is coated by PMMA (black). We chose a film thickness of $h \approx 6L_0/2$ ($\nu \approx 6$), as thicker films, like those used in our experimental study, will differ only in the number of parallel layers near the substrate. A film thickness corresponding to $\nu \approx 6$ is suited to the L_6^{\parallel} morphology, but nevertheless, the L_5^{\parallel} or L_7^{\parallel} morphologies of either stretched or compressed domains are energetically favorable because they allow for the exposure of PS at the air surface. The mixed (L_v^M) morphologies allow all lamellae to adopt the preferred domain thickness while still allowing a majority of the air surface to be covered by PS. However, there is still some PMMA at the air surface as well as a grain boundary between the parallel and perpendicular lamellae, making mixed morphologies less stable than the L_5^{\parallel} and L_7^{\parallel} morphologies. Notice that the free energies of L_5^{\parallel} and L_7^{\parallel} do not form a single smooth curve as originally assumed by Joly et al.¹²

Although the SCFT tells us which morphologies are favored at equilibrium, one has to consider the kinetics involved in forming the domains. The substrate has a far stronger affinity for PMMA than the air surface does for PS,²⁹ thus, the ordering will begin at the substrate with parallel lamellae of the preferred thickness. As the disordered region near the air interface gets thinner, the incommensurability of the film will become apparent. If the system continues to form parallel monolayers of equilibrium thickness, the system will end up in the costly L_6^{\parallel} morphology, with PMMA at the free interface. However, in order to form the more favorable L_5^{\parallel} or L_7^{\parallel} morphologies, the system must adjust the thickness of the existing lamellae near the substrate, which is a slow process due to the necessity of polymer exchange between layers.³⁹ The alternative is for the remaining disordered region to form perpendicular lamellae, resulting in the mixed morphology L_4^M structure. The L_5^M

morphology is unfavorable because of the high free energy associated with the excess bending of the lamellar domains. Despite the lower free energy of the L_3^M morphology, we expect this to be bypassed because of the rapid formation of parallel lamellae; it is only when there is a disordered layer of thickness $\sim L_0$ that the frustration of incommensurability is apparent to the system.

With the system in the intermediate morphology, L_4^M , the subsequent evolution of the system is then intimately related to the curvature of the free energy. The negative curvature of the L_4^M morphology implies that it is unstable with respect to small variations in film thickness.²⁵ Consequently, any flow of material from one area of the film to another will lower the overall free energy of the system; this instability is the key ingredient for spinodal fluctuations to occur.

Direct measurement of an unstable intermediate mixed morphology for highly incommensurate films completes the picture of symmetric diblock copolymer film ordering. As has already been well established, surface relief structures grow via a nucleated process for nearly commensurate films due to a metastable intermediate state of deformed parallel lamellae.^{32,33} Conversely, the maximally incommensurate films will exhibit spinodal growth patterns induced by a kinetically favored unstable intermediate state of mixed lamellar orientations. Additionally, in the regime of moderate incommensurability we might expect that nucleated and spinodal growth kinetics could occur simultaneously, as is indeed observed in experiment (see Supporting Information).

In conclusion, we have characterized the ordering process of PS-PMMA symmetric copolymer thin films. Identifying a direct link between our observations of an intermediate film morphology and surface relief growth kinetics, we have determined the source of spinodal decomposition in the film topography. The ordering pathway consists of an intermediate state of mixed lamellar morphology which precedes topological fluctuations. The free energy of the mixed morphology is calculated using SCFT, and is found to be an unstable state. In particular, it has a negative curvature in the free energy as a function of film thickness, providing the driving force necessary for the spinodal decomposition of the surface fluctuations. These results provide a clear picture of the ordering pathway of symmetric diblock films through an intermediate mixed morphology that is unstable to spinodal thickness variations.

EXPERIMENTAL SECTION

PS-PMMA copolymer of molecular weight for the blocks $M_w(\text{PS}) \approx 25$ kg/mol, $M_w(\text{PMMA}) \approx 26$ kg/mol, and dispersity = 1.06 (Polymer Source, Canada) was used. The equilibrium bilayer thickness was determined to be $L_0 = 26.5$ nm using atomic force microscopy (AFM; Veeco Caliber, U.S.A.). Samples were spincoated in air from dilute toluene solutions onto Si substrates with the native oxide layer present, such that they were *maximally incommensurate*, that is, $h_0 \approx L_0\nu/2$ with ν even, because PS-PMMA is asymmetrically wetting. The initial as-cast films exhibit thickness variations of less than 1 nm as measured using ellipsometry and have no long-range order due to rapid solvent evaporation during spincoating. These films were subsequently annealed at 155 °C, well below the order-disorder transition temperature (ODT), causing the film to order into lamellae. The samples were monitored during annealing using an ellipsometry technique sensitive to changes in film morphology,³³ and quenched into the glassy state as soon as surface topography began to change. Using AFM in tapping mode, the film surface was studied both with topography and phase imaging. The phase signal is sensitive to the mechanical contrast between PS and PMMA domains at the surface.⁴⁰ We continue to anneal films at 155 °C, interrupted by rapid quenches

into the glassy state to observe the evolution of the film surface with AFM.

ASSOCIATED CONTENT

Supporting Information

- (i) Analysis of 2DFT peak amplitude and position revealing the onset of coarsening of the surface topography at large times.
- (ii) Topography evolution of films with moderate incommensurability demonstrating both metastable and spinodal processes. This material is available free of charge via the Internet at <http://pubs.acs.org>.

AUTHOR INFORMATION

Corresponding Author

*E-mail: dalnoki@mcmaster.ca.

Notes

The authors declare no competing financial interest.

ACKNOWLEDGMENTS

Financial Support for this work was provided by NSERC (Canada) and EPSRC (U.K.).

REFERENCES

- (1) Gerold, V.; Kosterz, G. *J. Appl. Crystallogr.* **1978**, *11*, 376–404.
- (2) Gunton, J. D.; San Miguel, M.; Sahni, P. S. The Dynamics of First Order Phase Transitions. In *Phase Transitions and Critical Phenomena*; Domb, C., Lebowitz, J. L., Eds.; Academic Press: London, 1983; Vol. 8.
- (3) Jantzen, C. M. F.; Herman, H. . In *Phase Diagrams: Material Science and Technology*; Alpter, A. A., Ed.; Academic Press: New York, 1978; Vol. 5.
- (4) Vandenbrouck, F.; Valignat, M. P.; Cazabat, A. M. *Phys. Rev. Lett.* **1999**, *82*, 2693–2696.
- (5) Redon, C.; Brochard-Wyart, F.; Rondelez, F. *Phys. Rev. Lett.* **1991**, *66*, 715–718.
- (6) Reiter, G. *Phys. Rev. Lett.* **1992**, *68*, 75–78.
- (7) Sferrazza, M.; Heppenstall-Butler, M.; Cubitt, R.; Bucknall, D.; Webster, J.; Jones, R. A. L. *Phys. Rev. Lett.* **1998**, *81*, 5173–5176.
- (8) Higgins, A. M.; Jones, R. A. L. *Nature* **2000**, *404*, 476–478.
- (9) Seemann, R.; Herminghaus, S.; Jacobs, K. *Phys. Rev. Lett.* **2000**, *86*, 5534–5537.
- (10) Bergeron, V. *J. Phys.: Condens. Matter* **1999**, *11*, R215–R238.
- (11) Maaloum, M.; Ausserre, D.; Chatenay, D.; Gallot, Y. *Phys. Rev. Lett.* **1993**, *70*, 2577–2580.
- (12) Joly, S.; Raquois, A.; Paris, F.; Hamdoun, B.; Auvray, L.; Ausserre, D.; Gallot, Y. *Phys. Rev. Lett.* **1996**, *77*, 4394–4397.
- (13) Vignaud, G.; Bigaud, A.; Grubel, G.; Joly, S.; Ausserre, D.; Legrand, J. F.; Gallot, Y. *Physica B* **1998**, *248*, 250–257.
- (14) This representation of the order parameter, Ψ , as a height difference is analogous to the use of a compositional order parameter for a two-component blend. The two components of the system are effectively the heights of (i) an island and (ii) a hole; film heights between these two extremes may be regarded as a mixture of the two components.
- (15) Bates, F. S. *Science* **1991**, *251*, 898–905.
- (16) Bates, F. S.; Fredrickson, G. H. *Annu. Rev. Phys. Chem.* **1990**, *41*, 525–557.
- (17) Matsen, M. W. *J. Phys.: Condens. Matter* **2002**, *14*, R21–R47.
- (18) Hamley, I. *Prog. Polym. Sci.* **2009**, *34*, 1161–1210.
- (19) Thurn-Albrecht, T.; Schotter, J.; Kastle, G. A.; Emley, N.; Schibauchi, T.; Krusen-Ebaum, L.; Guarini, K.; Black, K. T.; Tuominen, M. T.; Russell, T. P. *Science* **2000**, *290*, 2126–2129.
- (20) Tang, C.; Lennon, E. M.; Fredrickson, G. H.; Kramer, E. J.; Hawker, C. J. *Science* **2008**, *322*, 429–432.
- (21) Creton, C.; Kramer, E. J.; Brown, H. R.; Hui, C. Y. *Adv. Polym. Sci.* **2001**, *156*, 53–136.

ACS Macro Letters

Letter

- (22) Mansky, P.; Liu, Y.; Huang, E.; Russell, T. P.; Hawker, C. *Science* **1997**, *275*, 1458–1460.
- (23) Green, P. F.; Limary, R. *Adv. Colloid Interface Sci.* **2001**, *94*, 53–81.
- (24) Fasolka, M. J.; Mayes, A. M. *Annu. Rev. Mater. Res.* **2001**, *31*, 323–355.
- (25) Matsen, M. J. *Chem. Phys.* **1997**, *106*, 7781–7791.
- (26) Shull, K. R. *Macromolecules* **1992**, *25*, 2122–2133.
- (27) Croll, A. B.; Massa, M. V.; Matsen, M. W.; Dalnoki-Veress, K. *Phys. Rev. Lett.* **2006**, *97*, 204502.
- (28) Croll, A. B.; Shi, A.-C.; Dalnoki-Veress, K. *Phys. Rev. E* **2009**, *80*, 051803.
- (29) Anastasiadis, S. H.; Russell, T. P.; Satija, S. K.; Majkrzak, C. F. *Phys. Rev. Lett.* **1989**, *62*, 1852–1855.
- (30) Menelle, A.; Russell, T. P.; Anastasiadis, S. H.; Satija, S. K.; Majkrzak, C. F. *Phys. Rev. Lett.* **1992**, *68*, 67–70.
- (31) Collin, B.; Chatenay, D.; Coulon, G.; Ausserre, D.; Gallot, Y. *Macromolecules* **1992**, *25*, 1621–1622.
- (32) Joly, S.; Ausserre, D.; Brotons, G.; Gallot, Y. *Eur. Phys. J. E* **2002**, *8*, 355–363.
- (33) Peters, R. D.; Dalnoki-Veress, K. *Eur. Phys. J. E* **2012**, *35*, 132.
- (34) The peak amplitude in the 2DFT radial average displays the same physical characteristics as the RMS roughness (see Supporting Information). However, due to the complex 2DFT background of the AFM tip and variations between measurements, we find roughness to be a more robust measure.
- (35) Fasolka, M. J.; Banerjee, P.; Mayes, A. M.; Pickett, G.; Balazs, A. C. *Macromolecules* **2000**, *33*, 5702–5712.
- (36) Mansky, P.; Russell, T. P.; Hasker, C. J.; Pitsikalis, M.; Mays, J. *Macromolecules* **1997**, *30*, 6810–6813.
- (37) Koneripalli, N.; Levicky, R.; Bates, F. S. *Langmuir* **1996**, *12*, 6681–6690.
- (38) Matsen, M. W. *Macromolecules* **2006**, *39*, 5512–5520.
- (39) Croll, A. B.; Matsen, M. W.; Shi, A.-C.; Dalnoki-Veress, K. *Eur. Phys. J. E* **2008**, *27*, 407–411.
- (40) Vu, T.; Mahadevapuram, N.; Perera, G. M.; Stein, G. E. *Macromolecules* **2011**, *44*, 6121–6127.

3.3 Manuscript III

An intermediate perforated lamella morphology mediates an order-order transition in thin symmetric diblock copolymer films

R. D. Peters, K. Dalnoki-Veress, (Submitted to Journal of Polymer Science Part B: Polymer Physics)

This third study on thin films of symmetric diblock copolymers observed the order-order transition between asymmetrically wetting lamellae to symmetrically wetting lamellae. Thin films of symmetric diblock PS-PMMA were prepared on mica substrates and annealed to order lamellae parallel to the substrate with PMMA segregated to the mica substrate and PS at the free surface. Asymmetrically commensurate films were used (ν odd) such that at equilibrium, the film surface was flat and featureless. Films were then transferred via the floating technique to substrates which favoured the PS block, changing the boundary conditions from asymmetric to symmetric wetting (ν even). Films were transferred such that the PMMA interface was exposed at the free interface, producing maximally incommensurate films, with surface energy boundary conditions not satisfied at the free surface.

The films were subsequently annealed and observed using AFM to study both the topology and morphology at the free surface. Initially, film surface topology remained unchanged while the lamella at the free surface developed interfacial curvature to produce a perforated lamella (PL) morphology. This PL morphology, though inducing curvature for a lamellar forming polymer, exposes the lower interfacial energy PS at the surface, providing a method for free energy decrease before forming islands or holes. After subsequent annealing, the growth of islands and holes is observed from the PL morphology. The holes were shown to grow with an anisotropic and ramified growth, indicating a preference for higher curvature holes when growing from the perforated lamella morphology.

As the principal investigator, I developed the sample preparation technique and performed measurements, analyzed data and prepared the manuscript. Dr. Kari Dalnoki-Veress contributed with discussions on measurements, data analysis and editing of the manuscript.

An intermediate perforated lamella morphology mediates an order-order transition in thin symmetric diblock copolymer films

Robert D. Peters¹ and Kari Dalnoki-Veress^{1,2}

Atomic force microscopy is used to study the order-order transition of lamellae forming symmetric poly(styrene-*b*-methyl methacrylate) diblock copolymer thin films with a step change in the surface interactions. Commensurate asymmetrically wetting lamellar films are prepared and equilibrated before being transferred to a new substrate that imposes sudden symmetric wetting conditions. The change in boundary conditions creates frustration in the film at the free surface. This frustration leads to the formation of an intermediate morphology upon annealing of a perforated lamella at the free interface. Upon further annealing, we observe separation of the film surface into regions of commensurate thickness with hole growth that is highly anisotropic in shape.

Keywords: block copolymers, order-order transitions, perforated lamella, thin films.

1 Introduction

Self-assembled periodic microstructures are prevalent in a wide variety of physical systems including liquid crystals^{1,2}, lipid membranes/vesicles^{3,4}, and block copolymer melts⁵. The equilibrium morphologies exhibited in these systems, in particular in block copolymer melts, are well understood and have received a great deal of interest due to the possibility for applications in nanolithography⁶⁻⁹, data storage^{10,11}, biomolecule patterning¹², and more^{5,13,14}. One subset of this broad class of self-assembling molecules is the simple “AB” diblock copolymer, a linear polymer consisting of two separate polymer blocks, “A” and “B”, covalently bonded together. Due to the chemical differences between the two blocks, phase separation is preferred at sufficiently low temperatures, below the order-disorder transition temperature, T_{ODT} . However, since the two polymer blocks are bonded together, macrophase separation is impossible causing phase separation to be restricted to the molecular scale (~ 10 nm). The ratio of lengths of the two blocks determines the resultant morphology of the ordered structure at equilibrium^{5,13}. In the case of symmetric diblock copolymers, composed of two polymer blocks of similar length, the melt orders into AB/BA bilayers with characteristic thickness, L_0 , when annealed below T_{ODT} ¹⁵. As the asymmetry of the block lengths is increased, a spontaneous interfacial curvature gives rise to equilibrium states which adopt cylindrical then spherical domain morphologies, or under certain conditions more complex morphologies such as the gyroid morphology^{5,16}.

In the case of supported diblock thin films, the additional interfaces at the substrate and free surface play a role in determining the equilibrium morphology^{13,17-19}. A difference in

interfacial energies of the two blocks at each surface induces an ordering of lamellae parallel to these boundaries¹³. Due to this orientation of lamellae, at equilibrium the film thickness, h , must satisfy the commensurability condition

$$h = \frac{\nu L_0}{2}, \quad (1)$$

where ν is a positive integer representing the number of monolayers in the system^{13,15,20}. Under asymmetric wetting conditions, where interfacial energies are such that one block preferentially orders at the substrate and the other block orders at the free surface, ν is odd. Conversely, when the same block is energetically preferable at both interfaces, ν is even. This ensures that the equilibrium bilayer width, L_0 , is preserved while satisfying surface energy conditions and volume conservation. For films with initial thickness that do not satisfy Equation 1, the film separates into regions consisting of ν and $\nu + 2$ monolayers, forming a terraced structure of islands or holes at the free interface, separated in thickness by L_0 ^{15,21-25}.

The equilibrium structures formed by diblock copolymers are well understood in thin films and the bulk. However, the kinetics of ordering is of great interest for understanding properties of ordered copolymers and optimizing processing²⁶. The transition pathway for the disorder-order transition of symmetric diblock copolymer films has been studied thoroughly^{21-24,27-30}. However, there is still much to be learnt through research of order-order transitions (OOTs) in thin film copolymer systems. The kinetics of OOTs have been studied using experiment^{19,31-38}, theory³⁹⁻⁴¹, and simulation^{35,36,42,43} to understand the transition between different morphologies. Most of this work has focused on understanding the epitaxial growth of one morphology from another morphology with different interfacial curvature of the micro-domains. However, significantly less work has been done on the transition between two similar morphologies.

¹ Department of Physics & Astronomy and the Brockhouse Institute for Materials Research, McMaster University, Hamilton, ON, Canada; E-mail: dalnoki@mcmaster.ca

² Laboratoire de Physico-Chimie Théorique, UMR CNRS 7083 Gulliver, ESPCI ParisTech, PSL Research University

Koneripalli et al. have studied the lamellar to lamellar transition in thin films, where capped films (films sandwiched between two hard interfaces) were annealed to produce parallel oriented lamellae with non-equilibrium bilayer thickness, $L < L_0$. These non-equilibrium films were subsequently uncapped to produce a free interface and annealed to monitor the growth of holes at the free surface³³. In this system, there is a high degree of strain on the films due to the non-equilibrium lamellae in comparison to their bulk ordered conformations. In our work we also study the transition between two morphologies of parallel oriented lamellae in thin films, however films are prepared such that they possess equilibrium bilayer thickness both before and at long times after the transition. We perform this experiment by switching the boundary conditions from asymmetric (ν odd) to symmetric wetting (ν even), observing the transition between a commensurate asymmetrically wetting film to a completely incommensurate symmetrically wetting film. Upon annealing, we monitor the free surface for the evolution of both the morphology and topography.

2 Experiment

Thin films of symmetric diblock poly(styrene-*b*-methyl methacrylate) (PS-PMMA) ($M_w = 25000 - 26000$ g/mol, polydispersity index = 1.06) (Polymer Source, Canada) were spincoated from toluene solution (2.0% – 4.0% polymer by weight) onto freshly cleaved mica sheets (Ted Pella Inc., USA). The equilibrium bilayer thickness for this copolymer was measured to be $L_0 \approx 26.5$ nm using atomic force microscopy (AFM) (Veeco Caliber, USA). Films were annealed at 180 °C for 24 hours under vacuum to obtain equilibrium commensurate lamellar films on mica*. The PS block has a lower surface energy at the air interface⁴⁴ and PMMA is preferred at the mica substrate⁴⁵, yielding an equilibrium condition of asymmetrically wetting lamellae with film thicknesses that correspond to ν odd (see Equation 1). In this study, we look at diblock film thicknesses which are commensurate under these asymmetric wetting conditions ($h_0 \approx 200$ nm $\approx 7.5L_0$), providing a smooth, featureless topography at equilibrium. Initial film thicknesses were measured using ellipsometry (EP3, Accurion GmbH, Germany).

A substrate favourable to the PS block is prepared by spin coating high molecular weight PS ($M_w = 1140$ kg/mol) (Polymer Source, Canada) from a dilute toluene solution (0.5% polymer by weight) onto freshly cleaved Si wafers. All PS films are annealed for 24 hrs at 180 °C under vacuum to remove solvent and produce uniform films with a film thickness $h \approx 50$ nm. Due to the much higher molecular weight of the PS ($M_w = 1140$ kg/mol) in comparison to that of the PS-PMMA ($M_w = 51$ kg/mol), the dynamics of the PS film will be sig-

*We note that adjusting the film thickness to obtain commensurate films requires careful adjustment of the thickness and some trial-and-error.

nificantly slower, allowing us to focus on the kinetics of the copolymer films. From hereafter, these high molecular weight PS films will be referred to as PS substrates.

After annealing at 180 °C for 24 hrs, both the PS-PMMA films on mica and PS substrates are quenched to room temperature where they are in the glassy state. The PS-PMMA films on mica are then submerged in a beaker of ultra pure water (18 M Ω cm, Pall Cascada, LS) to transfer the PS-PMMA onto the water surface. The film is then removed from the water surface using the PS substrate. This new substrate changes the wetting conditions from asymmetric to symmetric since the PS block is now preferred at both the substrate and free air interface. The change in wetting conditions means the *films that were previously prepared to be commensurate under asymmetric wetting conditions are now maximally frustrated*, and must separate into regions which satisfy the new commensurability condition (ν even in Equation 1) while conserving volume.

After the diblock films are transferred from the water surface to the PS substrate, the residual water is allowed to fully evaporate before annealing. These frustrated diblock copolymer films are subsequently annealed on a heating stage for specific intervals (Linkam Scientific, UK), quenched to room temperature, and imaged with AFM. The AFM was used in tapping mode, providing data for both film topology and the phase shift in AFM tip oscillation. The phase shift of the AFM tip oscillation is sensitive to the contrast in mechanical properties of the two block domains at the free interface⁴⁶, providing information on self assembled morphology at the free surface. Though surface defects such as wrinkles in the film or contaminants are unavoidable, great care was taken to image only areas which were defect free.

3 Results and Discussion

An interesting aspect of the sample preparation is that the asymmetrically ordered films may be oriented in one of two ways on the PS substrate. If the diblock film is removed from the water surface from underneath, this leaves the PS block exposed at the free surface (favourable) and the PMMA block in contact with the PS substrate (unfavourable). Alternatively, the PS-PMMA film may be oriented such that the PMMA block is exposed at the free surface (unfavourable), and the PS block is segregated to the PS substrate (favourable). In both orientations, the PMMA interface of the diblock copolymer film does not satisfy the new symmetric wetting conditions, and the film must rearrange to satisfy the commensurability condition such that ν is even.

In this manuscript we focus on the latter case, exposing PMMA at the free interface. This orientation allows us to concentrate the frustration in film morphology at the free surface

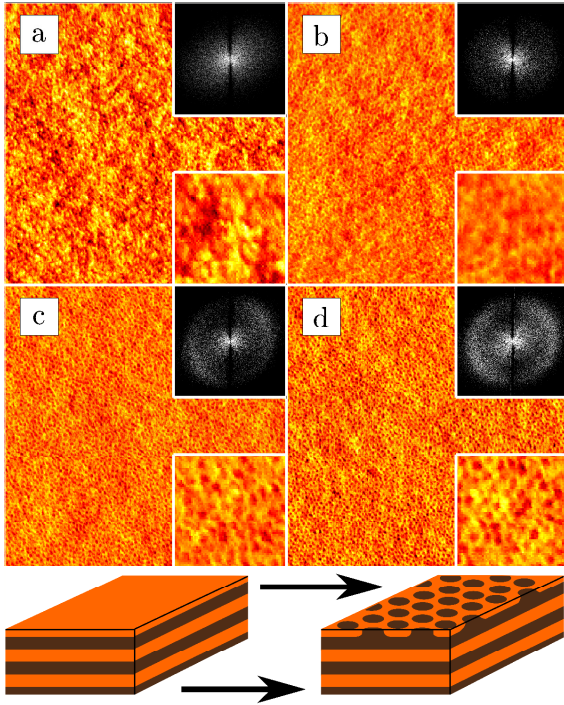


Figure 1 AFM phase images after annealing at 150 °C for (a) $t = 5$ min, (b) $t = 15$ min, (c) $t = 25$ min, and (d) $t = 35$ min. Light regions represent PMMA whereas dark regions represent PS. Each image is $2.5 \mu\text{m}$ wide and has the same vertical (phase) scale range of -0.25 to 0.25 V. The insets display the calculated 2D Fourier transform of each image (top) and a magnified $0.5 \mu\text{m}$ wide image of perforations (bottom). The bottom schematic outlines the transition that we suspect is occurring through this annealing process.

where we can observe the changes with AFM[†]. In this configuration, we expect the film surface to decompose into regions of commensurate thickness for symmetric wetting conditions at equilibrium, exposing PS at the free interface. Annealing at 150 °C and imaging at 5 minute intervals with AFM, we observed a flat film surface with no change in film topology. However, though there was no measurable change in the topology, the AFM phase images revealed a change in morphology at the free surface.

AFM phase images of the evolution of a film with $h_0 = 198 \pm 1 \text{ nm}$ ($\approx 7.5L_0$) are shown in Figure 1. Before annealing,

[†]The case where the PMMA block is in contact with the PS substrate was studied as well. However no changes in morphology or topology were observed at the free surface for this orientation due to the frustration being localized at the substrate.

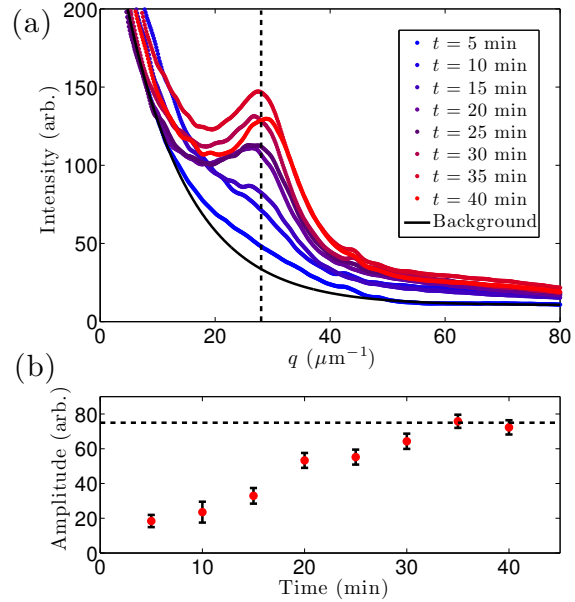


Figure 2 (a) Radial average of 2D Fourier transform intensity of AFM phase image as a function of wavevector, q , for a sequence of 5 minute annealing steps at 150 °C. The dashed lines indicates the growth of a peak at $q \approx 28 \mu\text{m}^{-1}$. The curves are fit to an exponential background function (black line) plus a Gaussian signal peak. (b) Amplitude of the Gaussian signal peak as a function of annealing time, the dashed line indicates the maximum amplitude in peak intensity.

the film surface is flat in topology and featureless in the phase image. This is expected as the equilibrium morphology on mica consisted of solely PMMA at the mica/diblock interface (the interface that is exposed after transfer to the PS substrate) and thus shows no major changes in morphology at the film surface. After annealing at 150 °C for 5, 15, 25, and 35 minutes, an array of circular PS domains grow at the surface, indicated by the dark regions in the images (shown in Figure 1a-d). The 2D Fourier transform of these images, displayed in the insets of Figure 1, show the the growth of a ring of intensity in the later stages of annealing (Figure 1c-d), indicating a spatial ordering for these PS domains. We suspect this indicates a morphology similar to a perforated lamella (PL) at the surface as shown in the schematic of Figure 1. We note that the schematic outlines the transition for only the top few lamellar layers at the surface of our $7.5L_0$ thick film.

The PL morphology has been known to exist as a metastable intermediate state in order-order transitions of bulk systems^{31,32} though it could possibly exist as a stable morphology

in thin films^{42,47}. The PL morphology we see at the top surface enables some of the favourable PS to be exposed at the free surface through the circular domains. Though the symmetric PS-PMMA copolymer we use assembles into lamellae at equilibrium, the PL morphology satisfies the preference for exposure of the lower surface energy PS domain at the free interface without nucleating islands or holes at the free surface. We suspect this is due to the higher energy barrier of hole and island nucleation in comparison to the cost of bending the lamellar domains at the surface. We investigated the length scale and growth of this PL morphology by calculating the radial average of the Fourier transform for each annealing step (shown in Figure 2a). As the sample was annealed, the growth of a length scale correlation is observed for $q \approx 28 \mu\text{m}^{-1}$, indicating the growth of a morphology with periodicity $\approx 35 \text{ nm}$. The Fourier curves in Figure 2a were fit with the sum of a background exponential decay function and a Gaussian signal peak. The evolution of the Gaussian peak amplitude is shown in Figure 2b, indicating that the PL morphology grows in on a time scale of $\sim 30 \text{ min}$.

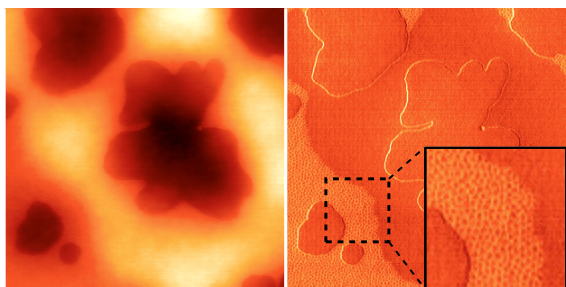


Figure 3 AFM topology (left) and phase (right) images of film after 10 minutes of annealing at $180 \text{ }^\circ\text{C}$. Images are $2.5 \mu\text{m}$ wide. The enlarged portion of the phase image highlights the remaining metastable PL layer.

It has been shown before that the PL morphology is metastable³², and thus to probe the stability of this PL morphology, we anneal the same film at higher temperatures. Upon annealing the film at $180 \text{ }^\circ\text{C}$, the surface begins to nucleate into regions of commensurate height with a terraced topography as can be seen in the topology image shown in Figure 3. The commensurate lamellae replace the metastable perforated lamella that initially formed at the free surface. Specifically, in the initial state the top highly frustrated layer consists of a monolayer of PS-PMMA, with PMMA at the free surface. This frustrated layer ultimately breaks up into a bilayer of PS-PMMA/PMMA-PS and a region exposing the PS block of the layer below, via an intermediate PL morphology.

The commensurate regions in the topography image of Fig-

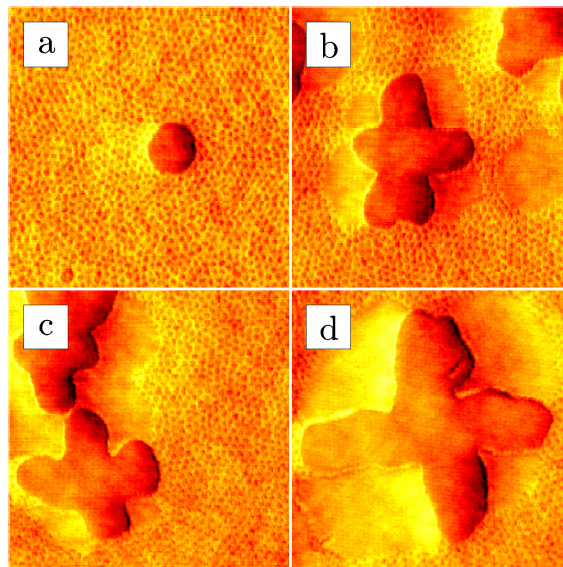


Figure 4 AFM phase images after annealing at $175 \text{ }^\circ\text{C}$ for (a) 5 minutes, (b) 15 minutes, (c) 20 minutes and (d) 25 minutes. Images are $1.25 \mu\text{m}$ wide. We note that these images were not taken of the same hole.

ure 3 (dark and light regions) correspond to featureless regions in the AFM phase image of Figure 3. We note that the phase shift of the featureless commensurate regions and the circular PL domains in the phase image (see enlarged portion of the phase image in Figure 3) are the same, indicating as we presumed that the intermediate morphology is indeed a perforated PMMA lamella with PS domains exposed.

Though small circular holes seem to have nucleated in Figure 3 in the corners of the image, the larger holes (see the one in the centre of Figure 3) have irregular shapes that do not seem to be growing isotropically. In order to investigate this further we annealed at a slightly lower temperature, slowing the process of film equilibration to examine hole growth out of this PL morphology. In Figure 4, we show phase images for a sample ($h_0 \approx 200 \text{ nm}$) annealed at $175 \text{ }^\circ\text{C}$. At early annealing times, small holes with a high degree of curvature are nucleated with a fairly circular, isotropic shape (Figure 4a). However as the holes continue to grow, they form shapes with extended arms (Figure 4b-d), increasing their curvature in comparison to a circular hole of equal volume. This hole growth is reminiscent of the ramified structures formed due to the high degree of strain in the films studied by Koneripalli et al. in Ref.³³. There are many possible sources for this anisotropic growth of holes such as surface defects, film wrinkles, and strain on the lamella at

the film surface due to the step change in boundary conditions. However, though we can not identify which source is the cause of the ramified growth we observe, it is clear from our experiments that the holes grow out of the perforated lamella with shapes that exhibit an increased curvature.

4 Conclusions

The data shown in this paper are the result of a sample preparation technique that allows for the switching of boundary wetting conditions from asymmetric to symmetric for lamellar forming diblock films. Using AFM to observe the order-order transition from commensurate asymmetrically ordered films to their incommensurate symmetrically wetting counterpart, we discovered the formation of an intermediate morphology with a perforated lamella which exposed PS domains at the free surface. This morphology forms to reduce surface energy in the system without nucleating commensurate islands or holes. Upon further annealing the films did nucleate islands and holes out of the metastable intermediate morphology to form equilibrium commensurate film thicknesses. However, the growth of holes was observed to be highly ramified, indicating a preference for growth of holes with a higher degree of curvature out of the PL morphology.

Acknowledgements

Financial Support for this work was provided by National Sciences and Engineering Research Council (NSERC). The authors thank An-Chang Shi for helpful discussions.

References

- [1] T. Kato, *Science*, 2002, **295**, 2414–2418.
- [2] H. K. Bisoyi and S. Kumar, *Chemical Society Reviews*, 2011, **40**, 306–319.
- [3] J. N. Israelachvili, D. J. Mitchell and B. W. Ninham, *Biochimica et Biophysica Acta*, 1977, **470**, 185–201.
- [4] M. Antonietti and S. Forster, *Advanced Materials*, 2003, **15**, 1323–1333.
- [5] G. H. Fredrickson and F. S. Bates, *Ann. Rev. Mater. Sci.*, 1996, **26**, 501–550.
- [6] C. Lee, S. Hyun Kim and T. P. Russell, *Macromolecular Rapid Communications*, 2009, **30**, 1674–1678.
- [7] B. C. Berry, G. Singh, H.-C. Kim and A. Karim, *ACS Macro Letters*, 2013, **2**, 346–350.
- [8] S. Kim, P. F. Nealey and F. S. Bates, *Nano Letters*, 2013, **14**, 148–152.
- [9] S. Pujari, M. A. Keaton, P. M. Chaikin and R. A. Register, *Soft Matter*, 2012, **8**, 5358–5363.
- [10] T. Thurn-Albrecht, J. Schotter, G. A. Kastle, N. Emley, T. Schibauchi, L. Krusen-Ebaum, K. Guarini, K. T. Black, M. T. Tuominen and T. P. Russell, *Science*, 2000, **290**, 2126–2129.
- [11] C. Tang, E. M. Lennon, G. H. Fredrickson, E. J. Kramer and C. J. Hawker, *Science*, 2008, **322**, 429–432.
- [12] N. Kumar, O. Parajuli, A. Gupta and J. I. Hahn, *Langmuir*, 2008, **24**, 2688–2694.
- [13] M. J. Fasolka and A. M. Mayes, *Annu. Rev. Mater. Res.*, 2001, **31**, 323–355.
- [14] I. Hamley, *Progress in Polymer Science*, 2009, **34**, 1161–1210.
- [15] P. F. Green and R. Limary, *Adv. Coll. Int. Sci.*, 2001, **94**, 53–81.
- [16] M. W. Matsen, *J. Phys.: Condens. Matter*, 2001, **14**, R21–R47.
- [17] M. J. Fasolka, P. Banerjee, A. M. Mayes, G. Pickett and A. C. Balazs, *Macromolecules*, 2000, **33**, 5702–5712.
- [18] P. Lambooy, T. P. Russell, G. J. Kellogg, A. M. Mayes, P. D. Gallagher and S. K. Satija, *Physical Review Letters*, 1994, **72**, 2899–2902.
- [19] J. L. Carvalho, M. V. Massa, S. L. Cormier, M. W. Matsen and K. Dalnoki-Veress, *Eur. Phys. J. E*, 2011, **34**, 51.
- [20] M. Matsen, *J. Chem. Phys.*, 1997, **106**, 7781–7791.
- [21] B. Collin, D. Chatenay, G. Coulon, D. Auserre and Y. Gallot, *Macromolecules*, 1992, **25**, 1621–1622.
- [22] S. Joly, A. Raquois, F. Paris, B. Hamdoun, L. Auvray, D. Auserre and Y. Gallot, *Phys. Rev. Lett.*, 1996, **77**, 4394–4397.
- [23] G. Vignaud, A. Bigaud, G. Grubel, S. Joly, D. Auserre, J. F. Legrand and Y. Gallot, *Physica B*, 1998, **248**, 250–257.
- [24] S. Joly, D. Auserre, G. Brotons and Y. Gallot, *Eur. Phys. J. E*, 2002, **8**, 355–363.
- [25] P. F. Green, *J. Polym. Sci. Part B: Polym. Phys.*, 2003, **41**, 2219–2235.
- [26] T. Q. Chastek and T. P. Lodge, *J. Polym. Sci. Part B: Polym. Phys.*, 2005, **44**, 481–491.
- [27] K. S. Lyakhova, A. Horvat, A. V. Zvelindovsky and G. J. A. Sevink, *Langmuir*, 2006, **22**, 5848–5855.
- [28] A. B. Croll, A.-C. Shi and K. Dalnoki-Veress, *Physical Review E*, 2009, **80**, 051803.
- [29] R. D. Peters and K. Dalnoki-Veress, *EPJE*, 2012, **35**, 132.
- [30] R. D. Peters, P. Stasiak, M. W. Matsen and K. Dalnoki-Veress, *ACS Macro Letters*, 2013, **2**, 441–445.
- [31] I. W. Hamley, K. Q. Koppi, J. H. Rosedale and F. S. Bates, *Macromolecules*, 1993, **26**, 5959–5970.
- [32] D. A. Hajduk, H. Takenouchi, M. A. Hillmyer and F. S. Bates, *Macromolecules*, 1997, **30**, 3788–3795.
- [33] N. Koneripalli, F. S. Bates and G. H. Fredrickson, *Physical Review Letters*, 1998, **81**, 1861–1864.
- [34] G. Floudas, R. Ulrich, U. Wiesner and B. Chu, *Europhysics Letters*, 2000, **50**, 182–188.

- [35] M. Imai, A. Saeki, T. Teramoto, A. Kawaguchi, K. Nakaya, T. Kato and K. Ito, *Journal of Chemical Physics*, 2001, **115**, 10525–10531.
- [36] I. W. Hamley, V. Castelletto, O. O. Mykhaylyk, Z. Yang, R. May and A. V. Zvelindovsky, *Langmuir*, 2004, **20**, 10785–10790.
- [37] T. Q. Chastek and T. P. Lodge, *J. Polym. Sci. Part B: Polym. Phys.*, 2006, **44**, 481–491.
- [38] M. Luo, J. E. Seppala, J. N. L. Albert, R. L. Lewis, N. Mahadevapuram, G. E. Stein and T. H. Epps, *Macromolecules*, 2013, **46**, 1803–1811.
- [39] M. W. Matsen, *Physical Review Letters*, 1998, **80**, 4470–4473.
- [40] M. W. Matsen, *Journal of Chemical Physics*, 2001, **114**, 8165–8173.
- [41] R. A. Wickham, A.-C. Shi and Z.-G. Wang, *The Journal of Chemical Physics*, 2003, **118**, 10293–10305.
- [42] D. Q. Ly, T. Honda, T. Kawakatsu and A. V. Zvelindovsky, *Macromolecules*, 2008, **41**, 4501–4505.
- [43] R. K. W. Spencer and R. Wickham, *Soft Matter*, 2013, **9**, 3373–3382.
- [44] S. Wu, *Polymer Interfaces and Adhesion*, Marcel Dekker, New York, 1982.
- [45] C. Ton-That, A. G. Shard, D. O. H. Teare and R. H. Bradley, *Polymer*, 2001, **42**, 1121–1129.
- [46] T. Vu, N. Mahadevapuram, G. M. Perera and G. E. Stein, *Macromolecules*, 2011, **44**, 6121–6127.
- [47] I. Park, S. Park, H.-W. Park, T. Chang, H. Yang and C. Ryu, *Macromolecules*, 2006, **39**, 315–318.

3.4 Manuscript IV

Strain rate effects on symmetric diblock copolymer liquid bridges: order induced stability of polymer fibres

R. D. Peters, K. Dalnoki-Veress, (Submitted to EPJE)

In this study, we switch focus from the thin film geometry to that of liquid bridges. We monitored the break-up of unstable polymer melt bridges to study the effect of shear strain rates on viscosity. Experiments were performed at a variety of different temperatures to probe a wider range of shear strain rates, and superposed using Time-Temperature superposition. We began with measurements on homopolymer polystyrene (PS) of low molecular weight as a reference for measurements made on diblock copolymers. The PS bridges exhibited a shear thinning response in agreement with bulk shear thinning of homopolymers at low shear strain rates, and exhibited shear thickening at high shear strain rates due to the build up of elastic stresses from chain elongation.

Experiments were then performed on symmetric diblock poly(styrene-*b*-2-vinyl pyridine) (PS-P2VP) which has an experimentally accessible ODT at $T_{\text{ODT}} \approx 160$ °C. Measurements were performed both in the disordered and ordered state and superposed using time-temperature superposition. It was found that disordered liquid bridges exhibited similar dynamics and shear response to their homopolymer counterparts. Conversely, the ordered symmetric diblock copolymer bridges demonstrated elevated effective viscosities, indicating an increased fibre stability, and a strictly shear thinning response over the entire shear strain rate range we studied. An explanation for the enhancement of stability was provided by the supposed isotropic orientation of lamellae in the bulk, providing energy barriers to flow within the bridge. As well, the shear thinning was proposed to be caused by the alignment of lamellae along the direction of shear strain rates, providing pathways for copolymer flow from the bridge into the reservoir droplets. More strongly segregated PS-PMMA ordered copolymer bridges were also studied, exhibiting a negligible temperature dependence on effective viscosity over a 20 °C range. This temperature independence indicates a domination

of the dynamics by the lamellar domain alignment and not the viscosities of the individual polymer blocks.

As principal investigator, I developed the experimental apparatus and technique for studying polymer bridges, analyzed the data, and wrote the manuscript. Dr. Kari Dalnoki-Veress contributed by editing the manuscript and with discussions on experimental design and data analysis.

EPJ manuscript No.
(will be inserted by the editor)

Strain rate effects on symmetric diblock copolymer liquid bridges: order induced stability of polymer fibres

Robert D. Peters¹ and Kari Dalnoki-Veress^{1,2a}

¹ Department of Physics & Astronomy and the Brockhouse Institute for Materials Research, McMaster University, Hamilton, Canada

² Laboratoire de Physico-Chimie Théorique, UMR CNRS 7083 Gulliver, ESPCI ParisTech, PSL Research University

September 23, 2014

Abstract. Optical microscopy is used to study the effect of lamellar order on the evolution of polymer-melt bridges. Measurements are performed on symmetric diblock copolymers and linear homopolymers in the melt state. Diblock copolymer bridges measured in the disordered phase are shown to exhibit the same strain rate response as their homopolymer counterparts: shear thinning at low strain rates and shear thickening at high strain rates. However, when measured in the ordered phase, copolymer-melt bridges demonstrate an increased effective viscosity due to the lamellar order and a shear thinning response over the entire range of strain rates probed. The increased viscosity demonstrates an enhanced stability in lamellae forming diblock liquid bridges, presumed to be caused by the isotropic orientational order of lamellar domains that provide energy barriers to flow within the bridge. The shear thinning can be understood as an alignment of lamellae along the axis of the bridge due to flow, facilitating unimpeded diffusion of polymer out of the liquid bridge along lamellar boundaries.

1 Introduction

The breakup of a long cylindrical Newtonian liquid jet into individual droplets is explained by the Plateau-Rayleigh instability. A common example of this phenomenon is the breakup of a thin stream of water from a kitchen faucet into droplets [1]. Though the water exits the faucet as a cylindrical jet, the surface is unstable to perturbations of wavelength greater than the circumference of the jet. The free energy of the thin stream is reduced via a sinusoidal perturbation that grows continuously until the jet is separated into individual droplets. Understanding the breakup of liquid jets allows us to understand many natural systems [1], however it is also vital for understanding and improving various industrial and research applications such as electrospinning [2], inkjet printing [3], and diesel engines [4], to name a few.

The breakup of a cylindrical liquid element may also be observed in the case of an unstable liquid bridge. When a droplet of fluid spanning two solid substrates is separated, for example saliva between your fingers, an axi-symmetric liquid bridge joins the two reservoirs. For small separation distances the outer curvature of the liquid bridge dominates and will induce an attractive capillary force which pulls the substrates back together [5]. However, if the separation distance is large enough then the liquid bridge is unstable as the inner curvature dominates and surface tension causes fluid to drain from the bridge into two reservoir

droplets, one on each substrate [5]. In the case of a slender liquid bridge where the bridge is nearly cylindrical at its midpoint, (ie. the inner curvature is much greater than the outer curvature), the minimum diameter of the bridge, d_{\min} , is known to evolve as

$$d_{\min} = d_0 - 2\alpha \frac{\gamma}{\eta} t, \quad (1)$$

where η is the viscosity of the liquid, γ is the surface tension, and α is a numerical geometric prefactor [6,7]. The geometric factor α has been calculated previously by Papageorgiou to be $\alpha = 0.0709$ for a liquid bridge system [6], and verified experimentally by McKinley and Tripathi [7]. Equation 1 is quite remarkable as it illustrates how one can measure a simple observable parameter in a naturally evolving system, the minimum diameter of a thinning liquid bridge, to extract an important rheological property, the ratio of surface tension to viscosity of a fluid system γ/η . The parameter γ/η is known as the capillary velocity. In the case of a simple Newtonian liquid (η is constant) and a constant surface tension, this leads to a linear decrease in filament diameter.

Though the breakup of Newtonian liquid jets and bridges is well understood [1], when additives, such as polymers, are included in a liquid jet or bridge system, the physics of breakup may become highly non-linear due to viscoelastic effects. An area of intense research focus is the breakup of dilute polymer solutions [8–17] and polymer melts [18–22]. In bulk polymer rheology, it is known that for sufficiently

^a e-mail: dalnoki@mcmaster.ca

high strain rates, polymer melts exhibit a shear thinning property such that

$$\frac{\eta}{\gamma} = \dot{\epsilon}^\nu, \quad (2)$$

where $\nu < 0$ for shear thinning and $\dot{\epsilon}$ is the strain rate applied to the bulk polymer melt. For a Newtonian liquid $\nu = 0$, while $\nu > 0$ denotes shear thickening. In the case of bulk polymer systems, shear thinning has been measured with a power law exponent as large as $\nu \sim -0.85$ [23]. However, as axially symmetric polymer systems such as liquid jets and bridges evolve toward pinch-off, regions which experience a local decrease in radius also experience a stretching of the fluid element in that region, extending the polymer chains along with it. This stretching of the polymer chains by the extensional flow creates a build up of elastic stresses resulting in an increase in effective viscosity, or a shear thickening, of the liquid [8–22]. The onset of this shear thickening has been observed in dilute polymer solutions for shear strain rates that are comparable to the inverse of the polymer relaxation time [10]. This shear thickening has been shown to increase the viscosity by orders of magnitude in dilute solutions of high molecular weight polymer [8–16]. The large elongational strain rates experienced at the midpoint of a cylindrical filament, $\dot{\epsilon}$, are the source of the shear thickening and are calculated as

$$\dot{\epsilon} = \frac{1}{l} \frac{dl}{dt} = -\frac{2}{d_{\min}} \frac{d}{dt} (d_{\min}), \quad (3)$$

where l is the length of the cylindrical fluid element which is stretched upon liquid bridge thinning [11]. This localized shear thickening in regions near pinch off leads to a variety of interesting viscoelastic effects in the breakup of both liquid bridge [13, 14] and liquid jet [24] homopolymer systems.

Though extensive research has been performed on the breakup of jets and bridges both for homopolymer solutions and melts, very little has been reported on the effect of diblock copolymer architecture on the dynamics in these axially symmetric systems. Diblock copolymers consist of two chemically distinct homopolymer chains that are covalently bonded together. In the liquid state, the incompatibility between the two polymer blocks can favour phase separation at temperatures that are sufficiently low. Due to the connectivity of the two blocks, macroscale phase separation is not possible, thus diblock copolymer molecules are known to self assemble into unique microstructures which depend on the relative lengths of the two polymer chains [25, 26]. A symmetric diblock, where both blocks take up a similar volume, will microphase separate into a lamellar morphology. The lamellar thickness, L_0 , is dependent on the molecular weight of the diblock and determined by the balance of both entropic and enthalpic energy terms [25]. However, as temperature is increased, the lamellar order can be destroyed as entropy becomes dominant, and the system favours mixing. The order disorder transition temperature, T_{ODT} , is determined by the relative incompatibility of the two blocks and the length of the copolymer chain [25].

A number of experimental studies have shown that diblock copolymer order has a significant effect on the rheological properties in the melt state (for example [25, 27, 28]). In particular, diblock copolymers in the disordered state can exhibit properties similar to Newtonian liquids [25]. However, in the ordered state the lamellar morphology of symmetric diblock copolymer restricts flow depending on strains and strain rates [25, 28]. Here we investigate the effect of strain rate dependant rheological properties on the thinning dynamics of symmetric diblock copolymer melt bridges.

2 Experiment

2.1 Sample preparation

All measurements were performed with low polydispersity symmetric diblock copolymer and homopolymer purchased from Polymer Source Inc. (Dorval, Quebec). The homopolymers used were polystyrene (PS) and poly(2-vinylpyridine) (P2VP), while the diblocks were poly(styrene-*b*-2-vinylpyridine) (PS-*b*-P2VP) and poly(styrene-*b*-methyl methacrylate) (PS-*b*-PMMA) see Table 1 for details. All polymers were dissolved in toluene to form concentrated solutions with $\sim 25 - 40\%$ polymer by weight.

Table 1. Polymers used in this study. M_n is the number averaged molecular weight and PI is the polydispersity index.

Polymer	M_n (kg/mol)	PI
PS	8.0	1.10
PS	16.0	1.03
P2VP	15.5	1.04
PS- <i>b</i> -P2VP	8.2- <i>b</i> -8.3	1.09
PS- <i>b</i> -PMMA	25- <i>b</i> -26	1.09

A schematic of our experimental setup is shown in Figure 1. One polymer droplet is deposited on a glass substrate that is mounted perpendicular to a freshly cleaved Si wafer (University Wafer, USA). A second droplet of the same polymer is deposited on a glass substrate that is attached to a stiff micropipette. The micropipette is affixed to a multi-axis translation stage that allows us to manoeuvre the polymer droplets in and out of contact. The entire experimental setup is then placed on a modified optical microscope hot stage (Linkam Scientific THMS 600, United Kingdom) capable of elevating the temperature, T , of the polymer above the glass transition and into the melt state. To ensure consistent temperature regulation, the experimentation volume is enclosed within a metal ring and capped with a sapphire window. The metal ring is in intimate contact with the heating block of the hot stage, and the sapphire window is in contact with the metal ring. The conductive contacts and high thermal conductivity of sapphire all ensure that the temperature is well known and well controlled. All polymer droplets are annealed $\sim 50^\circ\text{C}$ above the glass transition temperature for sufficient time (~ 30 min) to remove all toluene from the system and

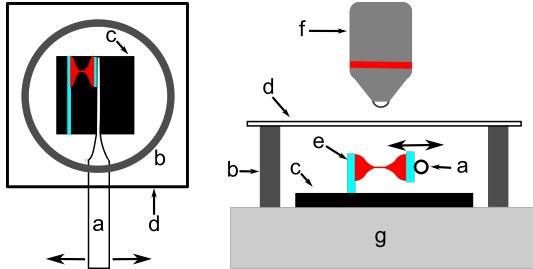


Fig. 1. Schematic of experimental setup from top view (left) and side view (right). The labels shown correspond to the different components of the setup: a) pipette, b) metal ring, c) Si wafer, d) sapphire window, e) glass substrate, f) microscope objective, g) hot stage. The pipette can be translated as indicated by the arrows in order bring the two droplets together and prepare the liquid bridge.

allow the droplets to relax to equilibrium spherical caps before measurements are performed.

A measurement is executed by bringing two polymer droplets into contact, causing them to coalesce (see Fig. 1). The droplets are then separated quickly to a fixed distance, forming a liquid bridge that is unstable. The evolution of the polymer bridge is then monitored on an optical microscope in reflection mode (Olympus BX51, Canada). The silicon wafer provides a highly reflective background, creating high contrast between the polymer bridge and its surroundings, facilitating image analysis of the liquid bridge profile.

2.2 Time-Temperature superposition

Measurements are performed over a wide range of temperatures in order to observe a broad range of dynamics. It is important to note that for all polymers used in this study, surface tension is known to vary by less than 10% over the temperature ranges used in these experiments [29], and is not dependent on the shear strain rates. However, as will be shown below, the viscosity changes by orders of magnitude. Thus, we ignore the small changes in surface tension and focus instead on the temperature and strain rate effects on viscosity which play the dominant role in dynamics. As the temperature response of the viscosity in polymeric systems is well understood, we use the Williams-Landel-Ferry (WLF) equation to perform time-temperature superposition such that all experimental time scales are shifted to those of a reference temperature [30]. The WLF equation allows us to calculate shift factors, a_T , for specific temperatures, T , based on the equation

$$\log(a_T) = -\frac{C_1(T - T_0)}{C_2 + (T - T_0)}, \quad (4)$$

where C_1 and C_2 , are empirical constants, and T_0 is the reference temperature chosen to construct the compliance

master curve in bulk rheology measurements. All time coordinates for experiments performed at different temperatures, T_1 and T_2 may be equated through the relation

$$t_1 = \left(\frac{a_{T_1}}{a_{T_2}}\right) t_2, \quad (5)$$

where t_1 and t_2 are the timescales of the experiments performed at temperatures T_1 and T_2 respectively [30]. Using Equations 4 and 5, we can form master curves for experiments performed at a variety of temperatures on the same material. All measurements made above 180 °C were made under N_2 atmosphere to prevent degradation.

3 Results and Discussions

In section 3.1 we discuss the simplest case of the 8 kg/mol PS homopolymer – this simple canonical system will serve as a reference for the measurements on diblock copolymers. In section 3.2 we discuss the diblock copolymers. First a PS-*b*-P2VP with a total molecular weight of 16 kg/mol which has an experimentally accessible T_{ODT} . As will be seen, the lamellar order resulting from the microphase separation in symmetric diblock copolymer melts has a significant effect on the breakup dynamics of the bridges. We will then compare the 16 kg/mol PS-*b*-P2VP to both PS and P2VP homopolymer, both with the same molecular weight as the diblock. Ensuring that the PS-*b*-P2VP, PS, and P2VP all have similar molecular weights facilitates a fair comparison of the dynamics. The second diblock studied is PS-*b*-PMMA diblock which is strongly segregated and serves as a comparison to the PS-*b*-P2VP to investigate the general features of diblock fibres.

3.1 Homopolymer bridges

To facilitate comparison to the more complex case of diblock copolymers, we performed experiments on a linear, 8 kg/mol PS homopolymer, which is well below the entanglement molecular weight. The evolution of a typical homopolymer bridge is shown in Figure 2. Initially, after the droplets are separated, there is significant outer curvature in the bridge (Figure 2a). After a short time, the liquid bridge forms an approximately cylindrical fiber, with negligible outer curvature at the midpoint (Figure 2b) and this liquid cylinder decreases in diameter until its eventual pinch-off (Figure 2c-d). Due to the high contrast between the polymer and the highly reflective Si wafer background, the diameter of the bridge is easily measured as a function of time, resulting in a typical plot shown in Figure 3. In that plot it can be seen that in the early stages, after initial droplet separation, the dynamics are highly non-linear ($t \lesssim 0.5$ min, see also image in Fig. 2a); however, after the bridge evolves to a cylindrical geometry we can use Equation 1 to obtain the evolution of viscosity in the system. In this measurement, when the nearly cylindrical geometry is reached ($t \sim 0.5$ minutes), d_{\min} decreases linearly

with time indicating a constant viscosity. However, as the diameter of the bridge decreases, the bridge evolution deviates from this linearity. Clearly the bridge begins to thin more slowly. Since $1/\eta$ is proportional to the slope of the plot in Figure 3 (see Eq. 1), the slowing down indicates an increasing viscosity for small bridge diameters.

Since an instantaneous η/γ and $\dot{\epsilon}$ can be calculated from $d_{\min}(t)$ using Equations 1 and 3 respectively, we can monitor the effect of strain rate on the viscosity of our system. All results presented hereafter for η/γ as a function of $\dot{\epsilon}$ are calculated from the average of at least 4 separate liquid bridge breakup experiments at each temperature. Measurements on 8 kg/mol PS were performed over a temperature range of 112 °C to 155 °C, allowing us to probe a wide range of different strain rates and polymer viscosities. The viscosity changes by orders of magnitude and is known to be impacted by shear flows in both bulk and liquid bridge systems [22, 23]. By applying time-temperature superposition using Equations 4 and 5, we shift all measurements to a reference temperature of 140 °C obtaining a master curve of all data. We use WLF shift parameters for PS of $C_1 = 15$ °C, $C_2 = 60$ °C, and $T_0 = 98$ °C, taken from Ref. [31].

In Figure 4 is shown the data for η/γ and $\dot{\epsilon}$, both without time-temperature superposition (inset) as well as the superposed data for the 8 kg/mol PS. From the inset it is clear that over 4 orders of magnitude in viscosity and strain rate are observed for the different temperatures. The temperature shifted data (main plot) shown in Figure 4, illustrates an excellent collapse of all the data. A transition between two regimes for the viscosity at the midpoint of the homopolymer bridge as a function of strain rate is observed. At low strain rates, the polymer bridge decreases in viscosity as a function of strain rate, indicative of a shear thinning fluid. This shear thinning approaches a power law (see Eq. 2) with an exponent of $\nu \sim -0.85$,

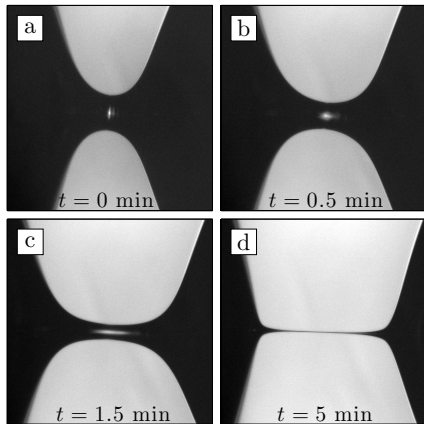


Fig. 2. Optical microscopy images of stages of liquid bridge evolution for 8 kg/mol PS homopolymer melt at 130 °C. All images are 500 μm wide.

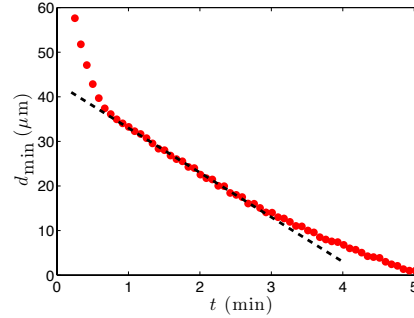


Fig. 3. Typical measurement of minimum diameter (d_{\min}) as a function of time for homopolymer, taken for 8 kg/mol PS bridge at 130 °C. The dashed line identifies the approximately constant viscosity regime after the cylindrical bridge is formed. Deviations from the simple Newtonian fluid can be identified by the decrease in the slope at late times, which corresponds to an increase in viscosity.

indicating bulk shear response in accordance with previous measurements [23]. However, at higher strain rates there is a transition to a shear thickening regime, where the viscosity increases as a function of strain rate within the bridge. This is in response to the high elongational flow experienced in the liquid bridge geometry extending polymer chains, thereby increasing the effective viscosity of the homopolymer melt [10]. The shear thickening effect is not as drastic as in previous experiments [11–16], where viscosity was observed to increase by orders of magnitude, for 2 main reasons. Firstly, our strain rates are lower than in these previous experiments. Secondly, previous experiments were performed primarily on polymer solutions and homopolymers of much larger molecular weight, increasing the relaxation time of the polymer and creating a greater build up of elastic stresses due to extensional flows.

3.2 Symmetric diblock copolymer bridges

Having understood the dynamics in the simple homopolymer system, we now focus on the effect of lamellar ordering of symmetric diblocks on the dynamics of copolymer bridges. We use PS-b-P2VP which has an experimentally accessible bulk T_{ODT} of ~ 160 °C [32]. Simply by changing temperature we can treat this system as a simple homogenous polymer fluid, like the PS homopolymer case discussed above, or as a complex fluid with ordered lamellae. Furthermore, PS-b-P2VP was chosen as both PS and P2VP are similar in terms of chemical composition and have similar rheological properties [33]. As before, we measure the PS-b-P2VP at varying temperatures from 150 °C to 180 °C, thereby capturing the dynamics above and below T_{ODT} . Optical images of evolution and the corresponding typical measurements of $d_{\min}(t)$ are shown in Figure 5 for the disordered state at 175 °C (Figure 5a) and ordered state at 155 °C (Figure 5b). The left-right asym-

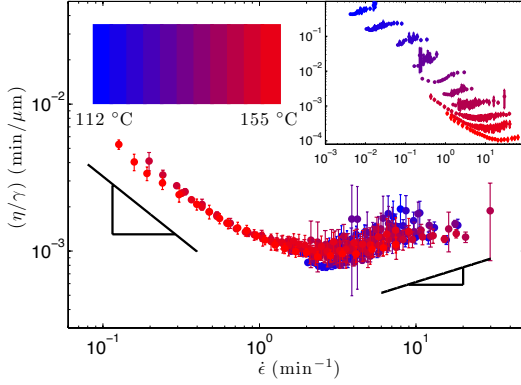


Fig. 4. Measurement of the ratio of viscosity to surface tension as a function of strain rate at the midpoint of the liquid bridge for temperatures of 112 °C to 155 °C for PS with 8 kg/mol. The data has been shifted using the WLF equation as described in the text. The two power law slopes represent guides to the eye for the shear thinning and shear thickening representing power laws of $\nu = -0.85$ and $\nu = 1/3$ respectively in correspondence with Equation 3. The inset demonstrates the unshifted data for each temperature.

metry seen in the optical images reflects slightly different geometries for the left droplet and right droplet prior to coalescence. This asymmetry is not a concern since the system is locally symmetric at the minimum diameter, from where the measurement $d_{\min}(t)$ is obtained. Though it is difficult to compare measurements made at the two temperatures shown in Figure 5, the difference in evolution of $d_{\min}(t)$ is marked. While the disordered diblock copolymer exhibits dynamics similar to what we observed for the homopolymer case (fairly constant viscosity), the ordered lamellar diblock bridge evolves differently, thinning out much faster as the liquid bridge gets thinner and strain rates increase at $t \gtrsim 25$ min.

Since diblock copolymer melts are a complex fluid with nanostructure, it is difficult to define a viscosity or surface tension¹ for the system. However, since the evolution of diblock bridges is cylindrical at the midpoint for the late stages of break-up, we can calculate an effective viscosity, $(\gamma/\eta)_{\text{eff}}$, and strain rate using Equations 1 and 3. The calculation of an effective viscosity in diblock copolymer systems has been performed in the past using bulk rheological techniques [25]. In Figure 6 we show the results of $(\eta/\gamma)_{\text{eff}}$ as a function of $\dot{\epsilon}$. The raw unshifted data is shown in the inset and, as in the homopolymer case, an increase in temperature is accompanied by orders of magnitude decreases in viscosity. However, the shear response of the low temperature lamellar ordered diblock melt is quite different from the high temperature disordered melt,

¹ Again, we stress that though the surface tension may differ, the changes are at the 10% level while the effective viscosity changes by orders of magnitude

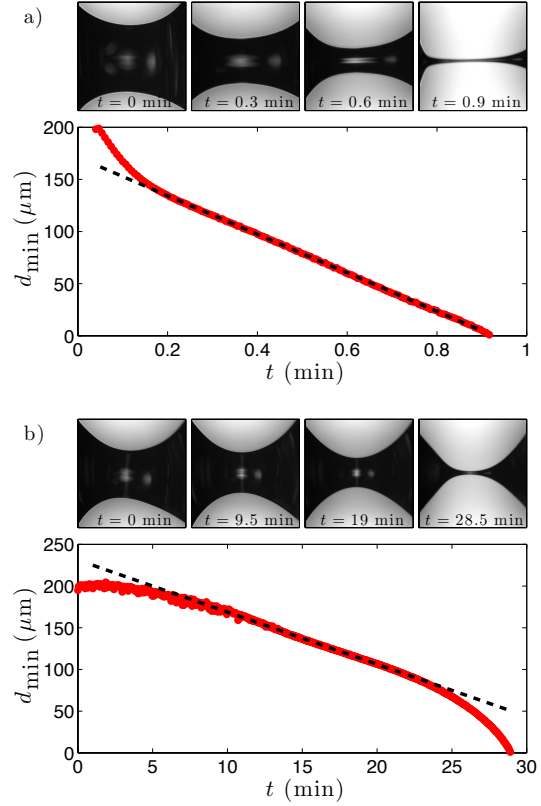


Fig. 5. Typical measurement of the minimum diameter as a function of time for the bridge evolution of PS-b-P2VP in the disordered (top) and ordered (bottom) state at 175 °C and 155 °C respectively. The dashed lines identify the constant viscosity regimes. The optical microscopy images (times indicated) are representative of the breakup of the diblock bridges. The images are 500 μm wide.

exhibiting solely shear thinning response during the liquid bridge evolution. This shear thinning response is entirely consistent with the increasing negative slope of Figure 5b).

In addition to experiments on lamellar forming 16.5 kg/mol PS-b-P2VP, we also performed measurements on 16 kg/mol homopolymer PS and 16 kg/mol homopolymer P2VP melt bridges to facilitate comparison. Since both PS and P2VP exhibit extremely similar rheological properties (both in previous measurements [33] as well as the liquid bridge evolution experiments performed with our experimental setup), we performed time-temperature superposition of all PS, P2VP and PS-b-P2VP with the same WLF shift parameters as before using Equations 4 and 5. In the main plot of Figure 6 is shown the effective ratio of viscosity to surface tension as a function of strain rate for all three polymer melts superposed to a temper-

6 Peters et al.: Enhanced stability and strain rate effects on symmetric diblock copolymer liquid bridges

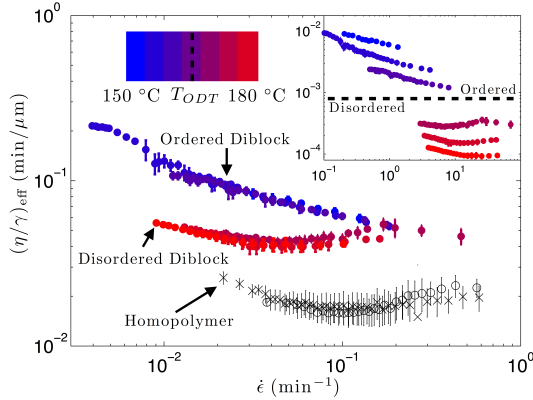


Fig. 6. Measurement of the ratio of viscosity to surface tension as a function of strain rate during bridge evolution for 16 kg/mol PS-b-P2VP (filled circles), 16 kg/mol linear PS (open circles), and 16 kg/mol linear P2VP (x). All the data in the main plot has been superposed using the PS WLF parameters. The inset shows the same PS-b-P2VP data unshifted by time-temperature superposition. The horizontal dashed line indicates the separation between measurements made in the ordered and disordered states.

ature of 140 °C. As expected, the homopolymer PS and P2VP data collapse to similar viscosities and strain rate responses. Just as the 8 kg/mol PS of Figure 4, there is an initial shear thinning regime followed by a shear thickening with increasing shear strain rate. However, when we perform time-temperature superposition on the diblock copolymer data, we obtain a remarkable collapse of the data to *two* markedly different master curves corresponding to the ordered and disordered diblock phases.

All experiments performed in the disordered phase, collapse to a single curve that exhibits a similar shear response to that of the homopolymer PS and P2VP systems, whereby there is a shear thinning effect at low strain rates, and a shear thickening effect at high strain rates. At these high temperatures, there is no order and the homogeneous diblock system is rheologically equivalent to a homopolymer. This result is in agreement with measurements performed on bulk disordered diblock copolymers, where similar rheological properties to simple homopolymers were observed [25,28]. One interesting and surprising result for disordered diblock bridges is that though they have similar shear responses, they exhibit increased effective viscosity in comparison to the experiments on homopolymers of each block, though all three molecules were chosen to have very similar molecular weight. We speculate that this may be caused by an increased energy cost of flowing unlike blocks past each other in the melt, even in the disordered case where the diblock copolymers are a homogeneous mixture.

The measurements made in the ordered lamellar phase, below T_{ODT} , collapse to a distinct second curve. The mea-

surements on ordered diblock copolymer demonstrate an elevated effective viscosity at low shears in comparison to measurements made in the disordered state, indicating an enhanced stability of ordered diblock melt bridges. Additionally, the strain rate response is shear thinning throughout the entire measurement, recombining with the disordered data only at the largest strain rates just before bridge breakup. Since all measurements were performed on the same diblock copolymer droplets, *the difference in dynamics is attributed solely to the effect of order on the flow* in symmetric diblock bridges.

In order to understand the results for the lamellar ordered diblock, we first revisit the length scales in the system. The symmetric diblock copolymer orders with a repeating bilayer thickness on the ~ 10 nm length scale, $L_0 \approx 13.5$ nm, whereas the polymer bridge diameter is initially 10's to 100's of microns in diameter. This represents a difference of 10^3 - 10^4 in length scale between the lamellae and the entire system, indicating that we may treat our liquid bridges as an unconfined, bulk system with regard to the diblock ordering. In bulk symmetric diblock copolymer systems ordered under low shear or no shear, the orientation of lamellar domains is isotropic [25]. Thus, within our bridge there are lamellae oriented in many different directions. Though polymer may flow along the boundary of a lamella continuously, there is an energy barrier to hopping from one lamellar layer to another [34], or hopping across defects between lamellae of different orientations [35]. The energy barrier to layer hopping or motion across a defect is induced by the energy cost of moving a polymer block through a region of unlike polymer. In the case of our ordered symmetric diblock melt bridges, due to the isotropic orientations of the lamellae, there are countless energy barriers that must be overcome in flowing polymer from the centre of the bridge to the reservoir droplets. These energy barriers impede flow and consequently increase the effective viscosity of the system and the inherent stability of the polymer bridge.

We now turn to the shear thinning that is observed over the entire range of shear strain rate explored for the ordered diblocks. As the ordered diblock bridge thins in diameter, strain rates increase and as is evident from Figure 6, the effective viscosity decreases. It is known that in the case of oscillatory shear measurements made on bulk symmetric diblock copolymer melts in the ordered phase, the lamellar domains may become aligned with shear forces dependent on annealing history as well as the amplitude and frequency of shear [36]. Additionally, the application of sufficiently large shear stress is known to align lamellae, cylinders and spheres in block copolymer thin films [37,38]. The process is believed to occur through the destruction of ordered domains not oriented parallel to the shear stress, and the subsequent reformation of ordered structures in alignment with applied shear [39,40]. Since we measure shear thinning in our measurements on ordered diblock melt bridges, we suggest that the strain rates within the bridge are in the regime where lamellae are forced to align such that the normal vector to the lamellae are directed perpendicular to the flow. This ori-

entation would allow copolymer to travel more efficiently along the lamellar boundaries, flowing into the reservoir droplets without having to hop between lamellae or across as many defects. As the strain rates increase, the lamellae become increasingly more aligned and the effective viscosity correspondingly decreases.

In addition to this shear thinning effect, it is evident from Figure 6 that measurements made both above and below T_{ODT} converge at high strain rates to the same effective viscosity. There are two possible explanations for this convergence; the disordered phase is ordering under shear *or* the ordered phase is disordering. In bulk systems, oscillatory shear has been shown to increase the T_{ODT} for lamellar forming diblocks, and the domains created under these conditions are aligned such that flow is possible along the lamellar boundaries [41, 42]. Therefore, it seems likely that under the strain rates experienced in our measurements, the disordered diblock is ordering lamellae at high strain rates such that flow is less impeded and dynamics are identical to measurements performed below bulk T_{ODT} . Indeed this suggestion is further evidenced by the fact that the disordered diblock, rather than continuing along the trend of shear thickening with increasing $\dot{\epsilon}$ actually follows perfectly the extrapolated shear thinning trend of the ordered diblock.

Bridge evolution measurements were also performed on a 51 kg/mol PS-b-PMMA symmetric diblock copolymer which has an experimentally unaccessible T_{ODT} , and thus contains more strongly segregated lamellae than its PS-b-P2VP counterpart [43]. Polymer-melt bridge evolution was investigated at 220, 230 and 240 °C for the PS-b-PMMA melt in a N_2 atmosphere. In Figure 7 we plot the effective viscosity divided by surface tension as a function of strain rate for the PS-b-PMMA copolymer without performing any time-temperature shifts. It is clear that for this highly ordered polymer melt, a shear thinning effect is once again observed due to the shear alignment of lamellae along the direction of flow within the bridge. However, it is interesting to note that in the case of this highly ordered symmetric diblock, the effect of temperature seems to be negligible since the dynamics at all 3 temperatures seem to overlap. As the PS-b-PMMA system is more strongly segregated, there is a much larger energy penalty for layer hopping or moving across a defect than for the weakly ordered PS-b-P2VP melt. We speculate that the dynamics are dominated by the shear alignment of the lamellae, rather than the viscosity effects of the individual polymer blocks, resulting in identical dynamics for measurements at different temperatures.

An increase in effective viscosity upon lamellar ordering and a decrease in viscosity upon application of strain has been observed previously in oscillatory shear rheology experiments [25, 27, 28]. In particular, Schulz et al. performed measurements on a PS-P2VP diblock copolymer and observed a discontinuity in the rheological properties as a function of temperature for constant shear rates [27]. This discontinuity is consistent with a transition from the ordered to the disordered curves in Figure 6. The collapse of ordered and disordered data with only time-

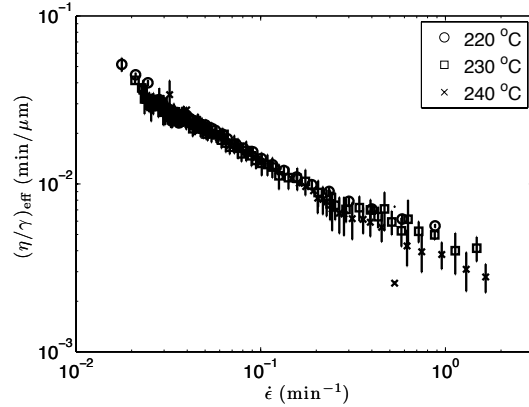


Fig. 7. Measurements of effective viscosity divided by surface tension as a function of strain rate for a 51 kg/mol PS-b-PMMA symmetric copolymer. Measurements are not shifted using time-temperature superposition.

temperature superposition from a direct observation of bridge diameter supports previous rheological measurements of symmetric diblock copolymer. As well, the additional complexity of the elongational flows within the axisymmetric liquid bridges provides a useful method for studying complex macromolecular fluids where molecule extension or alignment may play a key role in the resultant dynamics.

4 Conclusions

Using optical microscopy we have investigated the effect of the lamellar order in symmetric diblock copolymer melts on the dynamics of unstable polymer-melt bridges. In the disordered phase, symmetric diblock copolymer melts were observed to exhibit similar dynamics to their homopolymer counterparts: at low strain rates, a shear thinning response due to bulk shear effects, followed by a shear thickening response due to polymer extension at high strain rates. Though qualitatively similar to the homopolymers in response to strain rate, the symmetric diblock copolymer in the disordered state was measured to have higher effective viscosity than the homopolymers. In the ordered phase, symmetric diblock copolymers were observed to be markedly different from disordered. The ordered system was more stable, with a higher effective viscosities in comparison to the disordered phase. This enhanced stability may be attributed to the energy barriers to flow induced by the isotropic orientation of lamellae. As strain rates increased, a shear thinning response was measured consistent with an alignment of lamellae which facilitates flow of polymers from the bridge into the adjacent droplets. In the case of the strongly segregated lamellar forming diblock, PS-b-PMMA, the effect of temperature was negligible in comparison to the shear thinning effect in the

8 Peters et al.: Enhanced stability and strain rate effects on symmetric diblock copolymer liquid bridges

liquid bridge evolution, exhibiting identical dynamics over a 20 °C temperature range. The ability of diblock copolymers to prevent break-up and enhance the stability of liquid fibres may be useful for the production of textiles or in the creation of electrospun fibres.

Financial Support for this work was provided by National Sciences and Engineering Research Council (NSERC). The authors thank Mark Matsen and An-Chang Shi for helpful discussions.

References

- J. Eggers, E. Villermaux, Rep. Prog. Phys. **71**, 036601 (2008)
- D.H. Reneker, A.L. Yarin, Polymer **49**, 2387 (2008)
- B.J. de Gans, P.C. Duineveld, U.S. Schubert, Advanced Materials **16**, 203 (2004)
- C. Arcoumanis, J.H. Whitelaw, Journal of Mechanical Engineering Science **201**, 57 (1987)
- L.E. Johns, R. Narayanan, *Interfacial Instability* (Springer, New York, 2002)
- D.T. Papageorgiou, Physics of Fluids **7**, 1529 (1995)
- G.H. McKinley, A. Tripathi, Journal of Rheology **44**, 653 (2000)
- V.M. Entov, E.J. Hinch, J. Non-Newtonian Fluid Mech. **72**, 31 (1997)
- M.I. Kolte, P. Szabo, Journal of Rheology **43**, 609 (1999)
- Y. Amarouchene, D. Bonn, J. Meunier, H. Kellay, Physical Review Letters **86**, 3558 (2001)
- S.L. Anna, G.H. McKinley, Journal of Rheology **45**, 115 (2001)
- C. Clasen, J. Eggers, M.A. Fontelos, J. Li, G.H. McKinley, Journal of Fluid Mechanics **556**, 283 (2006)
- R. Sattler, C. Wagner, J. Eggers, Physical Review Letters **100**, 164502 (2008)
- P.P. Bhat, S. Appathurai, H.M. T., M. Pasquali, G.H. McKinley, O.A. Basaran, Nature Physics **6**, 625 (2010)
- R. Sattler, S. Gier, J. Eggers, C. Wagner, Physics of Fluids **24**, 023101 (2012)
- A.V. Bazilevskii, Fluid Dynamics **48**, 97 (2013)
- J. Eggers, Physics of Fluids **26**, 033106 (2014)
- A. Bach, K. Almdal, H.K. Rasmussen, O. Hassager, Macromolecules **36**, 5174 (2003)
- M.H. Wagner, S. Kheirandish, O. Hassager, Journal of Rheology **49**, 1317 (2005)
- Y. Wang, P. Boukany, S.Q. Wang, X. Wang, Physical Review Letters **99**, 237801 (2007)
- H.K. Rasmussen, K. Yu, Physical Review Letters **107**, 126001 (2011)
- M.H. Wagner, V.H. Rolon-Garrido, Journal of Rheology **56**, 1279 (2012)
- W.W. Graessley, Adv. Polym. Sci. **16**, 1 (1974)
- C. Clasen, J. Bico, V. Entov, G.H. McKinley, Journal of Fluid Mechanics **636**, 5 (2009)
- G.H. Fredrickson, F.S. Bates, Ann. Rev. Mater. Sci. **26**, 501 (1996)
- M.J. Fasolka, A.M. Mayes, Annu. Rev. Mater. Res. **31**, 323 (2001)
- M. Schulz, A. Khandpur, F.S. Bates, K. Almdal, K. Mortensen, D. Hajduk, S. Gruner, Macromolecules **29**, 2857 (1996)
- J.H. Rosedale, F.S. Bates, Macromolecules **23**, 2329 (1990)
- S. Wu, The Journal of Physical Chemistry **74**, 632 (1970)
- M.L. Williams, R.F. Landel, J.D. Ferry, Journal of the American Chemical Society **77**, 3701 (1955)
- J.E. Mark, ed., *Physical Properties of Polymers Handbook* (AIP Press, New York, 1996)
- A.B. Croll, A.C. Shi, K. Dalnoki-Veress, Physical Review E **80**, 051803 (2009)
- Y. Takahashi, N. Ochiai, Y. Matsushita, I. Noda, Polymer Journal **28**, 1065 (1996)
- A.B. Croll, M.W. Matsen, A.C. Shi, K. Dalnoki-Veress, European Physical Journal E **27**, 407 (2008)
- D. Duque, K. Katsov, M. Schick, Journal of Chemical Physics **117**, 10315 (2002)
- V.K. Gupta, R. Krishnamoorti, Z.R. Chen, J.A. Kornfield, S.D. Smith, M.M. Satkowski, J.T. Grothaus, Macromolecules **29**, 875 (1996)
- A.P. Marencic, D.H. Adamson, P.M. Chaikin, R.A. Register, Physical Review E **81**, 011503 (2010)
- G. Singh, K.G. Yager, B. Berry, H.C. Kim, A. Karim, ACS Nano **6**, 10335 (2012)
- S. Pujari, M.A. Keaton, P.M. Chaikin, R.A. Register, Soft Matter **8**, 5858 (2012)
- B.L. Peters, A. Ramirez-Hernandez, D.Q. Pike, M. Muller, Macromolecules **45**, 8109 (2012)
- K.A. Koppi, M. Tirrell, F.S. Bates, Physical Review Letters **70**, 1449 (1993)
- L. You, Y.D. HE, Y. Zhao, Z.Y. Lu, Journal of Chemical Physics **129**, 204901 (2008)
- T.P. Russell, R.P. Hjelm, P.A. Seeger, Macromolecules **23**, 890 (1990)

Chapter 4

Conclusions

In the research contained within this dissertation, we have studied the dynamics of symmetric diblock copolymer melts in both the thin film and liquid bridge geometries. We began by investigating the effect of incommensurability on the dynamics of island and hole formation at the film surface of symmetric diblock copolymer films when ordering from the spincast, homogeneous state. In the case of moderately incommensurate films, we found that the measurement of three distinct regimes in the ordering process was possible. First, an ordering regime which consisted of the formation of parallel lamellae of non-equilibrium lamellar spacing. Second, an incubation regime was observed followed finally by a nucleation regime, when islands and holes began to nucleate at the surface of the film. The ordering time was found to depend on the total film thickness, taking longer to reach the intermediate state in thicker films due to the necessity of forming more lamellar layers. As well, the incubation time was found to increase by up to 2 orders of magnitude as it approached commensurate thicknesses. This incubation time was modelled successfully with a simple calculation using classical nucleation theory and assuming strong segregation of the two blocks. However, this model failed for highly incommensurate films as the intermediate state of parallel lamellae with non-equilibrium bilayer width became kinetically unfavourable. As a consequence, an intermediate state of mixed morphology was found to exist for maximally incommensurate films, where lamellae were oriented parallel at the substrate, and perpendicular at the film surface. This morphology was found to be unstable through SCFT calculations, explaining the existence of a spinodal decomposition of

the film surface in highly incommensurate films. The changeover in dynamics from nucleation to spinodal was induced simply by changing initial film thickness, illustrating the impact that the equilibrium ordered structures of diblock copolymers can have on dynamics in confined systems.

In our next work, we considered the evolution of symmetric diblock copolymer films which were equilibrated and commensurate under asymmetric wetting conditions. Films were then transferred to a symmetrically wetting substrate, resulting in the higher surface energy block being exposed at the free interface. The resultant film was maximally incommensurate as in the previous study, but already ordered with equilibrium width lamellar bilayers oriented parallel to the substrate. Upon annealing, the lamellar monolayer at the free surface developed curvature in the lamellar domains to form a perforated lamella (PL) at the free surface, exposing the lower surface energy PS at the interface. Upon further annealing, this metastable PL morphology was shown to nucleate islands and holes at the free surface as expected, however hole growth exhibited a ramified structure, displaying higher curvature hole growth out of the PL morphology.

In our final study, we measured the effect of symmetric diblock copolymer on the dynamics within liquid bridges. It was observed that the diblock copolymer in the disordered state displayed similar properties to its homopolymer counterparts: a shear thinning response at low shear strain rates and a shear thickening response at high shear strain rates. However, the ordering of diblock copolymers significantly changed the dynamics of break-up within the liquid bridges, enhancing the stability through an increase in the effective viscosity, and displaying shear thinning response over all shear strain rates probed. The enhanced stability was proposed to be induced by an isotropic orientational order of lamellae within the bridge providing numerous energy barriers to flow. The shear thinning was then postulated to be caused by the alignment of diblock copolymer domains under the strain rates in the axisymmetric bridge, providing pathways for the diblock copolymer to move throughout the bridge along domain boundaries.

These studies all highlight the interesting effects that even one of the simplest copolymers, the symmetric diblock copolymer, can have on dynamics in various geometries. By simply changing the initial conditions in the first three studies on thin

films, we were able to study three significantly different sets of equilibration kinetics. As well, in studying the dynamics of symmetric diblock bridges, we encountered a practical enhancement of the stability in liquid fibres induced through symmetric diblock order while observing a shear thinning dynamic response. This enhancement of stability that we observed is just one example of the importance of understanding dynamics in ordered copolymer systems. It is easy to see that though they are quite complex, understanding the kinetics of diblock ordering processes and non-equilibrium dynamics is the first step toward having a global control over their final structures, and consequently their desirable physical properties.

Appendix A

Works not included in thesis

A.1 Paper I

Hierarchical, self-similar structure in native squid pen

F.-C. Yang, R. D. Peters, H. Dies, M. C. Rheinstädter, *Soft Matter* **10**, 5541-5549 (2014).

A.2 Paper II

The Rayleigh-Plateau instability on a fiber revisited: Influence of the hydrodynamic boundary condition

S. Haefner, O. Bäumchen, M. Benzaquen, T. Salez, R. D. Peters, J. D. McGraw, E. Raphael, K. Jacobs, K. Dalnoki-Veress, (In Preparation)

Bibliography

- [1] G. M. Whitesides and B. Grzybowski. Self-assembly at all scales. *Science*, 295:2418–2421, 2002.
- [2] G. H. Fredrickson and F. S. Bates. Dynamics of block copolymers: Theory and experiment. *Annual Review in Materials Science*, 26:501 – 550, 1996.
- [3] M. Rubinstein and R. H. Colby. *Polymer Physics*. Oxford University Press, New York, USA, 2003.
- [4] P. G. DeGennes. *Scaling Concepts in Polymer Physics*. Cornell University Press, USA, 1979.
- [5] G. R. Strobl. *The Physics of Polymers*. Springer Berlin, 2nd edition, 1997.
- [6] P. J. Flory. Thermodynamics of high polymer solutions. *The Journal of Chemical Physics*, 10:51–61, 1942.
- [7] M. L. Huggins. Some properties of solutions of long-chain compounds. *The Journal of Physical Chemistry*, 46:151–158, 1942.
- [8] R.A.L. Jones. *Soft Condensed Matter*. Oxford University Press, New York, USA, 2002.
- [9] J. E. Mark, editor. *Physical Properties of Polymers Handbook*. AIP Press, New York, 1996.

-
- [10] G. Reiter. Dewetting of thin polymer films. *Physical Review Letters*, 68:75–78, 1992.
- [11] J. Bischof, D. Scherer, S. Herminghaus, and P. Leiderer. Dewetting modes of thin metallic films: Nucleation of holes and spinodal dewetting. *Physical Review Letters*, 77:1536–1539, 1996.
- [12] R. Xie, A. Karim, J. F. Douglas, C. C. Han, and R. A. Weiss. Spinodal dewetting of thin polymer films. *Physical Review Letters*, 81:1251–1254, 1998.
- [13] R. Seemann, S. Herminghaus, and K. Jacobs. Dewetting patterns and molecular forces: A reconciliation. *Physical Review Letters*, 86:5534–5537, 2001.
- [14] J. Eggers and E. Villermaux. Physics of liquid jets. *Reports on Progress in Physics*, 71:036601, 2008.
- [15] S. Qi and Z.-G. Wang. Kinetic pathways of order-disorder and order-order transitions in weakly segregated microstructured systems. *Physical Review Letters*, 76:1679–1682, 1996.
- [16] R. A. Wickham, A.-C. Shi, and Z.-G. Wang. Nucleation of stable cylinders from a metastable lamellar phase in diblock copolymer melt. *The Journal of Chemical Physics*, 118:10293–10305, 2003.
- [17] X. Cheng, L. Lin, E. Weinan, P. Zhang, and A-C Shi. Nucleation of ordered phases in block copolymers. *Physical Review Letters*, 104:148301, 2010.
- [18] J. W. Cahn and J. E. Hilliard. Free energy of a nonuniform system. i. interfacial free energy. *The Journal of Chemical Physics*, 28:258–267, 1958.
- [19] J. W. Cahn. Phase separation by spinodal decomposition in isotropic systems. *The Journal of Chemical Physics*, 42:93–99, 1965.
- [20] M. L. Williams, R. F. Landel, and J. D. Ferry. The temperature dependence of relaxation mechanisms in amorphous polymers and other glass-forming liquids. *Journal of the American Chemical Society*, 77:3701–3707, 1955.

- [21] W. W. Graessley. The entanglement concept in polymer rheology. *Adv. Polym. Sci.*, 16:1–179, 1974.
- [22] M. W. Matsen and M. Schick. Self-assembly of block copolymers. *Current Opinion in Colloid & Interface Science*, 1:329–336, 1996.
- [23] I. Hamley. Ordering in thin films of block copolymers: Fundamentals to potential applications. *Progress in Polymer Science*, 34:1161 – 1210, 2009.
- [24] N. Kumar, O. Parajuli, A. Gupta, and J. I. Hahn. Elucidation of protein adsorption behaviour on polymeric surfaces: toward high-density, high-payload protein templates. *Langmuir*, 24:2688–2694, 2008.
- [25] P. Mansky, Y. Liu, E. Huang, T.P. Russell, and R. C. Hawker. Controlling polymer-surface interactions with random copolymer brushes. *Science*, 275:1458–1460, 1997.
- [26] T. P. Russell. Surface-responsive materials. *Science*, 297:964–967, 2002.
- [27] A. Taubert, A. Napoli, and W. Meier. Self-assembly of reactive amphiphilic block copolymers as mimetics for biological membranes. *Current Opinion in Chemical Biology*, 8:598–603, 2004.
- [28] J. Li, K. A. Pastor, A.-C. Shi, F. Schmid, and J. Zhou. Elastic properties and line tension of self-assembled bilayer membranes. *Physical Review E*, 88:012718, 2013.
- [29] B. M. Discher, Y-Y Won, D. S. Ege, J. C-M. Lee, F. S. Bates, D. E. Discher, and D. A. Hammer. Polymersomes: Tough vesicles made from diblock copolymers. *Science*, 284:1143–1146, 1999.
- [30] M. Muller, Y. G. Smirnova, G. Marelli, M. Fuhrmans, and A.-C. Shi. Transition path from two apposed membranes to a stalk obtained by a combination of particle simulations and string method. *Physical Review Letters*, 108:228103, 2012.
- [31] J. Li, H. Zhang, F. Qiu, and A.-C. Shi. Emergence and stability of intermediate open vesicles in disk-to-vesicle transitions. *Physical Review E*, 88:012719, 2013.

- [32] M. W. Matsen and M. Schick. Stable and unstable phases of a diblock copolymer melt. *Physical Review Letters*, 72:2660–2663, 1994.
- [33] D. A. Hajduk, H. Takenouchi, M. A. Hillmyer, and F. S. Bates. Stability of the perforated layer (pl) phase in diblock copolymer melts. *Macromolecules*, 30:3788–3795, 1997.
- [34] I. Hamley, K. Koppi, J. Rosedale, F. S. Bates, K. Almdal, and K. Mortensen. Hexagonal mesophases between lamellae and cylinders in a diblock copolymer melt. *Macromolecules*, 26:5959–5970, 1993.
- [35] A. N. Semenov. Contribution to the theory of microphase layering in block-copolymer melts. *Sov. Phys. JETP*, 61:1242–1256, 1985.
- [36] A. N. Semenov. Theory of block-copolymer interfaces in the strong segregation limit. *Macromolecules*, 26:6617–6621, 1993.
- [37] T. Ohta and K. Kawasaki. Equilibrium morphology of block copolymer melts. *Macromolecules*, 19:2621–2632, 1986.
- [38] L Leibler. Theory of microphase separation in block copolymers. *Macromolecules*, 13:1602–1617, 1980.
- [39] E. Helfand. Theory of inhomogeneous polymers: Fundamentals of the gaussian random-walk model. *The Journal of Chemical Physics*, 62:999–1005, 1975.
- [40] T. Hashimoto, M. Shibayama, and H. Kawai. Domain-boundary structure of styrene-isoprene block copolymer films cast from solution. 4. molecular weight dependence of lamellar microdomains. *Macromolecules*, 13:1237–1247, 1980.
- [41] K. Mori, H. Hasegawa, and T. Hashimoto. Order-disorder transition of polystyrene-block-polyisoprene part ii. characteristic length as a function of polymer concentration, molecular weight, copolymer composition, and χ parameter. *Polymer*, 42:3009–3021, 2001.
- [42] G. H. Fredrickson and E. Helfand. Fluctuation effects in the theory of microphase separation in block copolymers. *The Journal of Chemical Physics*, 87:697–705, 1987.

- [43] E. Helfand. Block copolymer theory. iii. statistical mechanics of the microdomain structure. *Macromolecules*, 8:552–556, 1975.
- [44] J. D. Vavasour and M. D. Whitmore. Self-consistent mean field theory of the microphases of diblock copolymers. *Macromolecules*, 25:5477–5486, 1992.
- [45] M. Laradji, A.-C. Shi, R. C. Desai, and J. Noolandi. Stability of ordered phases in weakly segregated diblock copolymer systems. *Physical Review Letters*, 78:2577–2580, 1997.
- [46] M. Laradji, A.-C. Shi, J. Noolandi, and R. C. Desai. Stability of ordered phases in diblock copolymer melts. *Macromolecules*, 30:3242–3255, 1997.
- [47] M. W. Matsen. The standard gaussian model for block copolymer melts. *Journal of Physics: Condensed Matter*, 14:R21–R47, 2002.
- [48] B. Yu, P. Sun, T. Chen, Q. Jin, D. Ding, B. Li, and A.-C. Shi. Confinement-induced novel morphologies of block copolymers. *Physical Review Letters*, 96:138306, 2006.
- [49] M. W. Matsen and F. S. Bates. Unifying weak- and strong-segregation block copolymer theories. *Macromolecules*, 29:1091–1098, 1996.
- [50] M. W. Matsen and F. W. Bates. Block copolymer microstructures in the intermediate-segregation regime. *The Journal of Chemical Physics*, 106:2436–2448, 1997.
- [51] P. Stasiak and M. W. Matsen. Monte carlo field-theoretic simulations for melts of symmetric diblock copolymer. *Macromolecules*, 46:8037–8045, 2013.
- [52] G. H. Fredrickson. Surface ordering phenomena in block copolymer melts. *Macromolecules*, 20:2535–2542, 1987.
- [53] T. P. Russell, G. Coulon, V. R. Deline, and D. C. Miller. Characteristics of the surface-induced orientation for symmetric diblock ps/pmma copolymers. *Macromolecules*, 22:4600–4606, 1989.

- [54] S. H. Anastasiadis, T. P. Russell, S. K. Satija, and C. F. Majkrzak. Neutron reflectivity studies of the surface-induced ordering of diblock copolymer films. *Physical Review Letters*, 62:1852–1855, 1989.
- [55] K. R. Shull. Mean-field theory of block copolymers: Bulk melts, surfaces and thin films. *Macromolecules*, 25:2122 – 2133, 1992.
- [56] A. Menelle, T. P. Russell, S. H. Anastasiadis, S. K. Satija, and C. F. Majkrzak. Ordering of thin diblock copolymer films. *Physical Review Letters*, 68:67 – 70, 1992.
- [57] M. D. Foster, M. Sikka, N. Singh, F. S. Bates, S. K. Satija, and C. F. Majkrzak. Structure of symmetric polyolefin block copolymer thin films. *The Journal of Chemical Physics*, 96:8605–8615, 1992.
- [58] P. F. Green and R. Limary. Block copolymer thin films: pattern formation and phase behavior. *Advances in Colloid and Interface Science*, 94:53 – 81, 2001.
- [59] A. B. Croll, A-C. Shi, and K. Dalnoki-Veress. Ordering of a lamella-forming fluid near an interface. *Physical Review E*, 80:051803, 2009.
- [60] J. L. Carvalho, M. V. Massa, S. L. Cormier, M. W. Matsen, and K. Dalnoki-Veress. Reversible sphere-to-lamellae wetting transition at the interface of a block copolymer system. *European Physical Journal E*, 34, 2011.
- [61] W. Li and R. A. Wickham. Self-assembled morphologies of a diblock copolymer melt confined in a cylindrical nanopore. *Macromolecules*, 39:8492–8498, 2006.
- [62] M. Pinna, X. Guo, and A. V. Zvelindovsky. Diblock copolymers in a cylindrical pore. *The Journal of Chemical Physics*, 131:214902, 2009.
- [63] B. Yu, B. Li, Q. Jin, D. Ding, and A-C Shi. Self-assembly of symmetric diblock copolymers confined in spherical nanopores. *Macromolecules*, 40:9133–9142, 2007.
- [64] B. Yu, P. Sun, T. Chen, Q. Jin, D. Ding, B. Li, and A-C Shi. Self-assembled morphologies of diblock copolymers confined in nano channels: Effects of confinement geometry. *The Journal of Chemical Physics*, 126:204903, 2007.

- [65] M. J. Fasolka and A. M. Mayes. Block copolymer thin films: Physics and applications. *Annual Review of Materials Research*, 31:323 – 355, 2001.
- [66] P. F. Green. Wetting and dynamics of structured liquid films. *Journal of Polymer Science: Part B: Polymer Physics*, 41:2219–2235, 2003.
- [67] T. P. Russell. Copolymers at surfaces and interfaces. *Current Opinion in Colloid & Interface Science*, 1:107–115, 1996.
- [68] P. Lambooy, T. P. Russell, G. J. Kellogg, A. M. Mayes, P. D. Gallagher, and S. K. Satija. Observed frustration in confined block copolymers. *Physical Review Letters*, 72:2899–2902, 1994.
- [69] D. G. Walton, G. J. Kellogg, and A. M. Mayes. A free energy model for confined diblock copolymers. *Macromolecules*, 27:6225–6228, 1994.
- [70] M. Kikuchi and K. Binder. Microphase separation in thin films of the symmetric diblock copolymer melt. *The Journal of Chemical Physics*, 101:3367–3377, 1994.
- [71] T. P. Russell, P. Lambooy, G. J. Kellogg, and A. M. Mayes. Diblock copolymers under confinement. *Physica B*, 213:22–25, 1995.
- [72] N. Koneripalli, R. Levicky, F. S. Bates, J. Ankner, H. Kaiser, and S. K. Satija. Confinement-induced morphological changes in diblock copolymer films. *Langmuir*, 12:6681–6690, 1996.
- [73] B. Collin, D. Chatenay, G. Coulon, D. Ausserré, and Y. Gallot. Ordering of copolymer thin films as revealed by atomic force microscopy. *Macromolecules*, 25:1621–1622, 1992.
- [74] M. Maaloum, D. Ausserré, D. Chatenay, and Y. Gallot. Spinodal-decomposition-like patterns via metastable state relaxation. *Physical Review Letters*, 70:2577–2580, 1993.
- [75] S. Joly, A. Raquois, F. Paris, B. Hamdoun, L. Auvray, and D. Ausserré. Early stage of spinodal decomposition in 2d. *Physical Review Letters*, 77:4394–4397, 1996.

- [76] N. Koneripalli, F. S. Bates, and G. H. Fredrickson. Fractal hole growth in strained block copolymer films. *Physical Review Letters*, 81:1861–1864, 1998.
- [77] G. Vignaud, A. Gibaud, G. Grubel, S. Joly, D. Ausserré, J. F. Legrand, and Y. Gallot. Ordering of diblock ps-pbma thin films: An x-ray reflectivity study. *Physica B*, 258:250–257, 1998.
- [78] S. Joly, D. Ausserré, G. Brotons, and Y. Gallot. Hole nucleation in thin diblock copolymer films. *The European Physical Journal E*, 8:355–363, 2002.
- [79] K. S. Lyakhova, A. Horvat, A. V. Zvelindovsky, and G. J. A. Sevink. Dynamics of terrace formation in a nanostructure thin block copolymer film. *Langmuir*, 22:5848–5855, 2006.
- [80] J. L. Goveas and S. T. Milner. Dynamics of the lamellar-cylindrical transition in weakly segregated diblock copolymer melts. *Macromolecules*, 30:2605–1612, 1997.
- [81] M. W. Matsen. Cylinder to gyroid epitaxial transitions in complex polymeric liquids. *Physical Review Letters*, 80:4470–4473, 1998.
- [82] S. Mani, R. A. Weiss, M. E. Cantino, L. H. Khairallah, S. F. Hahn, and C. E. Williams. Evidence for a thermally reversible order-order transition between lamellar and perforated lamellar micro phases in a triblock copolymer. *European Polymer Journal*, 36:215–219, 2000.
- [83] G. Floudas, R. Ulrich, U. Wiesner, and B. Chu. Nucleation and growth in order-to-order transitions of a block copolymers. *Europhysics Letters*, 50:182–188, 2000.
- [84] M. W. Matsen. Cylinder to sphere epitaxial transitions in block copolymer melts. *Journal of Chemical Physics*, 114:8165–8173, 2001.
- [85] M. Imai, A. Saeki, T. Teramoto, A. Kawaguchi, K. Nakaya, T. Kato, and K. Ito. Kinetic pathway of lamellar to gyroid transition: Pretransition and transient states. *Journal of Chemical Physics*, 115:10525–10531, 2001.

- [86] J-H Ahn and W-C Zin. Mechanism of morphological transition from lamellar/perforated layer to gyroid phases. *Macromolecular Research*, 11:152–156, 2003.
- [87] K. Yamada, M. Nonomura, and T. Ohta. Kinetics of morphological transitions in microphase-separated diblock copolymers. *Macromolecules*, 37:5762–5777, 2004.
- [88] D. Q. Ly, T. Honda, T. Kawakatsu, and A. V. Zvelindovsky. Hexagonally perforated lamella-to-cylinder transition in a diblock copolymer thin film under an electric field. *Macromolecules*, 41:4501–4505, 2008.
- [89] R. K. W. Spencer and R.A. Wickham. Simulation of nucleation dynamics at the cylinder-to-lamellar transition in a diblock copolymer melt. *Soft Matter*, 9:3373–3382, 2013.
- [90] T. Q. Chastek and T. P. Lodge. Grain shapes and growth kinetics during self-assembly of block copolymers. *Journal of Polymer Science Part B: Polymer Physics*, 44:481–491, 2006.
- [91] Y.-L. Loo, R. A. Register, and A. J. Ryan. Polymer crystallization in 25-nm spheres. *Physical Review Letters*, 84:4120–4123, 2000.
- [92] D. Beysens, M. Gbadamassi, and L. Boyer. Light-scattering study of a critical mixture with shear flow. *Physical Review Letters*, 43:1253–1256, 1979.
- [93] E. K. Hobbie, D. W. Hair, A. I. Nakatani, and C. C. Han. Crossover to strong shear in a low-molecular-weight critical polymer blend. *Physical Review Letters*, 69:1951–1954, 1992.
- [94] P. K. Dixon, D. J. Pine, and X.-I. Wu. Mode selection in the dynamics of sheared polymer solutions. *Physical Review Letters*, 68:2239–2242, 1992.
- [95] S. Kitade, N. Ochiai, Y. Takahashi, I. Noda, Y. Matsushita, A. Karim, A. Nakatani, H. Kim, and C. Han. Lamellar orientation of diblock copolymer solutions under steady shear flow. *Macromolecules*, 31:8083–8090, 1998.

- [96] Y. Zhang, U. Wiesner, and H. W. Spiess. Frequency dependence of orientation in dynamically sheared diblock copolymers. *Macromolecules*, 28:778–781, 1995.
- [97] V. K. Gupta, R. Krishnamoorti, Z-R Chen, J. A. Kornfield, S. D. Smith, M. M. Satkowski, and J. T. Grothaus. Dynamics of shear alignment in a lamellar diblock copolymer: Interplay of frequency, strain amplitude, and temperature. *Macromolecules*, 29:875–884, 1996.
- [98] K. A. Koppi, M. Tirrell, F. S. Bates, K. Almdal, and R. H. Colby. Lamellae orientation in dynamically sheared diblock copolymer melts. *Journal de Physique II*, 2:1941–1959, 1992.
- [99] B. L. Peters, A. Ramirez-Hernandez, D. Q. Pike, and M. Muller. Nonequilibrium simulations of lamellae forming block copolymers under steady shear: A comparison of dissipative particle dynamics and brownian dynamics. *Macromolecules*, 45:8109–8116, 2012.
- [100] A. P. Marencic and R. A. Register. Controlling order in block copolymer thin films for nanopatterning applications. *The Annual Review of Chemical and Biomolecular Engineering*, 1:277–297, 2010.
- [101] S. Pujari, M. A. Keaton, P. M. Chaikin, and R. A. Register. Alignment of perpendicular lamellae in block copolymer thin films by shearing. *Soft Matter*, 8:5858–5863, 2012.
- [102] G. Singh, K. G. Yager, B. Berry, H-C Kim, and A. Karim. Dynamics thermal field-induced gradient soft-shear for highly oriented block copolymer thin films. *ACS Nano*, 6:10335–10342, 2012.
- [103] K. A. Koppi, M. Tirrell, and F. S. Bates. Shear-induced isotropic-to-lamellar transition. *Physical Review Letters*, 70:1449, 1993.
- [104] V. K. Gupta, R. Krishnamoorti, J. A. Kornfield, and S. D. Smith. Evolution of microstructure during shear alignment in a polystyrene-polyisoprene lamellar diblock copolymer. *Macromolecules*, 28:4464–4474, 1995.

- [105] L.Y. You, Y. D. HE, Y. Zhao, and Z. Y. Lu. The complex influence of the oscillatory shear on the melt of linear diblock copolymers. *Journal of Chemical Physics*, 129:204901, 2008.
- [106] P. G. de Gennes, F. Brochard-Wyart, and D. Quéré. *Capillarity and Wetting Phenomena: Drops, Bubbles, Pearls, Waves*. Springer-Verlag, New York, USA, 2004.
- [107] Y. Amarouchene, D. Bonn, J. Meunier, and H. Kellay. Inhibition of the finite-time singularity during droplet fission of a polymeric fluid. *Physical Review Letters*, 86:3558–3561, 2001.
- [108] J. W. Strutt and Rayleigh. On the instability of jets. *Proceedings of the London mathematical society*, 10:4–13, 1878.
- [109] L. E. Johns and R. Narayanan. *Interfacial Instability*. Springer, New York, 2002.
- [110] G. H. McKinley and A. Tripathi. How to extract the newtonian viscosity from capillary breakup measurements in a filament rheometer. *Journal of Rheology*, 44:653–670, 2000.
- [111] S. L. Anna and G. H. McKinley. Elasto-capillary thinning and breakup of model elastic liquids. *Journal of Rheology*, 45:115–138, 2001.
- [112] D. T. Papageorgiou. On the breakup of viscous liquid threads. *Physics of Fluids*, 7:1529–1544, 1995.
- [113] J. D. McGraw, T. Salez, O. Baumchen, E. Raphael, and K. Dalnoki-Veress. Capillary levelling of stepped films with inhomogeneous molecular mobility. *Soft Matter*, 9:8297–8305, 2013.
- [114] C. Clasen, J. Eggers, M. A. Fontelos, J. Li, and G. H. McKinley. The beads-on-string structure of viscoelastic threads. *Journal of Fluid Mechanics*, 556:283–308, 2006.

- [115] R. Sattler, C. Wagner, and J. Eggers. Blistering pattern and formation of nanofibers in capillary thinning of polymer solutions. *Physical Review Letters*, 100:164502, 2008.
- [116] P. P. Bhat, S. Appathurai, Harris. M. T., M. Pasquali, G. H. McKinley, and O. A. Basaran. Formation of beads-on-a-string structures during break-up of viscoelastic filaments. *Nature Physics*, 6:625–631, 2010.
- [117] R. Sattler, S. Gier, J. Eggers, and C. Wagner. The final stages of capillary break-up of polymer solutions. *Physics of Fluids*, 24:023101, 2012.
- [118] A. V. Bazilevskii. Dynamics of horizontal viscoelastic fluid filaments. *Fluid Dynamics*, 48:97–108, 2013.
- [119] C. Clasen, J. Bico, V. Entov, and G. H. McKinley. 'gobbling drops': The jetting-dripping transition in flows of polymer solutions. *Journal of Fluid Mechanics*, 636:5–40, 2009.
- [120] J. Eggers. Instability of a polymeric thread. *Physics of Fluids*, 26:033106, 2014.
- [121] A. Bach, K. Almdal, H. K. Rasmussen, and O. Hassager. Elongational viscosity of narrow molar mass distribution polystyrene. *Macromolecules*, 36:5174–5179, 2003.
- [122] M. H. Wagner, S. Kheirandish, and O. Hassager. Quantitative prediction of transient and steady-state elongational viscosity of nearly monodisperse polystyrene melts. *Journal of Rheology*, 49:1317–1327, 2005.
- [123] Y. Wang, P. Boukany, S-Q Wang, and X. Wang. Elastic breakup in uniaxial extension of entangled polymer melts. *Physical Review Letters*, 99:237801, 2007.
- [124] H. K. Rasmussen and K. Yu. Spontaneous breakup of extended monodisperse polymer melts. *Physical Review Letters*, 107:126001, 2011.
- [125] M. H. Wagner and V. H. Rolon-Garrido. Constant force elongational flow of polymer melts: Experiment and modelling. *Journal of Rheology*, 56:1279–1297, 2012.

-
- [126] T. P. Russell, R. P. Hjelm, and P. A. Seeger. Temperature dependence of the interaction parameter of polystyrene and poly(methyl methacrylate). *Macromolecules*, 23:890–893, 1990.
- [127] F.S. Bates. Polymer-polymer phase behavior. *Science*, 251:898–905, 1991.
- [128] Y. Takahashi, N. Ochiai, Y. Matsushita, and I. Noda. Viscoelastic properties of poly(2-vinylpyridine) in bulk and solution. *Polymer Journal*, 28:1065–1070, 1996.
- [129] A. B. Croll, M. W. Matsen, A-C Shi, and K. Dalnoki-Veress. Kinetics of layer hopping in a diblock copolymer lamellar phase. *European Physical Journal E*, 27:407–411, 2008.
- [130] R. M. A. Assam and N. M. Bashara. *Ellipsometry and Polarized Light*. North Holland Publishing, New York, 1977.
- [131] T. Vu, N. Mahadevapuram, G. M. Perera, and G. E. Stein. Controlling domain orientation in thin films of ab and aba block copolymers. *Macromolecules*, 44:6121–6127, 2011.